Utah State University

DigitalCommons@USU

All Graduate Theses and Dissertations | Graduate Studies

5-2015

Molecular Sensing and Imaging of Human Disease Cells and Their Responses to Biochemical Stimuli

Lifu Xiao
Utah State University

Follow this and additional works at: https://digitalcommons.usu.edu/etd

 Part of the Biological Engineering Commons

Recommended Citation

Xiao, Lifu, "Molecular Sensing and Imaging of Human Disease Cells and Their Responses to Biochemical Stimuli" (2015). *All Graduate Theses and Dissertations*. 4278.
https://digitalcommons.usu.edu/etd/4278

This Dissertation is brought to you for free and open access by the Graduate Studies at DigitalCommons@USU. It has been accepted for inclusion in All Graduate Theses and Dissertations by an authorized administrator of DigitalCommons@USU. For more information, please contact digitalcommons@usu.edu.



MOLECULAR SENSING AND IMAGING OF HUMAN DISEASE CELLS AND THEIR RESPONSES TO BIOCHEMICAL STIMULI

by

Lifu Xiao

A dissertation submitted in partial fulfillment
of the requirements for the degree

of

DOCTOR OF PHILOSOPHY

in

Biological Engineering

Approved:

Anhong Zhou, Ph.D. Major Professor	Timothy A. Gilbertson, Ph.D. Committee Member
Ronald C. Sims, Ph.D. Committee Member	Roger A. Coulombe, Jr., Ph.D. Committee Member
Bryan Howard, Ph.D. Committee Member	Mark R. McLellan, Ph.D. Vice President for Research and Dean of the School of Graduate Studies

UTAH STATE UNIVERSITY
Logan, Utah

2015

Copyright © Lifu Xiao 2015

All Rights Reserved

ABSTRACT

Molecular Sensing and Imaging of Human Disease Cells and Their Responses to Biochemical Stimuli

by

Lifu Xiao, Doctor of Philosophy

Utah State University, 2015

Major Professor: Dr. Anhong Zhou
Department: Biological Engineering

The overall goal of this dissertation is to develop noninvasive imaging techniques that allow us not only to detect diseased cells but also to study the molecular mechanisms underlying these diseases.

Atomic force microscopy and Raman spectroscopy are applied to measure cellular mechanical properties (e.g. Young's Modulus, adhesion force) and biochemical composition of living cancerous vs. healthy (A549 vs. SAEC) human lung epithelial cells. These biomechanical and biochemical properties can be utilized to differentiate between cancerous A549 and healthy SAEC human lung epithelial cells. Furthermore, different cellular responses to anticancer drug doxorubicin (DOX) treatment are also observed. Using AFM and Raman spectroscopy, we can quantitatively measure biophysical properties of different cells, as complementary parameters to other properties (e.g. gene and protein expression), helping identify the states of diseased cells.

Another major task of this dissertation is to develop noninvasive imaging techniques to detect cancer biomarker epidermal growth factor receptor (EGFR) at single

cell level using advanced instrumentation. We first synthesized a gold nanorod (AuNR)-based nanoprobe for single-cell imaging of EGFR using surface-enhance Raman spectroscopy (SERS). SERS is able to quantitatively measure the EGFR expression level in different breast cancer cell lines and map the cellular distribution of EGFR in single cells. Moreover, SERS, as a noninvasive imaging technique, is able to monitor the process of nanoparticle uptake by single cell. Due to the diffraction limit of optical microscopy, SERS is unable to provide nanoscale imaging resolution. We then applied an AFM-based simultaneous Topography and RECognition (TREC) imaging technique to image EGFR with nanoscale resolution. TREC is first validated on mica surface and then successfully utilized to map the EGFR distribution in fixed and living breast cancer cells at single molecule level. In addition, we have explored the potential of a gadolinium-gold (Gd-Au) composite nanomaterial as a dual functional (MRI-SERS) imaging probe. Using this previous reported MRI contrast agent, we successfully apply SERS function in the detection of EGFR in three cancer cell lines.

The last part of the dissertation is to study fat-responsive G protein-coupled receptor 120 (GPR120), and its interaction with linoleic acid (LA). We have synthesized a dual functional composite nanoparticle for SERS-fluorescence bimodal imaging of GRP120 in living HEK293 cells. By SERS-fluorescence imaging, we are able to locate GPR120 distribution in single cells. Moreover, we have observed a dose-dependent GPR120 response to LA treatments using SERS. This work demonstrates the potential to use SERS-fluorescence bimodal imaging technique for real-time detection of the interaction between fatty acids and their receptors (e.g. GPR120, CD36).

(201 pages)

PUBLIC ABSTRACT

Molecular Sensing and Imaging of Human Disease Cells and Their Responses to Biochemical Stimuli

Lifu Xiao

Advancement in microscopic and spectroscopic techniques could significantly improve our ability in the study and diagnosis of diseases. Especially, being able to image and detect human diseases at the cellular and molecular level allows people to diagnose diseases at early stages and to study the molecular mechanisms behind various diseases. Currently, histopathological techniques are most widely used for prognosis and diagnosis of human diseases. However, conventional histopathology requires a complex process of sample preparation, which limits the diagnostic efficiency of this technique. More importantly, it requires fixation of tissue or cell sample, making it unsuitable for the study of dynamic cellular activities in the progress of diseases. This dissertation mainly discusses the progress in development of noninvasive imaging techniques that can be applied to study human diseases at the cellular level.

One approach is to use atomic force microscopy (AFM) and Raman spectroscopy to quantitatively measure the biomechanical and biochemical properties of cells, and then use these properties to differentiate between different cell types, or cells at different states. Here we have utilized our tandem AFM-Raman spectroscopy system to differentiate between cancerous and healthy human lung epithelial cells, and monitor their different responses to anticancer drug treatments. Generally, this technique (AFM-Raman) can serve as a complementary approach to study various diseased cells, providing additional

information to help doctors identify diseases at an early stage and investigate the progress of diseases.

Another approach is specifically target and image disease marker molecules using advanced microscopic and spectroscopic techniques. Epidermal growth factor receptor (EGFR), as a cancer marker molecule, has been used as a model to develop noninvasive imaging methods. A nanoparticle-based imagine probe has been synthesized for specific imaging of EGFR at a single cell surface using surface-enhance Raman spectroscopy (SERS). Due to the noninvasive feature of SERS, it can monitor the receptor-mediated endocytosis of a nanoparticle in real time. Furthermore, an AFM-based simultaneous Topography and RECognition (TREC) imaging technique has been developed to localize EGFR subcellular distribution with nanoscale resolution. This TREC technique exhibits potential to monitor the binding between EGFR and its ligands at single molecule level.

A multimodal imaging nanoprobe, which integrates different imaging modalities into one single nanoparticle, can incorporate advantages and compensate for weaknesses of respective imaging techniques. In this dissertation, we have functionalized a previously reported nanoprobe for magnetic resonance imaging (MRI), trying to incorporate SERS function into this probe to realize MRI-SERS bimodal imaging. We have tested the SERS performance of the probe by using it to detect EGFR in three human cancer cell lines. This nanoprobe demonstrates the potential for *in vivo* MRI-SERS bimodal imaging with improved sensitivity from SERS. In addition, we have synthesized another composite nanoprobe for SERS-fluorescence bimodal imaging of a fat-responsive G protein-coupled receptor 120 (GPR120). Fluorescence is used as a fast indicator while SERS is for accurate localization of GPR120. Using this probe, we can also quantitatively measure the changes

of GPR120 activities in response to fatty acid binding, showing the potential to study the molecular mechanism of fatty acid chemoreception.

To my grandparents Chenggui Huang and Chengcai Xie I dedicate this dissertation.

ACKNOWLEDGMENTS

I would like to thank all those people who have provided valuable assistance and guidance that make me walk through all the difficulties and reach the completion of this doctoral program. First of all, I would like to thank my major advisor, Dr. Anhong Zhou, who has been a patient mentor not only teaching me to pursue academic success, but also giving me meticulous care since I came to the United States as a foreign student for the first time. Also, I would like to thank my committee members, Dr. Ronald Sims, Dr. Roger Coulomb, Dr. Tim Gilbertson, and Dr. Bryan Howard, for their advice and support during the entire process.

My sincere acknowledgment goes to the people I have worked with. Without their help, I could not have achieved any success in my graduate career. I would like to thank Dr. Yangzhe Wu, Qian Chen, and Mingjie Tang, who taught me every detail about the lab and helped me adapt to a new environment when I first came to USU. I also would like to thank the excellent researchers from Dr. Gilbertson's lab, Dr. Han Xu and Dr. Dane Hansen, for their support in the GPR120 project (chapter 6). Thanks to Dr. Xiaojun Qi for her help with complicated data analysis. Also special thanks to Dr. Sitaram Harihar and Dr. Danny Welch from the University of Kansas Medical Center for their collaboration in this dissertation. I am very grateful to have spent wonderful time with my labmates, Qifei Li, Han Zhang, Spencer Williams, Neil Draper, Dr. Ruizhen Li, Dr. Wen Zhang, and Dr. A. K. Parchur.

Most importantly, I want to thank my parents and my fiancée, Xiaojie Yang. Your strong support help me walk through this challenging and rewarding journey.

Lifu Xiao

This work was supported by Department of Defense CDMRP grant W81XWH-10-1-0668, National Science Foundation grant 1264498.

CONTENTS

Page

ABSTRACT III

PUBLIC ABSTRACT V

ACKNOWLEDGMENTS VIII

LIST OF TABLES XIII

LIST OF FIGURES XIV

CHAPTER

1. INTRODUCTION 1
2. NONINVASIVE DETECTION OF BIOMECHANICAL AND BIOCHEMICAL RESPONSES OF HUMAN LUNG CELLS TO SHORT TIME CHEMOTHERAPY EXPOSURE USING AFM AND CONFOCAL RAMAN SPECTROSCOPY 26
3. IMAGING OF EPIDERMAL GROWTH FACTOR RECEPTOR ON SINGLE BREAST CANCER CELLS USING SURFACE-ENHANCED RAMAN SPECTROSCOPY 57
4. SIMULTANEOUS TOPOGRAPHIC AND SINGLE MOLECULE RECOGNITION IMAGING OF EPIDERMAL GROWTH FACTOR RECEPTOR (EGFR) ON SINGLE HUMAN BREAST CANCER CELLS 85
5. GD_2O_3-DOPED SILICA @ GOLD NANOPARTICLES AS PROBES FOR IN VITRO CANCER BIOMARKER IMAGING USING SURFACE-ENHANCED RAMAN SPECTROSCOPY 112

6. SERS-FLUORESCENCE BIMODAL IMAGING OF FATTY ACID RESPONSIVE RECEPTOR GPR120 138

7. SUMMARY AND FUTURE DIRECTION 166

APPENDIX 172

CURRICULUM VITAE 179

LIST OF TABLES

Table Page

1.1. Raman spectroscopy in cellular investigation 22

2.1. Tentative Raman band assignments of Small Airway Epithelial Cells (SAEC) and human lung adenocarcinoma epithelial cell (A549). 47

LIST OF FIGURES

Figure Page

1.1. Schematic of chemobiomechanical pathways influencing connections among subcellular structure, cell biomechanics, motility and disease state (image adapted from ref [2]). 23

1.2. Biophysical and biochemical responses of human lung epithelial cells to doxorubicin anti-cancer drugs measured by AFM and Raman spectroscopy.....23

1.3. Schematic illustration of EGFR detection on single human cancer cells by SERS. 24

1.4. Schematic of interaction between EGFR and anti-EGFR measured by TREC imaging. 24

1.5. (a) STEM image of the Gd-Au nanoprobe. (b) Schematic of the SERS detection of EGFR using Gd-Au nanoprobes. 25

1.6. Schematic illustration of SERS-fluorescence bimodal nanoprobes for GPR120 detection. 25

2.1. AFM images of living (a) A549 and (b) SAEC cells. Cells are imaged in culture media under physiological condition. Scale bar: 10 μm. Histograms of (c) Young's modulus and (d) adhesion force distributions of A549 cells and SAECs.Data are expressed as mean±SD. 50

2.2. Comparison of (a) Young's modulus and (b) adhesion force of A549 cells and SAECs control groups and DOX (70nM, 4hr) treated groups.Values represent mean ± SD (bar) of multiple cells. *$p<0.05$, **$p<0.01$. 51

2.3. AFM deflection (row 1), phase contrast (row 2) and fluorescence (row 3) corresponding images of SAEC and A549 control and DOX treatment (70nM, 4hr), obtained simultaneously using coupled AFM/FL microscope.Cells were fixed with 4% paraformaldehyde. In fluorescence images, F-actin was stained with phalloidin and nucleus was stained with DAPI. Scale bar: 10 μm, column 1 and column 2; 16 μm, column 3 and column 4. 52

2.4. Average Raman spectra and PCA analysis of A549 cells and SAECs for cytoplasm (a, b) and membrane (c, d) areas of control and DOX treatment (70nM, 4hr) experiment.....53

2.5. (a) Average Raman spectra and (b) PCA analysis of A549 cells and SAECs for nucleus area of control and DOX treatment (70nM, 4hr) groups (n=32). 54

2.6. Raman intensity of the 720 cm^{-1}, 1006 cm^{-1} and 1450cm^{-1} bands of A549 cells and SAECs under control and DOX treatment condition. 720 cm^{-1}: DNA. 1006 cm^{-1}: Phenylalanine (protein), 1450 cm^{-1}: CH2 deformation of lipids. Scale bar represents standard deviation. Percentage numbers on column show the changes of peak intensity after DOX exposure. *p<0.05, **p<0.01. 55

2.7. Representative fluorescence images of cell viability test. Images of A549 cells and SAEC control (column 1, 2) and with DOX treatment (column 3, 4) were exhibited. Cells were stained with Invitrogen LIVE/DEAD Viability/ Cytotoxicity Assay Kit. Green fluorescence presented live cells, whereas red fluorescence showed dead or membrane-damaged cells. All images were obtained with 10× lens. These fluorescence images together revealed that A549 cells and SAECs which were used for AFM (row 1, 2) and Raman (row 3, 4) experiments were mostly alive. 56

3.1. (a) Schematic illustration of the fabrication of the gold nanorods-based, antibody-functionalized SERS probe. (b-d) Characterizations of the SERS probe. (b) TEM image of the bare gold nanorods, scale bar is 50 nm. (c) Extinction spectra of the AuNRs at each step of the coating process. (d) SERS spectrum of the antibody-functionalized gold nanorods with 4-MBA as the reporter molecules. AuNR: gold nanorod; 4-MBA: 4-mercaptobenzoic acid. 77

3.2. Fluorescence cell viability test. Cells were stained with Invitrogen LIVE/DEAD Viability/Cytotoxicity Assay Kit. Green fluorescence presented live cells, whereas red fluorescence showed dead or membrane-damaged cells. All images were obtained with 10× lens. The viability test shows that over 95% of A431 cells are alive after incubation with SERS probes for 1.5, 3, 4.5 and 6 hr. Over 500 cells were counted for each of the incubation times. 78

3.3. Performance assessment of constructed SERS probe. (a) Typical SERS spectra, (b) normalized average Raman intensities at 1077 cm^{-1} (curve numbers, n=60), and (c) typical single-cell bright-field and corresponding SERS mapping images of A431 cells incubated with (1) SERS probes without anti-EGFR antibody conjugation (No Antibody); (2) anti-EGFR antibody-conjugated SERS probes (Antibody); (3) free anti-EGFR antibody molecules prior to the incubation with antibody-conjugated SERS probes (Antibody_Block). Raman spectral images were created by the selection of peak 1077 cm^{-1}. The intensities were normalized between the lowest (0) and highest (1) color values. Image size: 30 × 30 μm^2. * P<0.001. 79

3.4. Raman line profiling of SERS probes bind to single A431 cell surface. (a) Image of an A431 cell showing 11 different locations with Raman measurements. (b) Raman profiles of the 11 points shown in (a). (c) Normalized Raman intensities at 1077 cm^{-1} at those eleven different locations. 80

3.5. Raman depth profiling of SERS probes bound to single A431 cell surface. (a) Raman streamline mapping (at 1077 cm^{-1}) of a living A431 cell. Three images (top, middle, and bottom) were respectively obtained at three different depths (0, 3 and 6 μm), when the cells were incubated with the SERS probes for 3 hr. (b) The typical

SERS spectra measured on the single cell shown in (a) at locations 1-3 with different depths. (c) Raman intensities (1077 cm^{-1}) at different depths with 1.5, 3, 4.5 and 6 hr incubation times, n=90, Error bar: SE of mean. Image size: 52 × 39 μm^2. 81

3.6. Comparison of EGFR detection by (a) immunoblotting and (b) SERS probes on MDA-MB-435 and MDA-MB-231 breast cancer cells, and their BRMS1 expressing cell lines MDA-MB-435^{BRMS1} and MDA-MB-231^{BRMS1}. (c-f) Dark field images of the SERS probes on MDA-MB-435 and MDA-MB-231 cells with (c, e) and without (d, f) BRMS1 expression. * P<0.001. n = 60, number of spectra collected. 82

3.7. Bright field and SERS mapping (1077 cm^{-1}) images of four breast cancer cell lines: 435, 435^{BRMS1}, 231 and 231^{BRMS1}. The intensities were normalized between the lowest (0) and the highest (1) color values for each pair of 435 vs. 435^{BRMS1}, and 231 vs. 231^{BRMS1}. Mapping size for all images is 30 × 30 μm^2.....83

3.8. Immune-fluorescence images for showing the expression of EGFR in MDA-MB-435, MDA-MB-435^{BRMS1}, MDA-MB-231 and MDA-MB-231^{BRMS1} cells. First column: EGFP; second column: EGFR; third column: nucleus; fourth column: merge of first three columns. 84

4.1. (a) Fabrication AFM MAC lever: (1) MAC lever amination; (2) link MAC lever with PEG linker; (3) antibody activation by SATP; (4) SATP-antibody conjugate to AFM tip. (b) SEM image for bare tip. (c) SEM image for anti-EGFR functionalized tip. 104

4.2. Specificity of recognition. (a) Topographic image and (b) corresponding recognition image of EGFR on mica. (c) Recognition image of EGFR after blocking by free anti-EGFR. (d, e, f) Cross section analysis along the green line in (a, b, c). Scan area: 500nm*500nm. 105

4.3. Topographic image, corresponding recognition and cross section profile of EGFR on mica under two conditions: (a) bare tip scans on EGFR only; (b) anti-EGFR antibody-tethered tip scans on EGFR with BSA presence. Scan area: 500nm*500nm. 106

4.4. Demonstration of recognition events. A pair of green dots in topography (a) and corresponding recognition (b) images represents a recognition event. After rescanning at the same location, changes in recognition events are labeled in the same recognition image (b). Green dot surrounded by a blue circle means a recognition event appear in the first scan but not in the second scan; blue dots represent recognition events appeared in the second scan but not in the first scan. Scan area: 2000nm*2000nm. 107

4.5. EGF influence on the recognition of EGFR on mica. Recognition events of EGFRs (green) superimposed on corresponding topography images before (a) and 10 min

after (b) the introduction of EGF solution (20 μg/mL). (c) EGF effect on recognition percentage. 108

4.6. Single 435 and 435^{BRMS1} cells' morphologies and their EGFR expression measured by TREC. (a-d) are the topography images (a, b) and corresponding deflection images (c, d) of Single 435 (a, c) and 435^{BRMS1} (b, d) cells. (e, f) are recognition events of EGFRs (green) superimposed onto corresponding topography images of 435 (e) and 435^{BRMS1} cells (f). 109

4.7. (a) Recognition image of EGFRs (green) superimposed on corresponding topography images of 435 cell. (b) Cross section profile along the red line in (a). Corresponding peaks were occurred at the positions of recognition sites, indicating the recognition events. 110

4.8. Schematic illustration of the TREC imaging method. 111

5.1. (a) Schematic illustration of the Gd-Au nanocomposite. (b) HAADF-STEM image of the Gd-Au nanocomposite. (c) EDX elemental mapping of oxygen (O), silicon (Si), gadolinium (Gd) and gold (Au) within the area labeled with an orange square in (b). (d) Hydraulic diameter of the nanocomposite determined by DLS. 129

5.2. (a) Parallel beam EDX spectrum of Gd-Au nanocomposite. (b) STEM image and corresponding elemental line profile of the Gd-Au nanocomposite. 130

5.3. (a) Schematic of the functionalization of Gd-Au nanocomposite. (b) Typical Raman spectra (600~1800 cm^{-1}) and (c) average Raman intensity at 1075 cm^{-1} of S18 cells under the treatments of PEG-NP, mAb-NP, and first free anti-EGFR molecules then mAb-NP. Error bar represents standard error of mean (SEM). (d) Dark field images of S18 cells alone (CTRL), cells incubated with PEG-NP, and cells incubated with mAb-NP. 131

5.4. Live/dead fluorescent images of S18 cells with mAb-NP incubation at concentrations of 8, 20, 28, 40 and 48 μg/ml. Cell viability is analyzed in the column graph. 132

5.5. (a) Bright field image of a single S18 cell with 1-h incubation with mAb-NP and the selected area for Raman mapping. Scale bar: 10 μm. (b-d) Raman images of the selected area after 60, 90 and 120 min incubation, respectively. The color scale is generated using peak intensity at 1075 cm^{-1}. (e-g) Extracted Raman spectra at the same position (green crosses) in (b-d). 133

5.6. Single cell Raman mapping of S18 cells after 120, 135, 150, 165, 180 and 195 min incubation of Gd-Au nanoprobes. The color scale is generated with peak intensity at 1075 cm^{-1} and is kept constant with Figure 5.5. 134

5.7. Representative Raman images of single S18, A431 and A549 cells incubated with Gd-Au nanoprobes (mAb-NPs). The first row shows bright field image and the selected area, and second row shows the corresponding Raman images. The color

scale is generated with peak intensity at 1075 cm^{-1} and is kept constant with Figure 5.5.....135

5.8. (a) Average peak intensity at 1075 cm^{-1} for S18, A431 and A549 cells with Gd-Au nanoprobes incubation. Data are collected from 50 spectra for each sample. **P<0.01. (b) Western blot result showing EGFR expression levels in S18, A431 and A549 cells.....136

5.9. Immunofluorescence images showing the EGFR expression in S18, A431 and A549 cells. 137

6.1. Characterization of the nanoprobe. (a) TEM image of $CaMoO_4:Eu^{3+}$@AuNR nanoparticle. Inset: EDX spectrum of the particle. (b) UV-Vis absorption spectra of AuNR and $CaMoO_4:Eu^{3+}$@AuNR. (c) FT-IR spectra of bare $CaMoO_4:Eu^{3+}$, $CaMoO_4:Eu^{3+}$@AuNR, and antibody-conjugated $CaMoO_4:Eu^{3+}$@AuNR. (d) Luminescent properties (excitation/emission) of the $CaMoO_4:Eu^{3+}$@AuNR nanoparticle.....157

6.2. FT-IR spectra of (a) HS–PEG–COOH, mPEG-HS and (b) GPR120 antibody. ..158

6.3. (a) Schematic for functionalization process of $CaMoO_4:Eu^{3+}$@AuNR nanocomposite. (b) Representative SERS spectra and (c) average SERS intensities at 1078 cm^{-1} (N=25) of $CaMoO_4:Eu^{3+}$@AuNR-MBA-Ab nanoprobe-incubated cell samples: (1) HEK293-GPR120 cells induced with DOX (GPR120 (+)); (2) HEK293-GPR120 cells without DOX inducing (GPR120 (-)); (3) constitutive HEK293-CD36 (CD36) cells. **P<0.001. 159

6.4. Immunofluorescence imaging to test the specificity of GPR120 antibody. Antibody ratio: 1^{st} 1:250, 2^{nd} 1:500. Color: red—GPR120, blue—DAPI. 160

6.5. Fluorescence imaging of GPR120 (+) and GPR120 (-) cells incubated with $CaMoO_4:Eu^{3+}$@AuNR-MBA-Ab nanoprobe for 24 hr. 161

6.6. Viability of GPR120 (+) cells with 24-hr incubation of $CaMoO_4:Eu^{3+}$@AuNR-MBA-Ab nanoprobe at concentrations of 20, 50, 80, 100, and 200 μg/mL. Green fluorescence presented live cells, whereas red fluorescence showed dead or membrane-damaged cells. Over 300 cells were counted for each treatment condition. Scale bar: 200 μm. **P<0.001.....162

6.7. Phase contrast (a, c) and Fluorescence (b, d) images of single CD36 (a, b) and GPR120 (+) (c, d) cells incubated with $CaMoO_4:Eu^{3+}$@AuNR-MBA-Ab nanoprobes for 24 hr. 163

6.8. Bright field images (a, c) and Raman mappings (b, d) of single CD36 (a, b) and GPR120 (+) (c, d) cells incubated with $CaMoO_4:Eu^{3+}$@AuNR-MBA-Ab nanoprobes for 24 hr. Raman mappings were generated by the selection of peak 1078 cm^{-1}. The intensities were normalized between the lowest (0) and highest (1) color values. Scale bar: 5 μm. 164

6.9. GPR120-LA dependence measured by SERS. (a) Average Raman spectra of $CaMoO_4:Eu^{3+}$@AuNR-MBA-Ab nanoprobe-incubated cells under 5 min LA treatment at concentrations 0, 5, 20, 30, and 60 μg/mL. (b) Linear relationship (R^2=0.93) between SERS intensity (1078 cm^{-1}) and LA concentration. Inset: expanded Raman spectra around 1078 cm^{-1}. 165

CHAPTER 1

INTRODUCTION

1.1 RATIONALE FOR PROPOSED RESEARCH

Health is one of the most important fields in human research. Every year, billions of US dollars are funded to support health-related studies, where thousands of researchers all over the world devote their lives, trying to fight human diseases and provide a better and healthier world. The comprehensive understanding of a disease and effective development of therapies requires an understanding of disease mechanisms at cellular and molecular levels. A typical example is the study of human tumors. Scientists have shown that the process of carcinogenesis proceeds through different stages such as initiation, promotion and progression. They found the occurrence of each stage is driven by different external or internal factors through different molecular mechanisms (reviewed in [1]). Thus, in order to monitor the cellular progress of cancer, or investigate the molecular mechanisms of other human diseases, there is always a need to develop new methods with improved accuracy and sensitivity, which can be applied in the detection and identification of single specific agents or multiple interactive factors that cause human diseases.

Currently, histopathology is most commonly used tool for study and diagnosis of a number of human diseases including most cancers [2]. Histopathology refers to the microscopic examination of tissues in order to study the manifestations of diseases. Conventional histopathology requires a complicated sample preparation process. For example, it requires (1) fixation of tissue to retain characteristic peculiarities of shape and structure; (2) sectioning to make micron-scale thin cuts for microscopic imaging; (3) histological staining to identify various components (e.g. disease markers) in cells and

tissues. Although the developments in digital pathology could substantially enhance the efficiency and accuracy of disease diagnosis by automated nuclei detection, segmentation, and classification [3], there still remains challenges in applying histopathology for disease studies. One major limitation is that histopathological imaging needs cells and tissues to be fixed ("killed"), which makes it incapable of monitoring dynamic changes of cells and tissues in the process of disease progress. Noninvasive imaging techniques need to be developed in order to study cellular mechanism of human diseases.

This dissertation communicates progress on the development of noninvasive imaging techniques to identify human diseased cells. Biomechanical and biochemical properties measured by atomic force microscopy (AFM) and Raman spectroscopy, respectively, are used to distinguish between different types of cells and different cellular responses to external stimuli. This combined AFM-Raman method is explored as a biophysical approach to increase the understanding of disease mechanisms. Another approach explored in this research is to build biocompatible imaging nanoprobes for detection and mapping of biomarker molecules in human cells using advanced microscopic and spectroscopic imaging techniques.

1.2 BACKGROUND

Since a more detailed background introduction is included in each technical chapter from chapter 2 to chapter 6, here only a brief background is presented to cover several important concepts in the dissertation.

1.2.1 Cellular biomechanics and biochemical compositions measured by AFM and Raman

In past decades, researchers have made considerable efforts to establish the links between measures of cellular biomechanics and human disease states. The relationships between cell structure, cell biomechanics and disease states can be summarized in a structure-property-function-disease paradigm [4] (Figure 1.1). This paradigm shows that changes in subcellular structures, especially in the cytoskeleton, will induce alterations in biomechanical properties, sequentially alter cell functions, and result in various disease states. It is reported that biomechanical properties can contribute to the regulation of tumor cell functions such as tumor progression, cell proliferation, motility, migration, invasion and metastasis [5, 6]. *In vitro* studies have shown that cellular biomechanics including cell stiffness and adhesion of cancer cells are often lower than that of their normal counterparts. This is thought to be mainly due to differently organized cytoskeletal structures [7]—this difference in mechanical properties also has been considered a "biomechanical marker" to early diagnosis of cancers [8, 9]. As a nondestructive nanoscale technique, AFM has been widely applied in the biomechanical studies for mammalian cells, especially for cancer cells [8-12].

Raman spectroscopy, based on the inelastic scattering of the incident laser on target molecules, is a molecular vibrational spectroscopic technique that can detect molecular structural information used to identify specific subcellular biochemical compositions in living cells [13]. Raman spectra provide highly specific and reproducible vibrational fingerprints of different cell types. In addition, this noninvasive technique can conduct rapid real-time cell detection under physiological growth environments. Previous Raman

studies have shown that cellular biochemical compositions and molecular structures (e.g. DNA/RNA, proteins and lipids) also exhibit differences in cells with different disease states [14-17]. Several studies applying Raman spectroscopy in cellular investigations have been summarized in Table 1.1. Since the differences of the Raman spectra are usually non-significant for different cell types, principal component analysis (PCA) is often applied on the spectra to classify them into different categories.

In past years, the Zhou lab from Utah State University has conducted a series of studies incorporating AFM and Raman analyses, together with other techniques, to investigate the biomechanics and biochemical changes of mammalian cells under various conditions. By using AFM and Raman spectroscopy, Wu *et al.* [18] observed alterations in cyto-architectures, mechanical properties, and biochemical components of human breast carcinoma cells (MDA-MB-435), when transfected with BReast cancer Metastasis Suppressor 1 (BRMS1) gene. This gene has been shown to induce many phenotypic alterations in MDA-MB-435 cells [19]. Tang *et al.* applied Raman spectroscopy, AFM, and multiplex ELISA to investigate the biophysical responses (including biomechanics and bio-spectroscopic responses) of human lung epithelial cells to short term exposure of diesel exhaust particles [20]. Li *et al.* used the biochemical and biophysical properties, measured by Raman and AFM, as an indicator to monitor serum-induced differentiation of trophoblast derived stem-like cells [21]. All these studies have demonstrated the potential of AFM and Raman as nondestructive methodologies to investigate human disease cells and their metabolism at subcellular level.

1.2.2 Epidermal growth factor receptor (EGFR)

Epidermal growth factor receptor (EGFR) is a member of the receptor tyrosine kinase (RTK) family of signaling proteins. It was the first mammalian signaling protein to be fully characterized [22]. The activation of EGFR is normally controlled by the interaction with their ligands such as EGF and TGF-α, providing cells with substantial differentiation and growth advantages [23]. However, it has been found that aberrant expression or activation of EGFR appears to be an important factor in both the initiation and the progression of human caner [24-26]. For example, in human breast carcinoma (EGFR positive), expression of EGFR was reported to support the existence of tumor cells with aggressive potentials [27]. The expression level of EGFR in metastatic breast tumors was often higher than primary tumors, indicating that EGFR was involved in the process of metastasis [19, 28]. Overexpression and abnormal function of EGFR and its ligands have been found in many different types of human cancers [26]; this makes it a great prognostic indicator for the development of malignancies. Furthermore, therapeutic strategies have been developed, using small biomolecules (e.g. monoclonal antibody, kinase inhibitors) to block the binding of EGFR and its ligands, consequently blocking receptor activation and transduction of post-receptor signals [29, 30].

1.2.3 Surface-enhanced Raman spectroscopy (SERS)

Surface-enhanced Raman spectroscopy (SERS) is a powerful analytical tool in biological applications which has attracted considerable attention recently. SERS offers extremely high enhancement and turns the weak inelastic scattering effect of photons into a structurally sensitive nanoscale probe [31]. As a result, one can realize ultrasensitive levels of detection and non-invasive tagging of specific bioanalytes in living cells and

animals [32]. A key component of the SERS technique is the SERS-active nanoprobe. It is usually composed of metal nanoparticle (NP, e.g. AuNP or AgNP) encoded with sensitive Raman reporter molecules followed by the coating of mono- or multi-layer protective polymers (e.g. silica, polyelectrolyte and PEG) which improve stability and biocompatibility [33-36]. Several studies have reported using SERS probes to target cancer cells in vitro or in vivo [33, 36-41], including measurement of EGFR [33, 37, 41]. However, very little SERS studies were focused on EGFR cellular distribution, EGFR-mediated bioprocess, and how EGFR is regulated by metastasis suppressors.

1.2.4 AFM and simultaneous Topography and RECognition (TREC) imaging

In past decades, AFM has become a powerful technique for analyzing the surface structures at nanometer scale and the forces acting on them with piconewton sensitivity [42, 43]. In terms of studying biological samples, AFM presents significant advantages over other microscopic methods since it allows single-molecule level studies of the structure and interaction of complicated biomolecules and cells with nanometer spatial resolution [44]. It also allows samples to be measured in liquid phase, enabling the study of dynamic interactions between biomolecules under physiological cell growth environments. Simultaneous Topography and RECognition (TREC) imaging, a new AFM technique based on the high-resolution topographic imaging and single-molecule force measurement [45, 46], has been developed for receptor imaging with high spatial and temporal resolution. This methodology provides information that is complementary to that obtained by fluorescence and electron microscopy [47]. For example, TREC imaging has been successfully used to visualize for the first time, the localization and distribution of Na^+-K^+ ATPases in the inner leaflet of cell membranes at the single-molecule level [48].

Also, by employing TREC, the local organization of Fcγ receptors on a single macrophage cell has been determined at single-molecule level [49]. In addition to cell receptor imaging, the TREC imaging technique has also been extensively used to monitor specific biomolecules while they are undergoing biological processes. Wang *et al.* [45, 50, 51] applied TREC to study the action of human Swi-Snf nucleosome remodeling complex and its interaction with mouse mammary tumor virus promoter during the process of nucleosome remodeling, describing the crucial role of ATP activation in the process. In addition, they were also able to recognize the glycosylation process of biomolecules by using TREC imaging, and distinguish normal and aberrant antibodies based on their glycosylation [52].

1.2.5 Multimodal cancer imaging

Noninvasive cancer imaging, used to describe tumor anatomical structure and to investigate tumor metabolism, plays an important role in early cancer detection and localization [53]. Currently, there are several imaging modalities widely applied in cancer research, such as magnetic resonance imaging (MRI) [54-57], photoacoustic (PA) imaging [58-60], surface-enhanced Raman scattering (SERS) [61-63] and optical fluorescent imaging [64-67]. Although each individual modality has specific advantages in cancer imaging, none are able to support comprehensive structural and functional studies of tumors independently. Thus, there has been an interest in developing multimodal approaches to combine the advantages of these individual imaging modalities and to compensate for their weaknesses. Recently, several composite nanoparticles have been successfully synthesized and used in multimodal imaging applications [68-73]. Theses composite nanoparticles are usually constructed by combining together different nano-

components, which are effective contrast agents for different imaging modalities. For example, Jin *et al.* [68] had synthesized an iron oxide and gold-coupled core-shell nanoparticle to integrate both MRI and PA imaging, which provides remarkable contrast enhancement in bioimaging. Despite the quickly growing interest in designing multifunctional imaging contrast agents, it remains challenging to combine multiple components to incorporate different imaging modalities while preserving particle size.

1.3 DISSERTATION OUTLINE

In chapter 2, I included a study that uses AFM and Raman to study human lung cancer cells in response to short time chemotherapy (Figure 1.2). Young's modulus and adhesion force of human lung adenocarcinoma epithelial cell line A549 and non-cancerous human primary small airway epithelial cells (SAECs) were measured by using AFM. It was found that normal SAECs are stiffer and more adhesive than cancerous A549 cells. Upon treatment with anti-cancer drug doxorubicin (DOX) for a short time (4 hr), both biomechanical properties of A549 cells were found to be increased while those of SAECs were decreased, implying that DOX induced response mechanisms are different between the two types of cells (cancerous vs. healthy cells). Using Raman spectroscopy, we measured the changes in subcellular biochemical compositions of both cell types before and after DOX exposure.

In chapter 3, I included a study that investigates expression, spatial distribution as well as the endocytosis of EGFR in single breast cancer cells using SERS (Figure 1.3). By incubating anti-EGFR antibody conjugated SERS nanoprobes with an EGFR-over-expressing cancer cell line, A431, EGFR localization was measured over time and found to be located primarily at the cell surface. To further validate the constructed SERS probes,

we applied this SERS probes to detect the EGFR expression on breast cancer cells (MDA-MB-435, MDA-MB-231) and their counterpart cell lines in which EGFR expression was down-regulated by breast cancer metastasis suppressor 1 (BRMS1). The results showed that SERS method not only confirms immunoblotting data measuring EGFR levels, but also adds new insights regarding EGFR localization and internalization in living cells which is impossible in immunoblotting method.

In chapter 4, I included a study that applies TREC imaging method to mapping the distribution of EGFR on single breast cancer cells at single-molecule level (Figure 1.4). Single molecule recognition using monoclonal antibody (anti-EGFR) tethered scanning tip was converted to high resolution Topography and Recognition images. The recognition efficiency was tested in a spatial-temporal manner by introducing EGF as a competing ligand, when conducting TREC imaging of EGFR using antibody-tethered AFM tips. We measured the density and distribution of EGFR on breast cancer cell lines—MDA-MB-435 and BRMS1-transfected 435 cells. We further discussed the advantages of TREC imaging over conventional detection methods such as western blot and immunofluorescence.

In chapter 5, I included a study that describes a novel hybrid Gd-Au nanocomposite (Gd_2O_3@MCM-41@Au), and its application on SERS detection of EGFR (Figure 1.5). We synthesized and characterized the Gd-Au nanocomposite, and further performed a series of functionalization processes to make it capable of SERS detection. We conjugated monoclonal antibody (mAb) to specifically target EGFR in three different human cancer cell lines: human nasopharyngeal carcinoma cell (S18), human epidermoid carcinoma cell (A431), and human lung adenocarcinoma cell (A549). These cell lines are measured by

SERS to express EGFR at different levels. In addition, we used SERS to mapping the cellular distribution of EGFR on single cancer cells as well as to monitor the metabolism of the antibody-targeted nanoparticles in real time. Combining our SERS study and the MRI study conducted by our collaborators in China [74], we demonstrate the potential of this Gd-Au nanocomposite as a multifunctional (MRI-SERS) nano-probe not only for the early detection and localization of cancer in vivo, but also for the investigation of cancer metabolism and biochemistry at single cell level.

In chapter 6, I included a study that describes a SERS-fluorescence dual functional nanocomposite ($CaMoO_4:Eu^{3+}$@AuNR), and its application on SERS-fluorescence bimodal imaging of GPR120 (Figure 1.6). The composite nanoprobe $CaMoO_4:Eu^{3+}$@AuNR was synthesized, characterized and functionalized for specific targeting of G-protein-coupled receptor 120 (GPR120). As a model to demonstrate the SERS-fluorescence bimodal imaging, we used a HEK293 cell line transfected with a cDNA sequence encoding a doxycycline (Dox)-inducible mature peptide of GPR120. Both SERS and fluorescence imaging showed elevated signals on GPR120 positive cells. In addition, the interaction between GPR120 and linoleic acid (LA) was also investigated by SERS.

In chapter 7, I gave a brief summary of this dissertation research and discussed directions for future research.

1.4 REFERENCES

[1] I.B. Weinstein, The origins of human cancer: molecular mechanisms of carcinogenesis and their implications for cancer prevention and treatment—27th Clowes, G.H.A. Memorial Award Lecture, Cancer Res. 48 (1988) 4135-4143.

[2] M.N. Gurcan, L.E. Boucheron, A. Can, A. Madabhushi, N.M. Rajpoot, B. Yener, Histopathological image analysis: a review, IEEE Rev. Biomed. Eng., 2 (2009) 147-171.

[3] H. Irshad, A. Veillard, L. Roux, D. Racoceanu, Methods for nuclei detection, segmentation, and classification in digital histopathology: a review-current status and future potential, IEEE Rev. Biomed. Eng., 7 (2014) 97-114.

[4] S. Suresh, Biomechanics and biophysics of cancer cells, Acta Mater. 55 (2007) 3989-4014.

[5] F. Michor, J. Liphardt, M. Ferrari, J. Widom, What does physics have to do with cancer?, Nat. Rev. Cancer 11 (2011) 657-670.

[6] H.M. Yu, J.K. Mouw, V.M. Weaver, Forcing form and function: biomechanical regulation of tumor evolution, Trends Cell Biol. 21 (2011) 47-56.

[7] Q.S. Li, G.Y.H. Lee, C.N. Ong, C.T. Lim, AFM indentation study of breast cancer cells, Biochem. Bioph. Res. Co. 374 (2008) 609-613.

[8] S. Suresh, Nanomedicine - elastic clues in cancer detection, Nat. Nanotechnol. 2 (2007) 748-749.

[9] S.E. Cross, Y.S. Jin, J. Rao, J.K. Gimzewski, Nanomechanical analysis of cells from cancer patients, Nat. Nanotechnol. 2 (2007) 780-783.

[10] S.E. Cross, Y.S. Jin, J. Tondre, R. Wong, J. Rao, J.K. Gimzewski, AFM-based analysis of human metastatic cancer cells, Nanotechnology 19 (2008) 384003.

[11] V. Palmieri, D. Lucchetti, A. Maiorana, M. Papi, G. Maulucci, G. Ciasca, M. Svelto, M. De Spirito, A. Sgambato, Biomechanical investigation of colorectal cancer cells, Appl. Phys. Lett. 105 (2014) 123701.

[12] S. Iyer, R.M. Gaikwad, V. Subba-Rao, C.D. Woodworth, I. Sokolov, Atomic force microscopy detects differences in the surface brush of normal and cancerous cells, Nat. Nanotechnol. 4 (2009) 389-393.

[13] C.A. Owen, I. Notingher, R. Hill, M. Stevens, L.L. Hench, Progress in Raman spectroscopy in the fields of tissue engineering, diagnostics and toxicological testing, J. Mater. Sci. - Mater. Med. 17 (2006) 1019-1023.

[14] J.W. Chan, D.S. Taylor, T. Zwerdling, S.M. Lane, K. Ihara, T. Huser, Micro-Raman spectroscopy detects individual neoplastic and normal hematopoietic cells, Biophys. J. 90 (2006) 648-656.

[15] J.W. Chan, D.S. Taylor, S.M. Lane, T. Zwerdling, J. Tuscano, T. Huser, Nondestructive identification of individual leukemia cells by laser trapping Raman spectroscopy, Anal. Chem. 80 (2008) 2180-2187.

[16] I. Notingher, Raman spectroscopy cell-based biosensors, Sensors-Basel 7 (2007) 1343-1358.

[17] F.M. Lyng, E.O. Faolain, J. Conroy, A.D. Meade, P. Knief, B. Duffy, M.B. Hunter, J.M. Byrne, P. Kelehan, H.J. Byrne, Vibrational spectroscopy for cervical cancer pathology, from biochemical analysis to diagnostic tool, Exp. Mol. Pathol. 82 (2007) 121-129.

[18] Y.Z. Wu, G.D. McEwen, S. Harihar, S.M. Baker, D.B. DeWald, A.H. Zhou, BRMS1 expression alters the ultrastructural, biomechanical and biochemical properties of MDA-MB-435 human breast carcinoma cells: an AFM and Raman microspectroscopy study, Cancer Lett. 293 (2010) 82-91.

[19] K.S. Vaidya, S. Harihar, P.A. Phadke, L.J. Stafford, D.R. Hurst, D.G. Hicks, G. Casey, D.B. DeWald, D.R. Welch, Breast cancer metastasis suppressor-1 differentially modulates growth factor signaling, J. Biol. Chem. 283 (2008) 28354-28360.

[20] M.J. Tang, Q.F. Li, L.F. Xiao, Y.P. Li, J.L. Jensen, T.G. Liou, A.H. Zhou, Toxicity effects of short term diesel exhaust particles exposure to human small airway epithelial cells (SAECs) and human lung carcinoma epithelial cells (A549), Toxicol. Lett. 215 (2012) 181-192.

[21] Q. Li, E. Suasnavas, L. Xiao, S. Heywood, X. Qi, A. Zhou, S.C. Isom, Label-free and non-invasive monitoring of porcine trophoblast derived cells: differentiation in serum and serum-free media, J. Biophotonics (2014) doi: 10.1002/jbio.201400062.

[22] A. Ullrich, L. Coussens, J.S. Hayflick, T.J. Dull, A. Gray, A.W. Tam, J. Lee, Y. Yarden, T.A. Libermann, J. Schlessinger, J. Downward, E.L.V. Mayes, N. Whittle, M.D. Waterfield, P.H. Seeburg, Human epidermal growth-factor receptor cDNA sequence and aberrant expression of the amplified gene in A431 epidermoid carcinoma cells, Nature 309 (1984) 418-425.

[23] D. Gospodarowicz, Epidermal and nerve growth-factors in mammalian development, Annu. Rev. Physiol. 43 (1981) 251-263.

[24] D.S. Salomon, R. Brandt, F. Ciardiello, N. Normanno, Epidermal growth factor-related peptides and their receptors in human malignancies, Crit. Rev. Oncol. Hemat. 19 (1995) 183-232.

[25] K. Khazaie, V. Schirrmacher, R.B. Lichtner, EGF receptor in neoplasia and metastasis, Cancer Metast. Rev. 12 (1993) 255-274.

[26] R.I. Nicholson, J.M.W. Gee, M.E. Harper, EGFR and cancer prognosis, Eur. J. Cancer 37 (2001) 9-15.

[27] M. Bilous, J. Milliken, J.M. Mathijs, Immunocytochemistry and in situ hybridization of epidermal growth factor receptor and relation to prognostic factors in breast cancer, Eur. J. Cancer 28 (1992) 1033-1037.

[28] M. Toi, A. Osaki, H. Yamada, T. Toge, Epidermal growth factor receptor expression as a prognostic indicator in breast cancer, Eur. J. Cancer. 27 (1991) 977-980.

[29] E.K. Rowinsky, The erbB family: targets for therapeutic development against cancer and therapeutic strategies using monoclonal antibodies and tyrosine kinase inhibitors, Annu. Rev. Med. 55 (2004) 433-457.

[30] N.E. Hynes, H.A. Lane, ERBB receptors and cancer: the complexity of targeted inhibitors, Nat. Rev. Cancer 5 (2005) 341-354.

[31] J. Kneipp, H. Kneipp, K. Kneipp, SERS—a single-molecule and nanoscale tool for bioanalytics, Chem. Soc. Rev. 37 (2008) 1052-1060.

[32] R.A. Alvarez-Puebla, L.M. Liz-Marzan, SERS-based diagnosis and biodetection, Small 6 (2010) 604-610.

[33] K.K. Maiti, U.S. Dinish, C.Y. Fu, J.J. Lee, K.S. Soh, S.W. Yun, R. Bhuvaneswari, M. Olivo, Y.T. Chang, Development of biocompatible SERS nanotag with increased stability by chemisorption of reporter molecule for in vivo cancer detection, Biosens. Bioelectron. 26 (2010) 398-403.

[34] G. von Maltzahn, A. Centrone, J.H. Park, R. Ramanathan, M.J. Sailor, T.A. Hatton, S.N. Bhatia, SERS-coded gold nanorods as a multifunctional platform for densely

multiplexed near-infrared imaging and photothermal heating, Adv. Mater. 21 (2009) 3175-3180.

[35] C.L. Zavaleta, B.R. Smith, I. Walton, W. Doering, G. Davis, B. Shojaei, M.J. Natan, S.S. Gambhir, Multiplexed imaging of surface enhanced Raman scattering nanotags in living mice using noninvasive Raman spectroscopy, Proc. Natl. Acad. Sci. USA 106 (2009) 13511-13516.

[36] L. Jiang, J. Qian, F.H. Cai, S.L. He, Raman reporter-coated gold nanorods and their applications in multimodal optical imaging of cancer cells, Anal. Bioanal. Chem. 400 (2011) 2793-2800.

[37] X.M. Qian, X.H. Peng, D.O. Ansari, Q. Yin-Goen, G.Z. Chen, D.M. Shin, L. Yang, A.N. Young, M.D. Wang, S.M. Nie, In vivo tumor targeting and spectroscopic detection with surface-enhanced Raman nanoparticle tags, Nat. Biotechnol. 26 (2008) 83-90.

[38] D.C. Kennedy, D.R. Duguay, L.L. Tay, D.S. Richeson, J.P. Pezacki, SERS detection and boron delivery to cancer cells using carborane labelled nanoparticles, Chem. Commun. (2009) 6750-6752.

[39] P. Wu, Y. Gao, H. Zhang, C.X. Cai, Aptamer-guided silver-gold bimetallic nanostructures with highly active surface-enhanced Raman scattering for specific detection and near-infrared photothermal therapy of human breast cancer cells, Anal. Chem. 84 (2012) 7692-7699.

[40] J. Yang, Z.Y. Wang, S.F. Zong, C.Y. Song, R.H. Zhang, Y.P. Cui, Distinguishing breast cancer cells using surface-enhanced Raman scattering, Anal. Bioanal. Chem. 402 (2012) 1093-1100.

[41] X. Wang, X.M. Qian, J.J. Beitler, Z.G. Chen, F.R. Khuri, M.M. Lewis, H.J.C. Shin, S.M. Nie, D.M. Shin, Detection of circulating tumor cells in human peripheral blood using surface-enhanced Raman scattering nanoparticles, Cancer Res. 71 (2011) 1526-1532.

[42] D.J. Muller, Y.F. Dufrene, Atomic force microscopy as a multifunctional molecular toolbox in nanobiotechnology, Nat. Nanotechnol. 3 (2008) 261-269.

[43] R.M.A. Sullan, A.B. Churnside, D.M. Nguyen, M.S. Bull, T.T. Perkins, Atomic force microscopy with sub-picoNewton force stability for biological applications, Methods 60 (2013) 131-141.

[44] J.K.H. Horber, M.J. Miles, Scanning probe evolution in biology, Science 302 (2003) 1002-1005.

[45] C. Stroh, H. Wang, R. Bash, B. Ashcroft, J. Nelson, H. Gruber, D. Lohr, S.M. Lindsay, P. Hinterdorfer, Single-molecule recognition imaging-microscopy, Proc. Natl. Acad. Sci. USA 101 (2004) 12503-12507.

[46] P. Hinterdorfer, Y.F. Dufrene, Detection and localization of single molecular recognition events using atomic force microscopy, Nat. Methods 3 (2006) 347-355.

[47] L.A. Chtcheglova, P. Hinterdorfer, Simultaneous topography and recognition imaging on endothelial cells, J. Mol. Recognit. 24 (2011) 788-794.

[48] J.G. Jiang, X. Hao, M.J. Cai, Y.P. Shan, X. Shang, Z.Y. Tang, H.D. Wang, Localization of Na^+-K^+ ATPases in quasi-native cell membranes, Nano Lett. 9 (2009) 4489-4493.

[49] S.F. Ahmad, L.A. Chtcheglova, B. Mayer, S.A. Kuznetsov, P. Hinterdorfer, Nanosensing of Fcγ receptors on macrophages, Anal. Bioanal. Chem. 399 (2011) 2359-2367.

[50] H. Wang, R. Bash, J.G. Yodh, G. Hager, S.M. Lindsay, D. Lohr, Using atomic force microscopy to study nucleosome remodeling on individual nucleosomal arrays in situ, Biophys. J. 87 (2004) 1964-1971.

[51] H. Wang, R. Bash, S.M. Lindsay, D. Lohr, Solution AFM studies of human Swi-Snf and its interactions with MMTV DNA and chromatin, Biophys. J. 89 (2005) 3386-3398.

[52] H.D. Wang, L. Obenauer-Kutner, M. Lin, Y.P. Huang, M.J. Grace, S.M. Lindsay, Imaging glycosylation, J. Am. Chem. Soc. 130 (2008) 8154-8155.

[53] J.S. Xu, J.W. Huang, R.G. Qin, G.H. Hinkle, S.P. Povoski, E.W. Martin, R.X. Xu, Synthesizing and binding dual-mode poly (lactic-co-glycolic acid) (PLGA) nanobubbles for cancer targeting and imaging, Biomaterials 31 (2010) 1716-1722.

[54] K. El-Boubbou, D.C. Zhu, C. Vasileiou, B. Borhan, D. Prosperi, W. Li, X.F. Huang, Magnetic glyco-nanoparticles: a tool to detect, differentiate, and unlock the glyco-codes of cancer via magnetic resonance imaging, J. Am. Chem. Soc. 132 (2010) 4490-4499.

[55] Y. Chen, H.R. Chen, D.P. Zeng, Y.B. Tian, F. Chen, J.W. Feng, J.L. Shi, Core/shell structured hollow mesoporous nanocapsules: a potential platform for simultaneous cell imaging and anticancer drug delivery, ACS Nano 4 (2010) 6001-6013.

[56] M.G. Harisinghani, J. Barentsz, P.F. Hahn, W.M. Deserno, S. Tabatabaei, C.H. van de Kaa, J. de la Rosette, R. Weissleder, Noninvasive detection of clinically occult lymph-node metastases in prostate cancer, New Engl. J. Med. 348 (2003) 2491-2499.

[57] J.H. Lee, Y.M. Huh, Y. Jun, J. Seo, J. Jang, H.T. Song, S. Kim, E.J. Cho, H.G. Yoon, J.S. Suh, J. Cheon, Artificially engineered magnetic nanoparticles for ultra-sensitive molecular imaging, Nat. Med. 13 (2007) 95-99.

[58] E.I. Galanzha, E.V. Shashkov, T. Kelly, J.W. Kim, L.L. Yang, V.P. Zharov, In vivo magnetic enrichment and multiplex photoacoustic detection of circulating tumour cells, Nat. Nanotechnol. 4 (2009) 855-860.

[59] S.A. Ermilov, T. Khamapirad, A. Conjusteau, M.H. Leonard, R. Lacewell, K. Mehta, T. Miller, A.A. Oraevsky, Laser optoacoustic imaging system for detection of breast cancer, J. Biomed. Opt. 14 (2009) 024007.

[60] S. Manohar, S.E. Vaartjes, J.C.G. van Hespen, J.M. Klaase, F.M. van den Engh, W. Steenbergen, T.G. van Leeuwen, Initial results of in vivo non-invasive cancer imaging in the human breast using near-infrared photoacoustics, Opt. Express 15 (2007) 12277-12285.

[61] S. Keren, C. Zavaleta, Z. Cheng, A. de la Zerda, O. Gheysens, S.S. Gambhir, Noninvasive molecular imaging of small living subjects using Raman spectroscopy, Proc. Natl. Acad. Sci. USA 105 (2008) 5844-5849.

[62] A. Samanta, K.K. Maiti, K.S. Soh, X. Liao, M. Vendrell, U.S. Dinish, S.W. Yun, R. Bhuvaneswari, H. Kim, S. Rautela, J. Chung, M. Olivo, Y.T. Chang, Ultrasensitive near-infrared Raman reporters for SERS-based in vivo cancer detection, Angew Chem. Int. Ed. Engl. 50 (2011) 6089-6092.

[63] L. Xiao, S. Harihar, D.R. Welch, A. Zhou, Imaging of epidermal growth factor receptor on single breast cancer cells using surface-enhanced Raman spectroscopy, Anal. Chim. Acta 843 (2014) 73-82.

[64] A. Becker, C. Hessenius, K. Licha, B. Ebert, U. Sukowski, W. Semmler, B. Wiedenmann, C. Grotzinger, Receptor-targeted optical imaging of tumors with near-infrared fluorescent ligands, Nat. Biotechnol. 19 (2001) 327-331.

[65] M. Wang, C.C. Mi, W.X. Wang, C.H. Liu, Y.F. Wu, Z.R. Xu, C.B. Mao, S.K. Xu, Immunolabeling and NIR-excited fluorescent imaging of HeLa cells by using $NaYF_4$:Yb,Er upconversion nanoparticles, ACS Nano 3 (2009) 1580-1586.

[66] Y. Urano, D. Asanuma, Y. Hama, Y. Koyama, T. Barrett, M. Kamiya, T. Nagano, T. Watanabe, A. Hasegawa, P.L. Choyke, H. Kobayashi, Selective molecular imaging of viable cancer cells with pH-activatable fluorescence probes, Nat. Med. 15 (2009) 104-109.

[67] M. Yang, E. Baranov, P. Jiang, F.X. Sun, X.M. Li, L.N. Li, S. Hasegawa, M. Bouvet, M. Al-Tuwaijri, T. Chishima, H. Shimada, A.R. Moossa, S. Penman, R.M. Hoffman, Whole-body optical imaging of green fluorescent protein-expressing tumors and metastases, Proc. Natl. Acad. Sci. USA 97 (2000) 1206-1211.

[68] Y.D. Jin, C.X. Jia, S.W. Huang, M. O'Donnell, X.H. Gao, Multifunctional nanoparticles as coupled contrast agents, Nat. Commun. 1 (2010) 41.

[69] M.F. Kircher, A. de la Zerda, J.V. Jokerst, C.L. Zavaleta, P.J. Kempen, E. Mittra, K. Pitter, R.M. Huang, C. Campos, F. Habte, R. Sinclair, C.W. Brennan, I.K. Mellinghoff, E.C. Holland, S.S. Gambhir, A brain tumor molecular imaging strategy using a new triple-modality MRI-photoacoustic-Raman nanoparticle, Nat. Med. 18 (2012) 829-834.

[70] M.V. Yigit, L.Y. Zhu, M.A. Ifediba, Y. Zhang, K. Carr, A. Moore, Z. Medarova, Noninvasive MRI-SERS imaging in living mice using an innately bimodal nanomaterial, ACS Nano 5 (2011) 1056-1066.

[71] T. Zhou, B.Y. Wu, D. Xing, Bio-modified Fe_3O_4 core/Au shell nanoparticles for targeting and multimodal imaging of cancer cells, J. Mater. Chem. 22 (2012) 470-477.

[72] X. Niu, H. Chen, Y. Wang, W. Wang, X. Sun, L. Chen, Upconversion fluorescence-SERS dual-mode tags for cellular and in vivo imaging, ACS Appl. Mater. Inter. 6 (2014) 5152-5160.

[73] M. Kacenka, O. Kaman, J. Kotek, L. Falteisek, J. Cerny, D. Jirak, V. Herynek, K. Zacharovova, Z. Berkova, P. Jendelova, J. Kupcik, E. Pollert, P. Veverka, I. Lukes, Dual imaging probes for magnetic resonance imaging and fluorescence microscopy based on perovskite manganite nanoparticles, J. Mater. Chem. 21 (2011) 157-164.

[74] X.M. Tian, Y.Z. Shao, H.Q. He, H. Liu, Y.Y. Shen, W.L. Huang, L. Li, Nanoamplifiers synthesized from gadolinium and gold nanocomposites for magnetic resonance imaging, Nanoscale 5 (2013) 3322-3329.

[75] B. Kang, L.A. Austin, M.A. El-Sayed, Real-time molecular imaging throughout the entire cell cycle by targeted plasmonic-enhanced Rayleigh/Raman spectroscopy, Nano Lett. 12 (2012) 5369-5375.

[76] J.W. Chan, D.K. Lieu, T. Huser, R.A. Li, Label-free separation of human embryonic stem cells and their cardiac derivatives using Raman spectroscopy, Anal. Chem. 81 (2009) 1324-1331.

[77] S. Verrier, I. Notingher, J.M. Polak, L.L. Hench, In situ monitoring of cell death using Raman microspectroscopy, Biopolymers 74 (2004) 157-162.

[78] N.J. Crane, T.S. Brown, K.N. Evans, J.S. Hawksworth, S. Hussey, D.K. Tadaki, E.A. Elster, Monitoring the healing of combat wounds using Raman spectroscopic mapping, Wound Repair Regen. 18 (2010) 409-416.

[79] L. Tirinato, C. Liberale, S. Di Franco, P. Candeloro, A. Benfante, R. La Rocca, L. Potze, R. Marotta, R. Ruffilli, V.P. Rajamanickam, M. Malerba, F. De Angelis, A. Falqui,

E. Carbone, M. Todaro, J.P. Medema, G. Stassi, E. Di Fabrizio, Lipid droplets: a new player in colorectal cancer stem cells unveiled by spectroscopic imaging, Stem Cells 33 (2015) 35-44.

Table 1.1 Raman spectroscopy in cellular investigation

Application	Exemplary Observations (bands, cm^{-1})	Reference
Cell cycle	G1 (511, 658, 845, 1322), S (1541, 1600), G2/M (1273)	[75]
Stem cell differentiation	hESCs had higher DNA and RNA contents than differentiated cells (785, 811, 1090, 1320)	[76]
Cell death	Degradation of proteins (1005, 1342), DNA breakdown (788), formation of lipid vesicles (1303, 1660)	[77]
Wound healing	Collagen content change (1665/1445 ratio)	[78]
Cancer detection	Excessive presence of lipid droplets (1300, 2850) in colorectal cancer stem cells	[79]

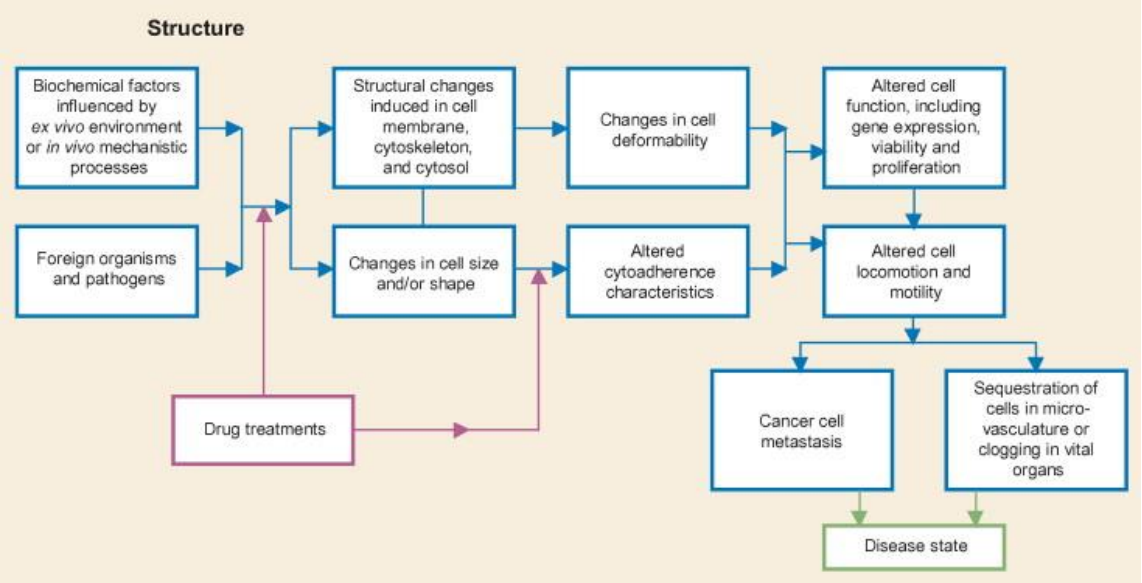


Figure 1.1 Schematic of chemo-biomechanical pathways influencing connections among subcellular structure, cell biomechanics, motility and disease state (image adapted from ref [2]).

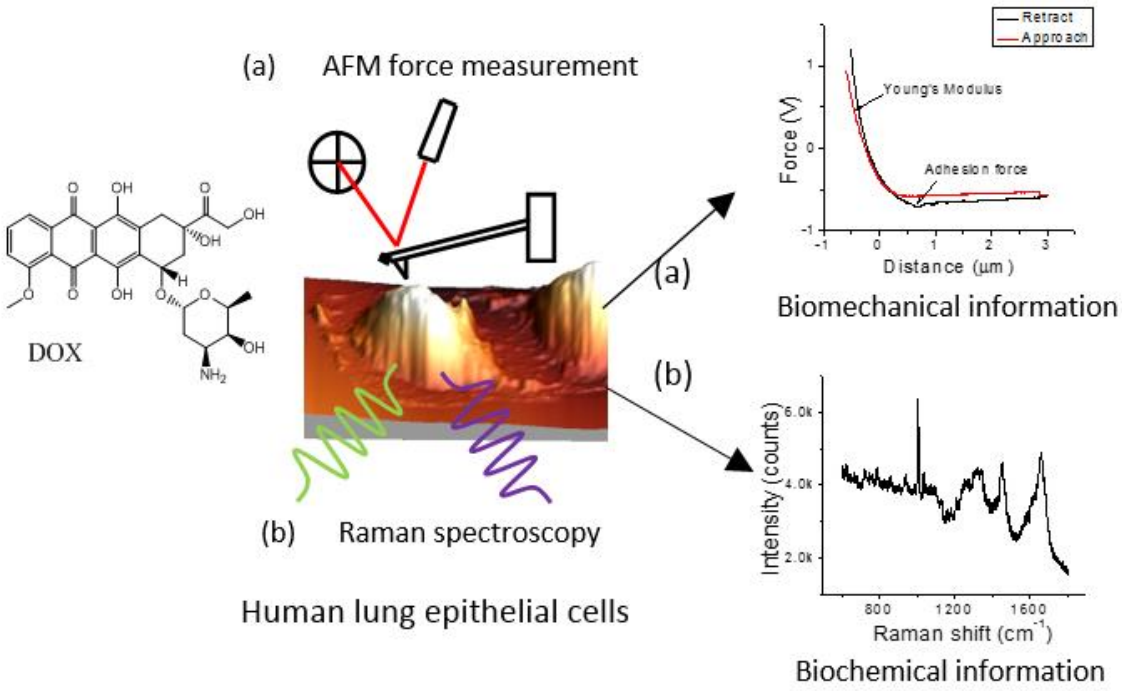


Figure 1.2 Biophysical and biochemical responses of human lung epithelial cells to doxorubicin anti-cancer drugs measured by AFM and Raman spectroscopy.

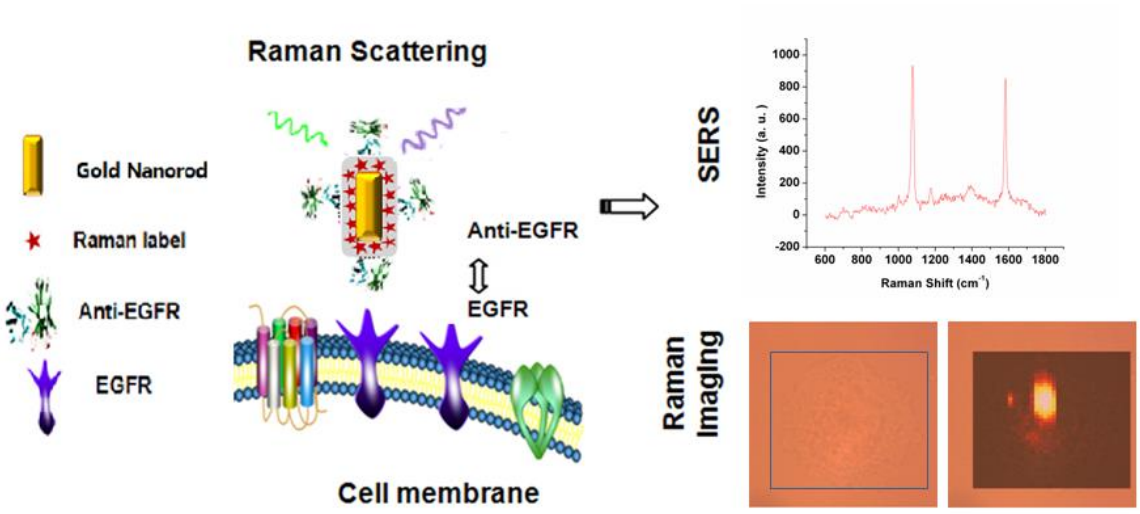


Figure 1.3 Schematic illustration of EGFR detection on single human cancer cells by SERS.

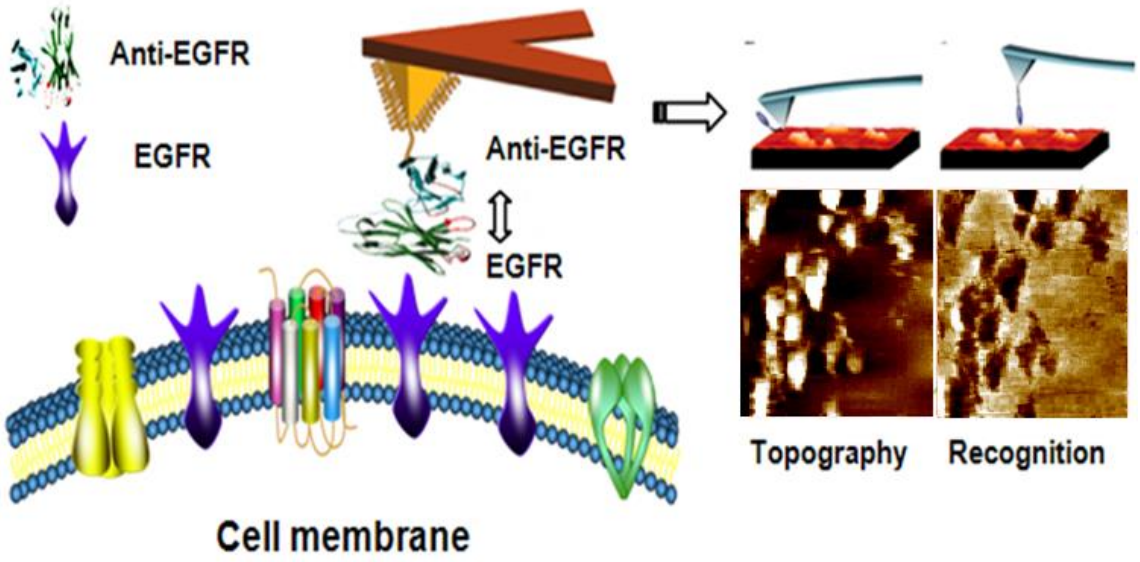


Figure 1.4 Schematic of interaction between EGFR and anti-EGFR measured by TREC imaging.

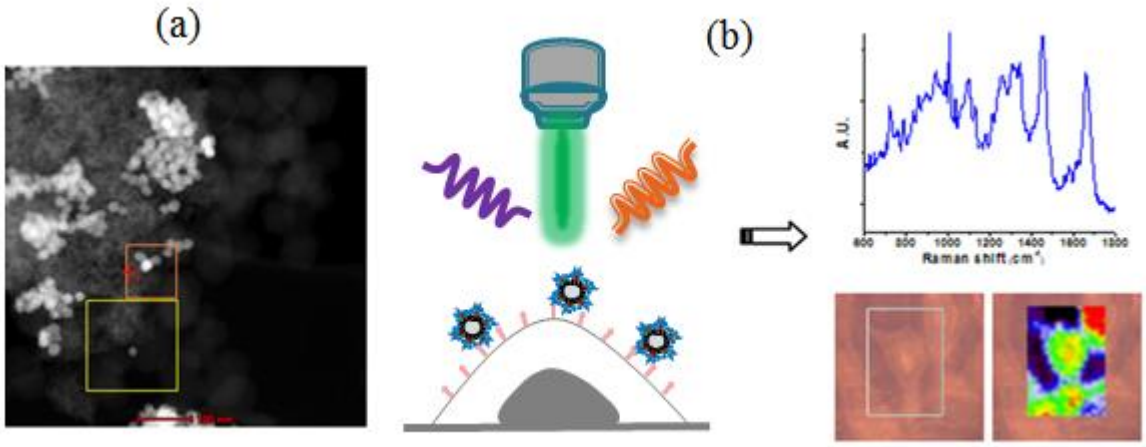


Figure 1.5 (a) STEM image of the Gd-Au nanoprobe. (b) Schematic of the SERS detection of EGFR using Gd-Au nanoprobes.

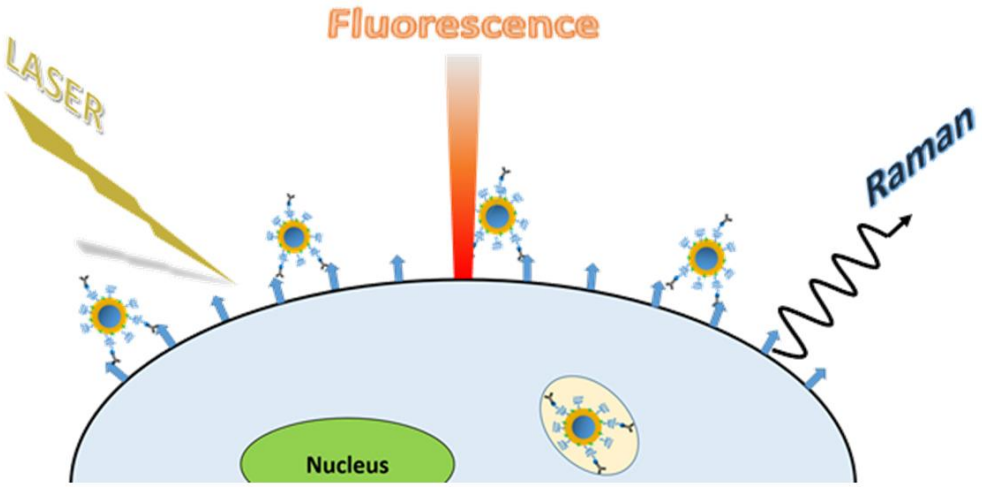


Figure 1.6 Schematic illustration of SERS-fluorescence bimodal nanoprobes for GPR120 detection.

CHAPTER 2

NONINVASIVE DETECTION OF BIOMECHANICAL AND BIOCHEMICAL RESPONSES OF HUMAN LUNG CELLS TO SHORT TIME CHEMOTHERAPY EXPOSURE USING AFM AND CONFOCAL RAMAN SPECTROSCOPY[1]

2.1 ABSTRACT

Cellular biomechanical properties including cell elasticity and cell adhesion are regarded as criteria to differentiate cancer cells and normal cells. In this study, the biomechanical properties including the Young's modulus and adhesion force of human lung adenocarcinoma epithelial cell line A549 and non-cancerous human primary small airway epithelial cells (SAECs) were measured by using atomic force microscopy (AFM). It was found that normal SAECs are stiffer and more adhesive than cancerous A549 cells. Upon treatment with anti-cancer drug doxorubicin (DOX) for a short time (4 hr), both biomechanical properties of A549 cells were found to be increased while those of SAECs were decreased, implying that DOX induced response mechanisms are different between the two types of cells (cancerous vs. primary cells). Using Raman spectroscopy, we measured the changes in (sub)cellular biochemical compositions of both cell types before and after DOX exposure. Our ultimate goal is to find out the potential relationship between the changes in biomechanics and biochemical compositions of lung epithelial cells in response to anti-cancer drugs.

2.2 INTRODUCTION

In past decades, considerable cancer research has been carried out using traditional biological methods that are based upon molecular genetics and gene signaling, but the roles

[1] L. Xiao, M. Tang, Q. Li, A. Zhou, Non-invasive detection of biomechanical and biochemical responses of human lung cells to short time chemotherapy exposure using AFM and confocal Raman spectroscopy, Anal. Methods 5 (2013) 874-879.

of cell biomechanics have been ignored, regardless of the mechanical nature of the invasion process of cancer cells [1]. Mechanical properties regulate tumor cell functions such as tumor progression, cell proliferation, motility, migration, invasion and metastasis [2, 3]. Recently, cyto-mechanical properties have received increasing attention as a potential biophysical marker for new cancer diagnostics and therapeutics [4, 5]. The quantitative analysis of mechanical profiles at the single-cell level can provide additional information that is usually not available in traditional cell biology approaches but may be crucial to assess and understand tumor prognosis and response to chemotherapy. Normal human mammary epithelial cells (MCF 10) are found to be less deformable than malignant human breast cancer epithelial cells (MCF 7); moreover, phorbol ester TPA-treated MCF-7 cells, which have an 18-fold increase in the invasiveness and metastatic efficiency, are even more deformable than before treatment [6].

In vitro studies have shown that cellular biomechanics including cell stiffness and adhesion of cancer cells are often lower than that of their normal counterparts—this has been considered as a target to early diagnosis of cancers [7, 8]. In addition, interactions between cancer cells and anti-cancer drugs have recently emerged as topics of particular interest, because understanding the mechanisms of biomechanics as well as biochemistry in cell function would facilitate the understanding of biology of cancers and further the development of new anti-cancer drugs. In addition to biomechanics, anti-cancer agents also cause subcellular biochemical changes such as the regulation of DNA, protein and lipids [9]. Studies have shown that chemotherapy would increase the stiffness of cancer cells [10, 11]. However, little is known about whether anti-cancer drug chemotherapy would lead to synergistic cellular biomechanical and biochemical responses, or in return, how these

cellular responses would influence the chemotherapy efficiency. This knowledge is particularly important to further determine the role of biomechanics in cancer development and further elucidate the potential relationship between biomechanics properties and cellular composition changes induced by anti-cancer drugs.

Atomic force microscopy (AFM) [12], working on the basis of the interaction between a sharp cantilever tip and the sample surface, has become a powerful tool for *in situ* imaging biological samples in (near) physiological conditions, and quantitation of biomechanical properties of living cells [13-16]. Cross et al. found that metastatic cancer cells are not only much softer, but also less adhesive than benign cells by measuring living human cells derived from patients [8, 16]. Lam et al. observed an increase in cell stiffness of leukemia cells, which may be due to dynamic changes in the actin cytoskeleton, when exposed to anti-cancer drug dexamethasone or daunorubicin [10]. Raman spectroscopy, based on the inelastic scattering of the incidence laser on target molecules, is a molecular vibrational spectroscopic technique that can detect molecular structural information used to identify specific (sub)cellular biochemical compositions in living cells [17]. Recently, Raman spectroscopy has been successfully applied to detect biochemical composition changes in cancer cells under anti-cancer drug treatments [18, 19].

Measurement of the biomechanical and biochemical responses of normal vs. cancerous cells to known chemotherapeutic agents is needed to further understand their cell-drug interaction mechanism. Doxorubicin (DOX) is a well-established anti-cancer drug widely used in the chemotherapy of a wide range of cancers such as breast carcinoma, hematological malignancies and lung cancer [20]. By intercalation into the nucleus [21], DOX inhibits the process of DNA replication and macromolecular biosynthesis, and

consequently lead to tumor cell apoptosis. In addition to leading to the apparent inhibition to cellular elements, DOX also induces changes in cellular cytoskeleton (actin filaments) [22, 23]. There are substantial studies on the interaction between DOX and tumor cells [24-26]. However, to our knowledge, no work specifically focused on DOX-induced biomechanical and biochemical changes in cancer cells has been reported. In this study, we applied AFM and Raman spectroscopy to detect the responses of lung carcinoma cell A549 and normal primary small airway epithelial cells (SAECs), to short time (4hr) exposure at the single cell level. Short-time chemotherapy exposure (e.g., 4 hr) has been reported to be sufficient for cells to show distinct responses and develop preliminary drug resistance [27]. As a matter of fact, anti-cancer drug therapy would not only interact with cancer cells but also may influence physiological function of normal (healthy) cells. It is of particular interest to investigate how normal and cancer cells respond to anti-cancer drug treatment.

2.3 MATERIALS AND METHODS

2.3.1 Preparation of A549 cells and SAECs

Human lung carcinoma A549 cells (ATCC, USA) were cultured in F-12k medium containing 5% fetal bovine serum and 1% penicillin-streptomycin (both from Invitrogen) at 37 °C with 5% CO_2 in a humidified atmosphere. Cells (approximately 10^6 cells/ml) were passaged at 80-90% confluence and used for experiments. Human small airway epithelial cells (SAECs) were cultured in SAGM medium containing growth factors (BPE, hydrocortisone, hEGF, epinephrine, insulin, triiodothyronine, transferrin, gentamicin/amphotericin-B, retinoic acid and BSA-FAF) at 37 °C with 5% CO_2 in a humidified atmosphere.

For AFM experiments, the cells were seeded on poly-L-lysine coated glass bottom Petri dishes (MatTek Corp. USA) at a density of $1x10^5$ cells per 2 mL of media. To minimize background in Raman spectroscopy, a density of $1x10^5$ cells per 2 mL of media was placed on a cleaned magnesium fluoride (MgF_2) optical window (United Crystals Co., Port Washington, NY).

2.3.2 Anticancer drug Doxorubicin (DOX) treatment

DOX (Sigma-Aldrich, St. Louis, MO) was dissolved in water and stored at 4 °C as a stock solution (8 μM) within one week prior to use. A549 cells and SAECs were incubated for 24 hr after seeding and then treated by DOX for 4 hr at a final concentration of 70 nM (IC_{50} of A549 [28]). Drugs were washed away after 4 hr and cells were kept for 24-hr incubation. Cells were then ready for measurement.

2.3.3 Atomic Force Microscopy (AFM) measurement

In order to conduct AFM measurements, cells were prepared in one of two ways. (1) To obtain the topography and deflection images, cells were fixed with 4% paraformaldehyde for 10 min, and then rinsed by $1\times Ca^{2+}/Mg^{2+}$-free phosphate buffered saline (PBS) buffer. Finally, the cells were imaged in PBS buffer. (2) To measure biomechanical properties such as cell elasticity and adhesion, *in situ* measurements were applied. Cells were measured in culture media without any pretreatment. The whole measurement was accomplished within 1 hr, so that the experiment condition could be considered reflective of the physiological condition of living cells.

Contact mode AFM controlled by Picoview software (Picoplus, Agilent Technologies, USA) was applied on A549 cells and SAECs at room temperature in either PBS buffer (0.01 M, pH 7.4) or cell culture media. AFM deflection images of cells were

chosen in the imaging experiment. In the force measurement, sharp silicon nitride AFM probes (tip radius, 20nm) were employed (Bruker Corp., USA). The spring constant of AFM tips were calibrated as 0.10~0.11 N/m and Deflection Sensitivities were 45~50 nm/V, using Thermo K Calibration (Agilent Technologies, USA). The approaching/retracting speed of the AFM tip during the force curve measurement was 6 μm/s.

For biomechanics measurement, force-distance curves were recorded by AFM instrument to get cell elasticity (Young's Modulus, E) and adhesion force (maximum pull force between AFM tip and cell surface during the retracting process of the AFM probe) of individual cells. For each cell line, 12 cells were measured with over 15 force-distance curves per cell to avoid spurious results [8]. Young's modulus and adhesion force were calculated via the Scanning Probe Image Processor (SPIP) software (Image Metrology, Denmark) by converting the force-distance curves to force-separation curves and fitting the Sneddon variation of Hertz model [29-31], which describes conical tips indenting elastic samples.

Statistical analysis of the biomechanical property data were conducted by one-way ANOVA (Origin9, USA). Significance of means comparison was evaluated by Tukey's range test. Same statistical analysis were performed in all chapters of this dissertation.

2.3.4 Fluorescence imaging of A549 cells and SAECs

Cell samples were stained for cytoskeletal and nuclear architecture according to manufacturer's protocol (Invitrogen). For staining, (1) cells were fixed with a 3.7% formaldehyde (Electron Microscopy Sciences) solution in PBS for 10 min at room temperature (RT); (2) cells were treated with 0.1% Triton X-100 (Sigma) in PBS for 3 min at RT; (3) incubated with 1% bovine serum albumin (BSA) in PBS for 30 min at RT; (4)

incubated with 1 unit of phallotoxins (cytoskeleton dye) in PBS for 30 min at RT; (5) incubated with 300 nM of DAPI dihydrochloride (nucleic acid dye) in PBS for 3 min at RT. Cell samples were washed with PBS for two times between each step. Then stained samples were stored in PBS at 4^{o}C prior to AFM/FL observation.

Fluorescence images were collected by an Olympus IX71 inverted fluorescence microscope equipped with an Olympus DP30BW CCD camera. Images were collected by Olympus DP-BSW Controller and Manager Software. Phase contrast images were acquired with a 40× Phase lens (Olympus), Our IX71 fluorescence microscope was coupled to a PicoPlus atomic force microscope (called AFM/FL) via a specially designed stage (Agilent Technologies).

2.3.5 Data acquisition for Raman Micro-spectroscopy

The Raman spectra of A549 cells and SAECs were measured by a Renishaw inVia Raman spectrometer (controlled by WiRE 3.0 software) connected to a Leica microscope (Leica DMLM), equipped with a 785 nm near-IR laser (laser spot 10 × 3 μm line) that was focused through a 63 × NA = 0.90 water immersion objective. 520.5 ± 0.1 cm^{-1} was the standard calibration peak for the spectrometer with silicon mode at a static spectrum. Samples of SAECs and A549 cells were cultured on magnesium fluoride (MgF_2) and then imaged in Earle's Balanced Salt Solution (EBSS). Raman spectra between 600 and 1800 cm^{-1} wavenumber were then recorded for 1 accumulation at 20s laser exposure at static mode. Three different positions (nucleus, cytoplasm and membrane) in a cell were measured. Thirty-two spectra were used to calculate an average for each group.

2.3.6 Raman data analysis

Cosmic rays in raw spectra were removed using Renishaw Wire 3.3 software. Because Raman spectra are affected by the physical properties of the samples and background noise, it is necessary to perform mathematical processes to reduce systematic noise, and enhance resolution of chemical compositions from target cells. In this work, Raman spectra were smoothed by moving average smoothing to filter high-frequency noise. Each Raman spectrum consists of many variables, but only a fraction of the variables contains useful information for cell classification. Principal component analysis (PCA) [32] was performed on the data set with the goal of defining a new dimensional space in which the major variance in the original data set can be captured and represented by only a few principal component (PC) variables and allowing the most important variables responsible for these differences to be identified. In this work, PCA methods based on moving average smoothing were performed as an attempt to extract useful information from raw spectral data, and firstly applied to examine the differences among the groups of untreated and treated SAEC and A549 at three locations (nucleus, cytoplasm and cell membrane) of cells. All algorithms were implemented in Matlab R2010b (Mathworks Inc., Natick, USA).

2.3.7 Cell viability test

The cell viability was analyzed using LIVE/DEAD Viability/Cytotoxicity Assay Kit (Invitrogen) according to the manufacturer's instruction. Briefly, (1) Cells were cultured in poly-D-lysine coated glass-bottom dishes (MatTek Cop. USA) and MgF2 substrate which was put in Petri dishes for 24 hr; (2) cells were then washed with PBS twice; (3) 2 ml of mixed solution of 2 μM Calcein AM and 4 μM ethidium homodimer-1 (EthD-1) (both from Invitrogen) was added directly to cells, and incubated cells for 30 min

at room temperature; (5) cells were imaged using fluorescence microscope with DP30BW CCD camera (Olympus IX71) to analyze the relative proportion of live/dead cells. Here, a 10× objective was used to observe fluorescence. Calcein AM is well retained within live cells producing green fluorescence; however, EthD-1 enters cells with damaged membrane and binds to nucleic acids, thereby producing a red fluorescence in dead or membrane-damaged cells. Therefore, the live/dead cells were differentiated visually.

2.4 RESULTS AND DISCUSSION

2.4.1 Biomechanical properties and morphologies of A549 cells and SAECs

In this study, cancerous A549 cells and normal (primary) SAECs are imaged with AFM directly in the culture media under physiological condition. Apparent differences in cell morphology and ultrastructure between the two cell types can be observed in AFM deflection images—primary SAECs are generally larger and more affluent in filamentous cell junctions than the cancerous A549 cells (Figure 2.1). Furthermore, two biomechanical properties, cell elasticity (Young's modulus, E) and cell adhesion force, are quantitated by AFM force-distance measurements. The average Young's modulus of A549 cells and SAECs are measured to be 12.007±4.381 kPa (n=210) and 25.227±9.274 kPa (n=187), respectively. The average adhesion force of A549 cells and SAECs are measured to be 0.506±0.152 nN (n=190) and 0.819±0.243 nN (n=187), respectively. Both Young's modulus and adhesion force for A549 cells (tumor cell) are significantly smaller ($p<0.01$, Figure 2.2) than that for SAECs (non-tumor cell); which is consistent with reported studies [16, 33]. This result means tumor cells were softer and less adhesive than non-tumor cells.

2.4.2 Biomechanical responses to chemotherapy

In order to study the morphological and biomechanical responses of A549 cells and SAECs to short time chemotherapy, cells are exposed to 70 nM (IC_{50} for A549 cells) [34] DOX for 4 hr, followed by AFM force measurement to detect the alteration of cell elasticity and cell adhesion. The results are shown in Figure 2.2. Young's moduli for A549 cells and SAECs with DOX treatment (4 hr) are measured to be 19.756±8.489 kPa (n=195) and 20.486±9.066 kPa (n=180), respectively. Adhesion forces for A549 cells and SAECs with DOX treatment are measured to be 0.839±0.291 nN (n=179) and 0.769±0.248 nN (n=195), respectively. Young's modulus of A549 cells significantly ($p<0.01$) increases with DOX treatment, whereas that of SAECs decreases, resulting in the reduction of difference in cell elasticity between the two cell types (the difference is not statistically significant, Figure 2.2a). The change in cell elasticity induced by DOX exposure might be attributed to the rearrangement of cytoskeleton, especially to the reorganization of intermediate filaments and actin filaments, which have been identified as the main determinants of cell viscoelasticity [35]. It should be noted that although, consistent with previous cancer studies [10, 11], the elasticity of tumor cells increases after chemotherapy, that of benign cells decreases possibly due to alterations in cytoskeleton with focal loss of contractile elements, which has been seen in cardiomyocytes [22]. In addition, the alteration in cell adhesion between the control and DOX treated cells follows the same trend as that of Young's modulus—adhesion force of A549 cells increases under DOX treatment, while that of SAECs decreases. This observed opposite biomechanical responses to DOX treatment between cancerous and primary cells imply that the regulation of (actin) cytoskeleton or related signaling pathways may be different between these two cell types

[36]. The response in cell adhesion could be related to the variation of adhesive macromolecules (e.g. proteins, polysaccharides) on the cell surface, which can be probed by AFM force spectroscopy [30]. In another word, DOX treatment reduced the biomechanical differences between A549 cells and SAECs.

By applying the coupled AFM/Fluorescence microscope system, we are able to simultaneously obtain AFM, fluorescence and optical phase contrast images of the same cell (Figure 2.3). It is found that A549 cells are with less organized cytoskeleton structures (e.g. filamentous actin) than SAECs; upon DOX treatment, both cell lines exhibit apparent change in cytoskeleton, confirming the results of biomechanical tests. Moreover, phase contrast images for DOX treated A549 and SAEC displayed dark spots within cells that indicated the presence of intracellular vesicles, which is known to occur during the apoptosis induced by DOX [37].

2.4.3 Cellular biochemical changes induced by chemotherapy

In addition to cell morphology and cellular biomechanics, cancerous A549 cells and primary SAECs, when exposed to DOX, also present differences in biochemical composition, which are detected by Raman spectroscopy. Since DOX interacts with cells primarily at nucleus, we mainly focus on the spectra collected on nucleus area (data of cytoplasm and membrane area are shown in Figure 2.4) of each cell type (via confocal setting in Raman measurement). Averaged Raman spectra of A549 cell and SAECs control and DOX treatment groups at nucleus are shown in Figure 2.5a. Major Raman bands for cellular biopolymers (i.e. nucleic acids, proteins, lipids and carbohydrates) are listed in Table 2.1. Comparing with SAEC control group, the Raman peaks of A549 control exhibited a pronounced rise at 672 cm^{-1} (C-S stretching mode of cytosine), 720 cm^{-1} (DNA),

786 cm^{-1} (DNA & phosphdiester bands DNA) and 813 cm^{-1} (phosphodiester bands RNA). This result would be consistent with previous findings that DNA is more abundant in cancer cells than normal cells due to the more active mitosis and cellular turnover [38]. Upon DOX treatments, spectroscopic differences between A549 cells and SAECs in DNA-related Raman peaks are reduced, because DOX selectively targets A549 cells and prevent DNA replication, lowering DNA level in A549 cells. This observation that intensities of DNA peaks decrease after anticancer drug exposure is also consistent with previous studies [9, 39]. Besides the nucleic acids, distinctions in proteins (937, 1006, 1034 cm^{-1}) and lipids (1450 cm^{-1}) are also observed in the Raman spectra; cancerous A549 cells are less affluent in proteins and lipids than primary SAECs. Unlike DNA, DOX treatment leads to elevated protein and lipid levels in both A549 cells and SAECs.

Principal component analysis (PCA) can further distinguish the spectral differences for both cell types before and after DOX exposure. In Figure 2.5b, an evident separation of clusters of SAEC and A549 can be observed in PCA score plot, where the 1st principal component incorporated 47% of the variance and the 2nd component 26%. Moreover, it is noticed that SAEC clusters (with and without DOX treatment) sit closely each other, compared to obvious separation of the two clusters of A549 control and A549-DOX group. This observation implies the less effective impact of short term (4 hr) exposure of DOX on the changes of SAEC spectra than those on A549 cells. PCA plots for cytoplasm and membrane areas are presented in Figure 2.4.

In order to quantitatively identify how DOX treatment influenced the variation in cellular bio-components, we selected some specific Raman peaks (labeled in Figure 2.5a) related to DNA, proteins, lipids and compared the changes in their spectral intensities. 720

cm^{-1} band is assigned to guanine band of DNA, 1006 cm^{-1} band the symmetric ring breathing phenylalanine band in protein, and 1450 cm^{-1} the CH_2 deformation of lipids and proteins [33]. Since Raman intensities have a linear dependence on the concentrations of particular molecular bonds of cellular bio-components, the changes in their characteristic peak intensities reflect the alterations of corresponding biochemical compositions of cells. As shown in Figure 2.6, for A549 and SAEC cells upon DOX exposure, Raman intensity for DNA (720 cm^{-1}) presented a slight decrease (SAEC cells didn't show obvious DNA changes), whereas the peak intensities for protein (1006 cm^{-1}) and lipid (1450 cm^{-1}) exhibited a considerable increase (6% ~12%). The decrease in DNA Raman signal and the increase in protein Raman signal could be caused by the DOX-induced cell apoptosis, which leads to the degradation of DNA [40] as well as the up-regulation of p53, Bax and MDM2 proteins in cell nucleus [41]. The increase in lipid related Raman peak is related to the presence of intracellular lipid vesicles at cell surface (e.g. phosphatidylserine, granule) [9, 42], which also are confirmed by phase contrast imaging (Figure 2.3). Furthermore, as Figure 2.6 shows, the larger percentages of Raman intensity changes for A549 cells indicates that cancer cells are more sensitive to DOX treatment, comparing with normal SAECs. Fluorescence cell viability analysis (Figure 2.7) shows more A549 cells are found dead than SAEC cells after 4 hr DOX treatment, although most are still alive under experimental condition.

2.5 CONCLUSIONS

In conclusion, we applied AFM and Raman micro-spectroscopy to monitor the cellular biomechanical and biochemical responses of cancerous (A549) and primary (SAECs) human lung epithelial cells to short chemotherapy exposure (4 hr). A549 cells

and SAECs show opposite variation in cell stiffness and cell adhesion—A549 cells increasing while SAECs decreasing—with the treatment of anticancer agent doxorubicin. A reduction in DNA and a rise in protein and lipid concentrations, due to the process of DOX-induced cell apoptosis, are observed from Raman spectral changes. Our study indicates cellular biomechanics, as a biomarker for cancer therapy, provides new prospective to investigate the potential linkage between alterations of biomechanics and cell biochemistry induced by cell-drug interaction. As a result, these new findings would benefit new anti-cancer drug development. In order to fully understand how the DOX treatments affect the cellular biomechanical and biochemical responses of human lung cells, more work has to be done in a dose-dependent and time-dependent manner.

2.6 REFERENCES

[1] C.T. Mierke, The biomechanical properties of 3d extracellular matrices and embedded cells regulate the invasiveness of cancer cells, Cell Biochem. Biophys. 61 (2011) 217-236.

[2] F. Michor, J. Liphardt, M. Ferrari, J. Widom, What does physics have to do with cancer?, Nat. Rev. Cancer 11 (2011) 657-670.

[3] H.M. Yu, J.K. Mouw, V.M. Weaver, Forcing form and function: biomechanical regulation of tumor evolution, Trends Cell. Biol. 21 (2011) 47-56.

[4] L. Wilson, S. Cross, J. Gimzewski, J.Y. Rao, Nanocytology: a novel class of biomarkers for cancer management, IDrugs 13 (2010) 847-851.

[5] S. Suresh, Biomechanics and biophysics of cancer cells, Acta Biomater. 3 (2007) 413-438.

[6] J. Guck, S. Schinkinger, B. Lincoln, F. Wottawah, S. Ebert, M. Romeyke, D. Lenz, H.M. Erickson, R. Ananthakrishnan, D. Mitchell, J. Kas, S. Ulvick, C. Bilby, Optical

deformability as an inherent cell marker for testing malignant transformation and metastatic competence, Biophys. J. 88 (2005) 3689-3698.

[7] S. Suresh, Nanomedicine - elastic clues in cancer detection, Nat. Nanotechnol. 2 (2007) 748-749.

[8] S.E. Cross, Y.S. Jin, J. Rao, J.K. Gimzewski, Nanomechanical analysis of cells from cancer patients, Nat. Nanotechnol. 2 (2007) 780-783.

[9] T.J. Moritz, D.S. Taylor, D.M. Krol, J. Fritch, J.W. Chan, Detection of doxorubicin-induced apoptosis of leukemic T-lymphocytes by laser tweezers Raman spectroscopy, Biomed. Opt. Express 1 (2010) 1138-1147.

[10] W.A. Lam, M.J. Rosenbluth, D.A. Fletcher, Chemotherapy exposure increases leukemia cell stiffness, Blood 109 (2007) 3505-3508.

[11] S.E. Cross, Y.S. Jin, Q.Y. Lu, J.Y. Rao, J.K. Gimzewski, Green tea extract selectively targets nanomechanics of live metastatic cancer cells, Nanotechnology 22 (2011) 215101.

[12] G. Binnig, C.F. Quate, C. Gerber, Atomic force microscope, Phys. Rev. Lett. 56 (1986) 930-933.

[13] E. A-Hassan, W.F. Heinz, M.D. Antonik, N.P. D'Costa, S. Nageswaran, C.A. Schoenenberger, J.H. Hoh, Relative microelastic mapping of living cells by atomic force microscopy, Biophys. J. 74 (1998) 1564-1578.

[14] M. Radmacher, M. Fritz, C.M. Kacher, J.P. Cleveland, P.K. Hansma, Measuring the viscoelastic properties of human platelets with the atomic force microscope, Biophys. J. 70 (1996) 556-567.

[15] M. Lekka, P. Laidler, D. Gil, J. Lekki, Z. Stachura, A.Z. Hrynkiewicz, Elasticity of normal and cancerous human bladder cells studied by scanning force microscopy, Eur. Biophys. J. Biophy. 28 (1999) 312-316.

[16] S.E. Cross, Y.S. Jin, J. Tondre, R. Wong, J. Rao, J.K. Gimzewski, AFM-based analysis of human metastatic cancer cells, Nanotechnology 19 (2008) 384003.

[17] C.A. Owen, I. Notingher, R. Hill, M. Stevens, L.L. Hench, Progress in Raman spectroscopy in the fields of tissue engineering, diagnostics and toxicological testing, J. Mater. Sci.-Mater. Med. 17 (2006) 1019-1023.

[18] H. Nawaz, F. Bonnier, P. Knief, O. Howe, F.M. Lyng, A.D. Meade, H.J. Byrne, Evaluation of the potential of Raman microspectroscopy for prediction of chemotherapeutic response to cisplatin in lung adenocarcinoma, Analyst 135 (2010) 3070-3076.

[19] H. Nawaz, F. Bonnier, A.D. Meade, F.M. Lyng, H.J. Byrne, Comparison of subcellular responses for the evaluation and prediction of the chemotherapeutic response to cisplatin in lung adenocarcinoma using Raman spectroscopy, Analyst 136 (2011) 2450-2463.

[20] F. Aoudjit, K. Vuori, Integrin signaling in cancer cell survival and chemoresistance, Chemother. Res. Pract. 2012 (2012) 283181.

[21] F.A. Fornari, J.K. Randolph, J.C. Yalowich, M.K. Ritke, D.A. Gewirtz, Interference by doxorubicin with DNA unwinding in Mcf-7 breast tumor cells, Mol. Pharmacol. 45 (1994) 649-656.

[22] O.J. Arola, A. Saraste, K. Pulkki, M. Kallajoki, M. Parvinen, L.M. Voipio-Pulkki, Acute doxorubicin cardiotoxicity involves cardiomyocyte apoptosis, Cancer Res. 60 (2000) 1789-1792.

[23] W. Lewis, B. Gonzalez, Anthracycline effects on actin and actin-containing thin filaments in cultured neonatal rat myocardial cells, Lab Invest. 54 (1986) 416-423.

[24] Q. Zhang, R. Pu, Y. Du, Y.F. Han, T. Su, H.Y. Wang, G.W. Cao, Non-coding RNAs in hepatitis B or C-associated hepatocellular carcinoma: potential diagnostic and prognostic markers and therapeutic targets, Cancer Lett. 321 (2012) 1-12.

[25] C.H. Takimoto, A. Awada, Safety and anti-tumor activity of sorafenib (Nexavar®) in combination with other anti-cancer agents: a review of clinical trials, Cancer Chemoth. Pharm. 61 (2008) 535-548.

[26] J. Sterz, I. von Metzler, J.C. Hahne, B. Lamottke, J. Rademacher, U. Heider, E. Terpos, O. Sezer, The potential of proteasome inhibitors in cancer therapy, Expert Opin. Inv. Drug. 17 (2008) 879-895.

[27] A. Sobrero, C. Aschele, R. Rosso, A. Nicolin, J.R. Bertino, Rapid development of resistance to antifolates in vitro—possible clinical implication, J. Natl. Cancer. I. 83 (1991) 24-28.

[28] K.N. Kashkin, E.A. Musatkina, A.V. Komelkov, I.A. Favorskaya, E.V. Trushkin, V.A. Shleptsova, D.A. Sakharov, T.V. Vinogradova, E.P. Kopantzev, M.V. Zinovyeva, O.V. Kovaleva, I.B. Zborovskaya, A.G. Tonevitsky, E.D. Sverdlov, Expression profiling and putative mechanisms of resistance to doxorubicin of human lung cancer cells, Dokl. Biochem. Biophys. 430 (2010) 20-23.

[29] S. Ian N, The relation between load and penetration in the axisymmetric boussinesq problem for a punch of arbitrary profile, Int. J. Eng. Sci. 3 (1965) 47-57.

[30] B.C. van der Aa, R.M. Michel, M. Asther, M.T. Zamora, P.G. Rouxhet, Y.F. Dufrene, Stretching cell surface macromolecules by atomic force microscopy, Langmuir 17 (2001) 3116-3119.

[31] M. Radmacher, Measuring the elastic properties of biological samples with the AFM, IEEE Eng. Med. Biol. 16 (1997) 47-57.

[32] L. Notingher, G. Jell, P.L. Notingher, I. Bisson, O. Tsigkou, J.M. Polak, M.M. Stevens, L.L. Hench, Multivariate analysis of Raman spectra for in vitro non-invasive studies of living cells, J. Mol. Struct. 744 (2005) 179-185.

[33] Y.Z. Wu, G.D. McEwen, S. Harihar, S.M. Baker, D.B. DeWald, A.H. Zhou, BRMS1 expression alters the ultrastructural, biomechanical and biochemical properties of MDA-MB-435 human breast carcinoma cells: an AFM and Raman microspectroscopy study, Cancer Lett. 293 (2010) 82-91.

[34] K.N. Kashkin, E.A. Musatkina, A.V. Komelkov, I.A. Favorskaya, E.V. Trushkin, V.A. Shleptsova, D.A. Sakharov, T.V. Vinogradova, E.P. Kopantzev, M.V. Zinovyeva, O.V. Kovaleva, I.B. Zborovskaya, A.G. Tonevitsky, E.D. Sverdlov, Expression profiling and putative mechanisms of resistance to doxorubicin of human lung cancer cells, Dokl. Biochem. Biophys. 430 (2010) 20-23.

[35] A.R. Bausch, K. Kroy, A bottom-up approach to cell mechanics, Nat. Phys. 2 (2006) 231-238.

[36] C. Alberti, Cytoskeleton structure and dynamic behaviour: quick excursus from basic molecular mechanisms to some implications in cancer chemotherapy, Eur. Rev. Med. Pharmacol. Sci. 13 (2009) 13-21.

[37] S. Gamen, A. Anel, P. Perez-Galan, P. Lasierra, D. Johnson, A. Pineiro, J. Naval, Doxorubicin treatment activates a Z-VAD-sensitive caspase, which causes $\Delta\Psi$ loss, caspase-9 activity, and apoptosis in Jurkat cells, Exp. Cell Res. 258 (2000) 223-235.

[38] N.D. Magee, J.R. Beattie, C. Carland, R. Davis, K. McManus, I. Bradbury, D.A. Fennell, P.W. Hamilton, M. Ennis, J.J. McGarvey, J.S. Elborn, Raman microscopy in the diagnosis and prognosis of surgically resected nonsmall cell lung cancer, J. Biomed. Opt. 15 (2010) 026015.

[39] F. Draux, C. Gobinet, J. Sule-Suso, M. Manfait, P. Jeannesson, G.D. Sockalingum, Raman imaging of single living cells: probing effects of non-cytotoxic doses of an anti-cancer drug, Analyst 136 (2011) 2718-2725.

[40] M. Binaschi, G. Capranico, P. De Isabella, M. Mariani, R. Supino, S. Tinelli, F. Zunino, Comparison of DNA cleavage induced by etoposide and doxorubicin in two human small-cell lung cancer lines with different sensitivities to topoisomerase II inhibitors, Int. J. Cancer 45 (1990) 347-352.

[41] X. Liu, C.C. Chua, J. Gao, Z. Chen, C.L. Landy, R. Hamdy, B.H. Chua, Pifithrin-alpha protects against doxorubicin-induced apoptosis and acute cardiotoxicity in mice, Am. J. Physiol. Heart Circ. Physiol. 286 (2004) H933-H939.

[42] C. Ferraro-Peyret, L. Quemeneur, M. Flacher, J.P. Revillard, L. Genestier, Caspase-independent phosphatidylserine exposure during apoptosis of primary T lymphocytes, J. Immunol. 169 (2002) 4805-4810.

[43] Z. Movasaghi, S. Rehman, I.U. Rehman, Raman spectroscopy of biological tissues, Appl. Spectrosc. Rev. 42 (2007) 493-541.

[44] C. Yu, E. Gestl, K. Eckert, D. Allara, J. Irudayaraj, Characterization of human breast epithelial cells by confocal Raman microspectroscopy, Cancer Detect. Prev. 30 (2006) 515-522.

[45] N. Stone, C. Kendall, J. Smith, P. Crow, H. Barr, Raman spectroscopy for identification of epithelial cancers, Faraday Discuss. 126 (2004) 141-157.

[46] N. Stone, C. Kendall, N. Shepherd, P. Crow, H. Barr, Near-infrared Raman spectroscopy for the classification of epithelial pre-cancers and cancers, J. Raman Spectrosc. 33 (2002) 564-573.

[47] W.T. Cheng, M.T. Liu, H.N. Liu, S.Y. Lin, Micro-Raman spectroscopy used to identify and grade human skin pilomatrixoma, Microsc. Res. Techniq. 68 (2005) 75-79.

[48] G. Shetty, C. Kendall, N. Shepherd, N. Stone, H. Barr, Raman spectroscopy: elucidation of biochemical changes in carcinogenesis of oesophagus, Brit. J. Cancer 94 (2006) 1460-1464.

[49] A.J. Ruiz-Chica, M.A. Medina, F. Sanchez-Jimenez, F.J. Ramirez, Characterization by Raman spectroscopy of conformational changes on guanine-cytosine and adenine-thymine oligonucleotides induced by aminooxy analogues of spermidine, J. Raman Spectrosc. 35 (2004) 93-100.

[50] J.W. Chan, D.S. Taylor, T. Zwerdling, S.M. Lane, K. Ihara, T. Huser, Micro-Raman spectroscopy detects individual neoplastic and normal hematopoietic cells, Biophys. J. 90 (2006) 648-656.

[51] L. Chiriboga, P. Xie, H. Yee, V. Vigorita, D. Zarou, D. Zakim, M. Diem, Infrared spectroscopy of human tissue. I. differentiation and maturation of epithelial cells in the human cervix, Biospectroscopy 4 (1998) 47-53.

Table 2.1 Tentative Raman band assignments of Small Airway Epithelial Cells (SAEC) and human lung adenocarcinoma epithelial cell (A549).

Raman shift (cm^{-1})		
SAEC	**A549**	**Band assignment**
624	624	Phenylalanine
643	643	C-C twist Phenylalanine
662	662	C-S stretching mode of cystine (collagen type I)
666	666	G, T-tyrosine-G backbone in RNA
672	669	C-S stretching mode of cytosine
719	719	C-C-N+ symmetric stretching in phosphatidylcholine
720	720	DNA
762	762	Tryptophan
786	785	DNA & phosphdiester bands DNA
813	813	Phosphodiester bands RNA
832	832	PO_2^- stretch nucleic acids
854	853	Tyrosine
880	881	Tryptophan
900	901	Monosaccharides (b-glucose), (C-O-C) skeletal mode

939	939	Skeletal modes (polysaccharides)
961	961	Phosphate of HA; Calcium-phosphate stretch band
1006	1006	Phenylalanine
1034	1034	Phenylalanine
1066	1066	PO_2^- stretching; chain stretching; C-O, C-C stretching
1070-90	1070-90	Symmetric PO_2^- stretching of DNA (represents more DNA in cell)
1095	1095	Phosphodioxy group (PO_2^- in nucleic acids); Lipid
1129	1129	C-C skeletal stretch transconformation
1158	1158	Lipids and nucleic acids (C, G and A)
1179	1176	Cytosine, guanine
1213	1213	Tyrosine, phenylalanine
1254	1254	Lipid; A,T breathing mode (DNA/RNA); Amide III (protein)
1304	1304	CH_2 deformation (lipid), adenine, cytosine
1306	1306	C-N stretching aromatic amines
1317-9	1317-9	Guanine (B,Z-marker)
1343	1342	G (DNA/RNA); CH deformation (proteins and carbohydrates)

1400-30	1400-30	γ(C=O) O^- (amino acids aspartic & glutamic acid)
1451	1450	CH_2 deformation (nucleic acid, proteins, lipids)
1579	1581	Pyrimidine ring (nucleic acids)
1608	1608	Phenylalanine, Tryptophan
1660	1661	Amide I
1740	1740	Collagen III

Band assignment is based on [43-51].

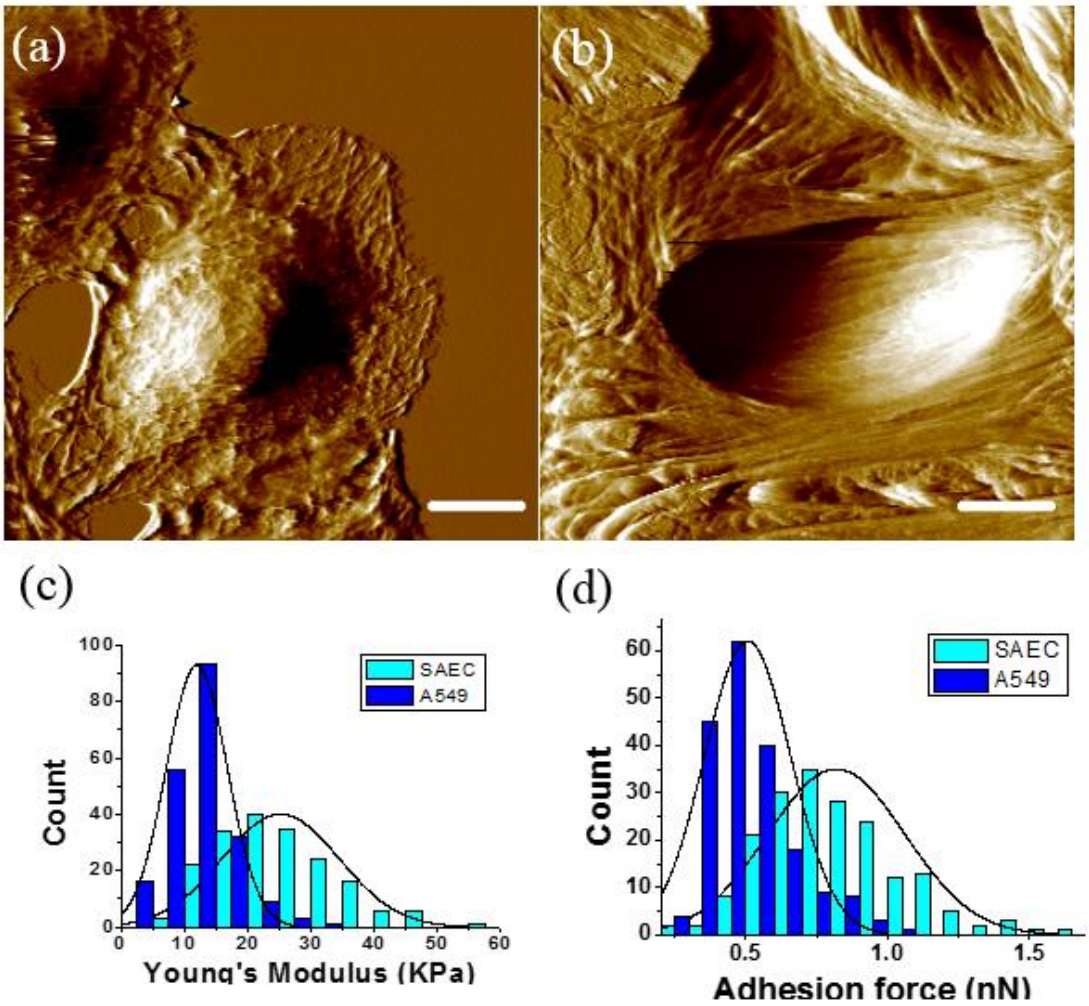


Figure 2.1 AFM images of living (a) A549 and (b) SAEC cells. Cells are imaged in culture media under physiological condition. Scale bar: 10 μm. Histograms of (c) Young's modulus and (d) adhesion force distributions of A549 cells and SAECs.Data are expressed as mean±SD.

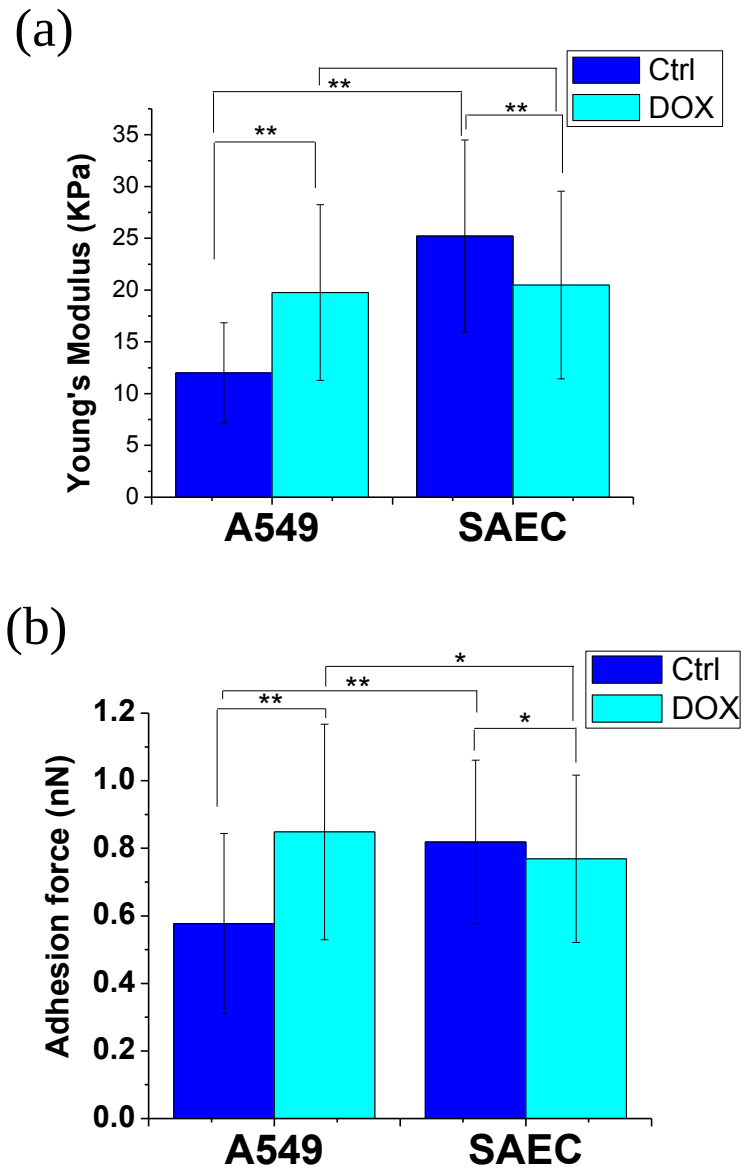


Figure 2.2 Comparison of (a) Young's modulus and (b) adhesion force of A549 cells and SAECs control groups and DOX (70nM, 4hr) treated groups.Values represent mean ± SD (bar) of multiple cells. *p<0.05, **p<0.01.

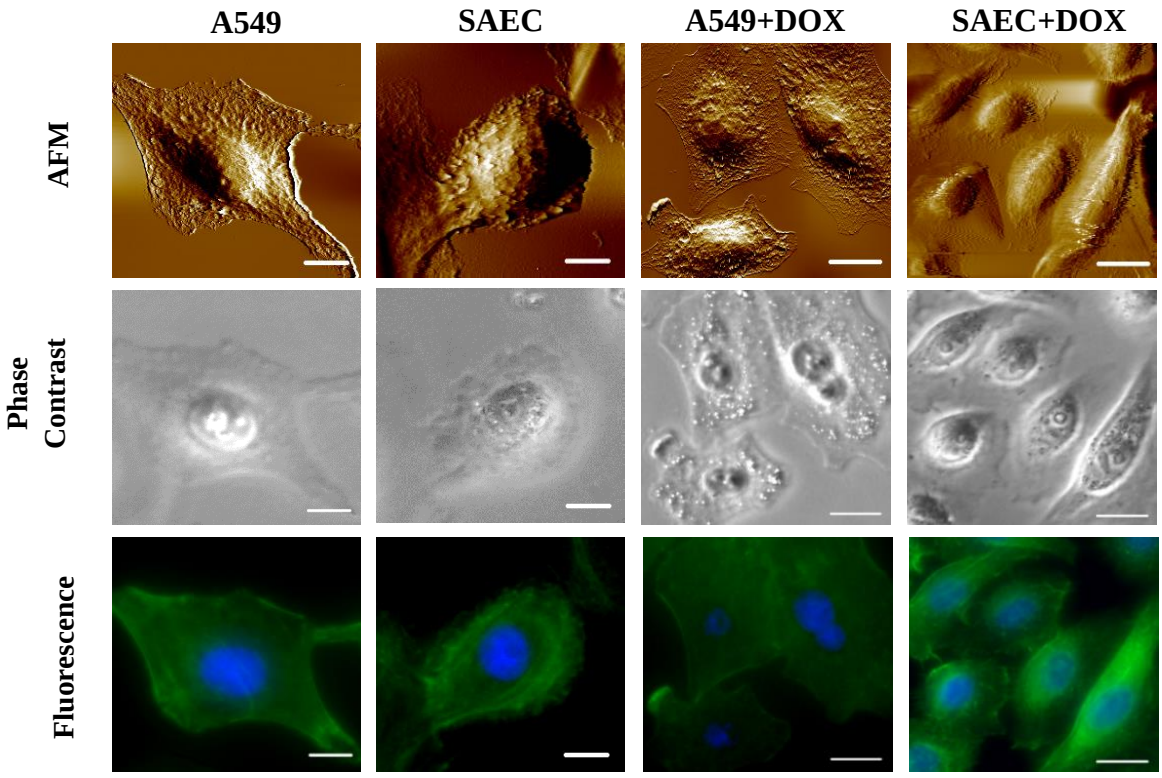


Figure 2.3 AFM deflection (row 1), phase contrast (row 2) and fluorescence (row 3) corresponding images of SAEC and A549 control and DOX treatment (70nM, 4hr), obtained simultaneously using coupled AFM/FL microscope.Cells were fixed with 4% paraformaldehyde. In fluorescence images, F-actin was stained with phalloidin and nucleus was stained with DAPI. Scale bar: 10 µm, column 1 and column 2; 16 µm, column 3 and column 4.

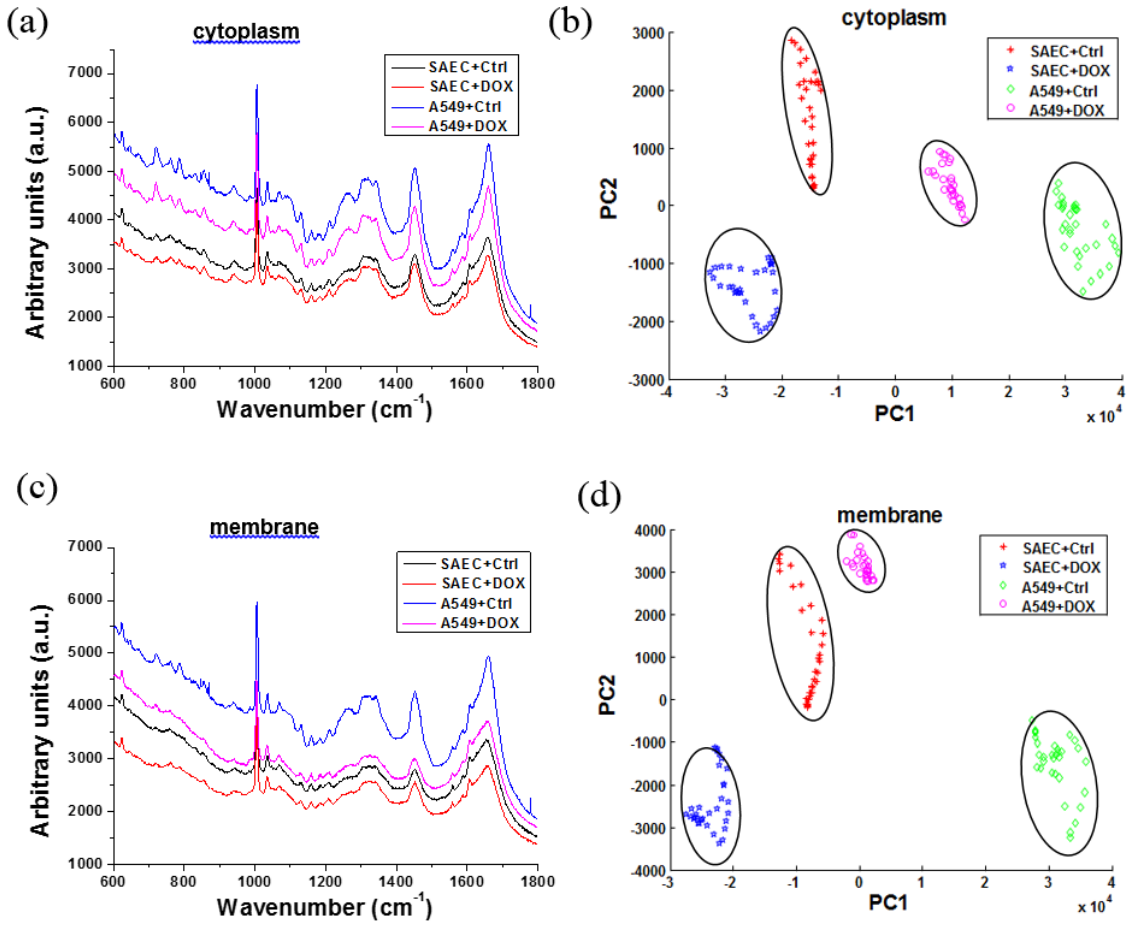


Figure 2.4 Average Raman spectra and PCA analysis of A549 cells and SAECs for cytoplasm (a, b) and membrane (c, d) areas of control and DOX treatment (70nM, 4hr) experiment.

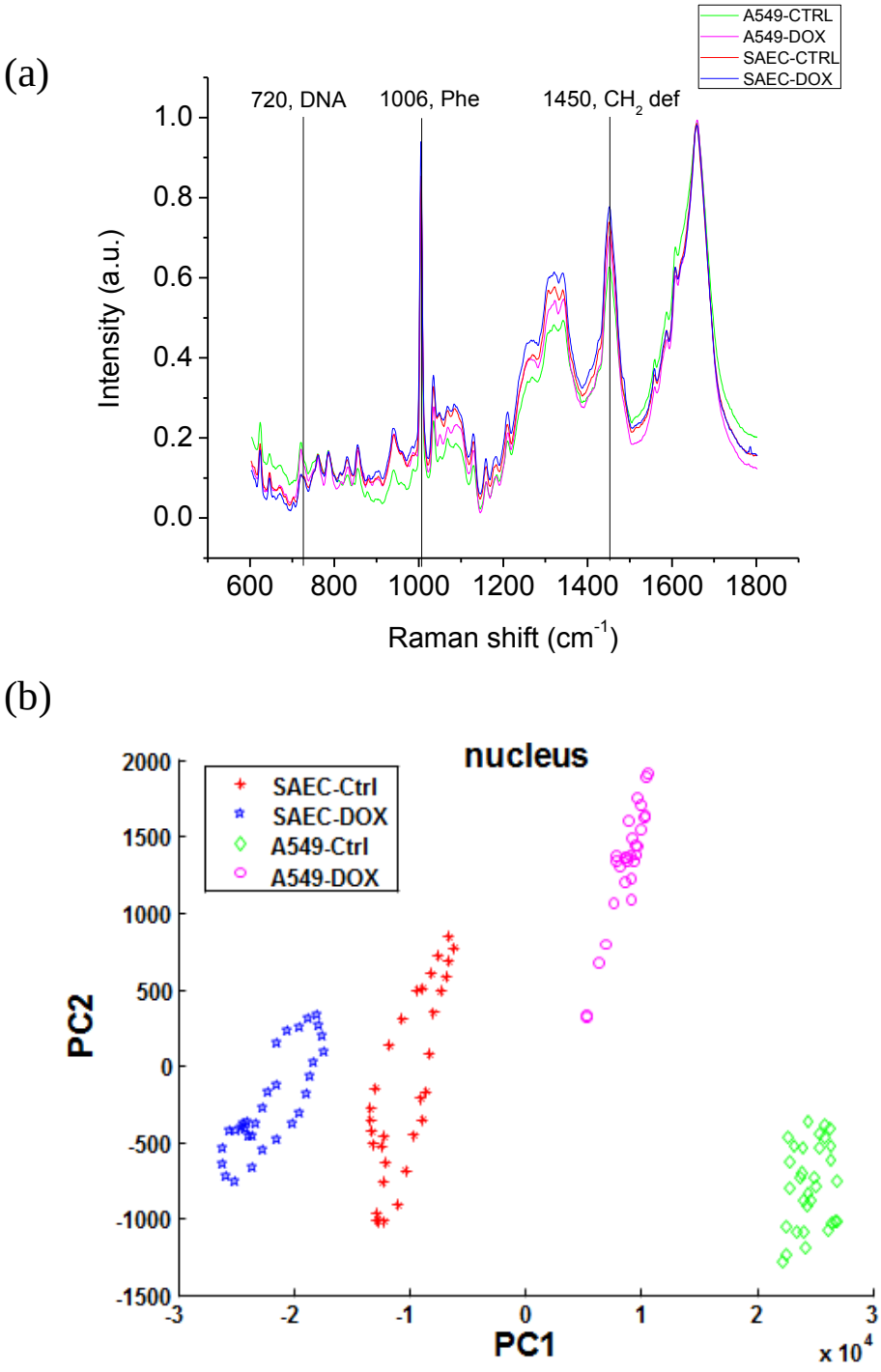


Figure 2. 5 (a) Average Raman spectra and (b) PCA analysis of A549 cells and SAECs for nucleus area of control and DOX treatment (70nM, 4hr) groups (n=32).

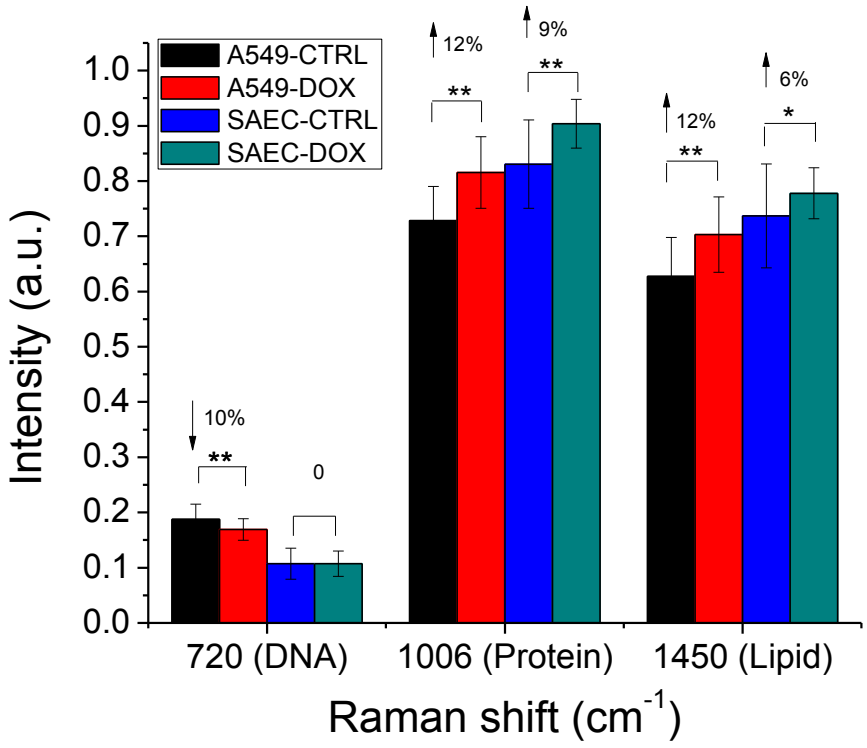


Figure 2.6 Raman intensity of the 720 cm^{-1}, 1006 cm^{-1} and 1450cm^{-1} bands of A549 cells and SAECs under control and DOX treatment condition. 720 cm^{-1}: DNA. 1006 cm^{-1}: Phenylalanine (protein), 1450 cm^{-1}: CH_2 deformation of lipids. Scale bar represents standard deviation. Percentage numbers on column show the changes of peak intensity after DOX exposure. *$p<0.05$, **$p<0.01$.

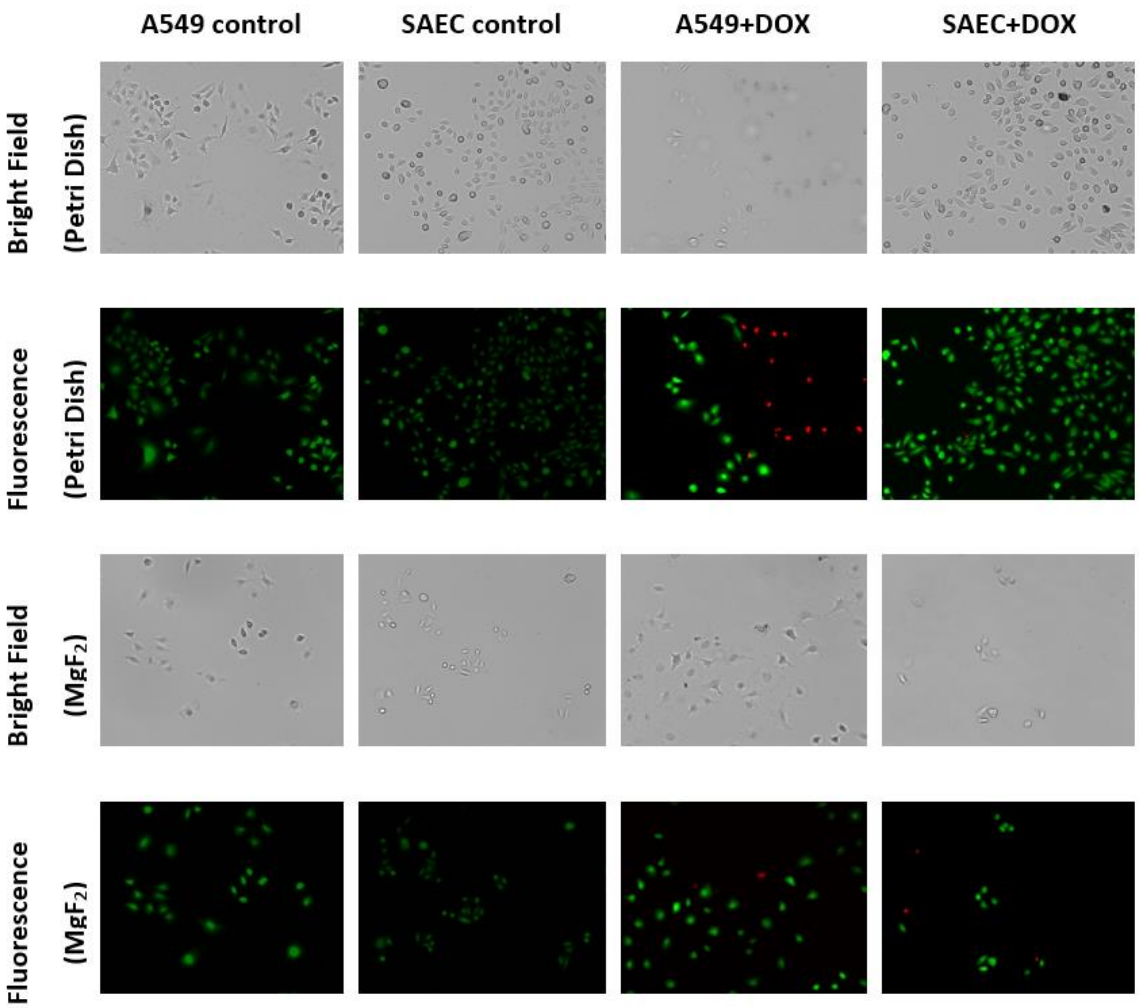


Figure 2.7 Representative fluorescence images of cell viability test. Images of A549 cells and SAEC control (column 1, 2) and with DOX treatment (column 3, 4) were exhibited. Cells were stained with Invitrogen LIVE/DEAD Viability/ Cytotoxicity Assay Kit. Green fluorescence presented live cells, whereas red fluorescence showed dead or membrane-damaged cells. All images were obtained with 10× lens. These fluorescence images together revealed that A549 cells and SAECs which were used for AFM (row 1, 2) and Raman (row 3, 4) experiments were mostly alive.

CHAPTER 3

IMAGING OF EPIDERMAL GROWTH FACTOR RECEPTOR ON SINGLE BREAST CANCER CELLS USING SURFACE-ENHANCED RAMAN SPECTROSCOPY[2]

3.1 ABSTRACT

Epidermal growth factor receptor (EGFR) is widely used as a biomarker for pathological grading and therapeutic targeting of human cancers. This study investigates expression, spatial distribution as well as the endocytosis of EGFR in single breast cancer cells using surface-enhanced Raman spectroscopy (SERS). By incubating anti-EGFR antibody conjugated SERS nanoprobes with an EGFR-over-expressing cancer cell line, A431, EGFR localization was measured over time and found to be located primarily at the cell surface. To further validate the constructed SERS probes, we applied this SERS probes to detect the EGFR expression on breast cancer cells (MDA-MB-435, MDA-MB-231) and their counterpart cell lines in which EGFR expression was down-regulated by breast cancer metastasis suppressor 1 (BRMS1). The results showed that SERS method not only confirms immunoblotting data measuring EGFR levels, but also adds new insights regarding EGFR localization and internalization in living cells which is impossible in immunoblotting method. Thus, SERS provides a powerful new tool to measure biomarkers in living cancer cells.

3.2 INTRODUCTION

Epidermal growth factor receptor (EGFR), a receptor tyrosine kinase, is overexpressed in a variety of human cancers, including all breast cancer subtypes [1]. Overexpression of EGFR in breast cancer is generally associated with poor prognosis and

[2] L. Xiao, S. Harihar, D.R. Welch, A. Zhou, Imaging of epidermal growth factor receptor on single breast cancer cells using surface-enhanced Raman spectroscopy, Anal. Chim. Acta 843 (2014) 73-82

high recurrence rates [2]. Since EGFR status is related to cancer progression, there has been extensive research to develop agents targeting EGFR and its corresponding signaling pathways [3-5]. Therefore, improved methods to quantify and measure function of EGFR in breast cancer cells could improve diagnosis and treatment of breast cancer.

Currently, the most commonly used methods to assess EGFR status in clinical cancer specimens are immunohistochemistry and immunofluorescence staining [6-8]. Quantification can be done using immunoblotting. However, these methods either need cell fixation (immunohistochemistry and immunoblotting), or face the problem of photo-bleaching (immunofluorescence), rendering them non-suitable for measuring dynamic alterations of cell receptors and ligands.

Surface-enhanced Raman spectroscopy (SERS) is a powerful analytical tool in biological applications which has attracted considerable attention recently. SERS offers extremely high enhancement and turns the weak inelastic scattering effect of photons into a structurally sensitive nanoscale probe [9]. In turn, one can realize ultrasensitive levels of detection and non-invasive tagging of specific bioanalytes in living cells and animals [10]. A key to the SERS technique is the metal nanoparticle (NP, e.g. AuNP or AgNP) encoded with sensitive Raman reporter molecules followed by the coating of mono- or multi-layer protective polymers (e.g. silica, polyelectrolyte and PEG) which improve stability and biocompatibility [11-14]. Several studies have reported using SERS probes to target cancer cells in vitro or in vivo [11, 14-19], including measurement of EGFR [11, 15, 19]. However, very little SERS studies were focused on EGFR cellular distribution, EGFR-mediated bioprocess, and how EGFR is regulated by metastasis suppressors.

Metastasis suppressors are a relatively recently described family of molecules that suppress the development of cancer metastasis without blocking primary tumor growth (reviewed in [20]). Of the approximately 30 metastasis suppressors (genes) identified to date, BRMS1 has been well characterized for its ability to regulate molecules that alter cellular response to micro-environmental signals which can be different between orthotopic sites (i.e., the mammary gland for breast cancer) and ectopic sites (i.e., sites of metastasis) [21], thought to explain why metastasis suppressors allow primary tumor growth, but not metastatic colonization. BRMS1 regulates EGFR [21] and osteopontin [22] expression, phosphoinositide [23], NFκB [24] and PKA [25] signaling, connexin expression and gap junctional intercellular communication [20, 26], all of which play significant roles in cancer progression. The mechanism by which BRMS1 does these myriad things is thought to be as part of SIN3 histone deacetylase regulation of chromatin structure [27].

Understanding how BRMS1 directly impacts cellular responses to signals from the microenvironment is thought to be key to defining the critical mechanisms of action. Unfortunately, the tools to measure ligand-receptor or antibody-antigen interactions are suboptimal for this purpose. Therefore, we designed a SERS probe based on polyelectrolyte-coated gold nanorods (AuNRs) to specifically recognize and detect EGFR molecules (via antibody-antigen interaction) on the cell surface of breast cancer cells. Using an EGFR over-expressing cell line (e.g., A341), we validated the ability of the antibody-conjugated SERS probe to measure EGFR distribution and internalization on single cancer cells. Then, using BRMS1-expressing cells and comparing them to their parental breast cancer counterparts, we demonstrated that our constructed SERS probe is

able to distinguish EGFR levels in different cancer cells and provide spatial information of EGFR expressed on single cancer cell surface.

3.3 MATERIALS AND METHODS

3.3.1 Materials

Ultrapure water (18 MΩ cm^{-1}) was used in this work. All chemicals were purchased from commercial source and were used as received: gold nanorods (5.1×10^{11} particles mL^{-1}, Nanopartz Inc., USA), monoclonal anti-EGFR antibody (Invitrogen). A431 cell line was obtained from American Type Culture Collection (ATCC). MDA-MB-435 (435), MDA-MB-231 (231), MDA-MB-435 expressing BRMS1 (435^{BRMS1}) and MDA-MB-231 expressing BRMS1 (231^{BRMS1}) were described previously [21]. Cell culture media and supplies were purchased from Thermo Fisher Scientific Inc. (Waltham, MA). Other chemicals were purchased from Sigma-Aldrich (St. Louis, MO) at the highest available purity.

3.3.2 Instrumentation

The morphology of the gold nanorods (AuNRs) SERS probe was determined by a FEI Titan 80-300 transmission electron microscope (TEM) in a bright-field mode. Extinction spectra of the AuNRs were taken by an Agilent Cary 60 UV-Vis Spectrophotometer controlled by Cary WinUV software. Dark field images of cell samples were obtained by using an Olympus IX71 Inverted Microscope equipped with an oil-immersed dark field condenser (NA=1.5) and a 100× objective lens. Images were acquired using DPController software (Olympus).

3.3.3 Preparation of SERS probe

As shown in Figure 3.1a, the synthesis of the SERS probe includes three steps: (1) bare AuNRs and Raman reporter molecules 4-mercaptobenzoic acid (MBA) were mixed together with a molar ratio of 1:10000, conjugating the reporter molecules onto AuNRs through Au-S interaction; (2) polyallylamine hydrochloride (PAH) solution (28 mg mL^{-1}, 200 µL) and NaCl solution (1 mM, 100 µL) were added to 1 mL of AuNRs solution containing 1 nM MBA-AuNRs and reacted for 3 hr; and (3) after removing the excess PAH by centrifugation, monoclonal antibody anti-EGFR (0.21 mg mL^{-1}, 10 µL) was added to the solution and incubated for 1 hr. Excess antibody was removed by centrifugation. The SERS probe was stable for several days at 4°C in solution.

3.3.4 Cell culture

Cell lines were grown in a mixture of Dulbecco's-modified Eagle's medium (DMEM) and Ham's F-12 medium (1:1) supplemented with 5% fetal bovine serum (Atlanta Biologicals, Atlanta, GA) in a humidified atmosphere at 37°C with 5% CO_2. Cells were at 80~90% confluence when used for experiments.

3.3.5 Immunoblotting

Cells were rinsed twice with ice-cold PBS and lysed in a buffer containing 25 mM Tris-HCl (pH 7.4), ß-glycerol phosphate (50 mM), EDTA (0.5 mM), glycerol (5%), triton X-100 (0.1%), sodium orthovanadate (1 mM), benzamidine (1 mM), and a protease inhibitor cocktail containing aprotinin, leupeptin, and phenylmethylsulfonyl fluoride (Roche, Indianapolis, IN). Protein concentration was determined using a BCA assay (Pierce, Rockford, IL). Protein was denatured with Laemmli's buffer at 95°C for 5 min and lysate (50 µg) was loaded to each well. Proteins were separated using 10% SDS-PAGE gel

electrophoresis and resolved proteins were transferred to PVDF before incubating in Tris-buffered saline containing Tween-20 (0.05%) and fat-free dry milk (5%) for 1 hr at room temperature. Membranes were incubated with primary antibodies to EGFR (Cell Signaling, Danvers, MA) β-Actin (Sigma, St. Louis, MO) and BRMS1 overnight at 4°C and subsequently with HRP-conjugated secondary antibody at room temperature for 1 hr. Signals were visualized using ECL (Pierce, Rockford, IL) following manufacturer's instructions.

3.3.6 Immunofluorescence imaging

To evaluate EGFR localization, MDA-MB-435/231 and $435^{BRMS1}/231^{BRMS1}$ cells grown on coverslips for 24 hr were fixed using 4% para-formaldehyde (Electron Microscopy Sciences, Hatfield, PA) for 20 min, and permeabilized using 0.1% Triton X-100 (Union Carbide Corporation, Texas City, TX) for 10 min. After blocking with 5% BSA in PBS, cells were incubated with anti-EGFR antibody conjugated with Alexia Fluor 555 at 1:50 dilution (Life technologies, Carlsbad, CA) in 5% BSA solution overnight at 4°C. After washing the cells thrice with PBS, the cover slips were mounted using Vectashield mounting solution containing the nuclear counter-stain 4′, 6-diamidino-2-phenylindole (Vector laboratories Inc, Burlingame, CA). Images were collected under a Nikon inverted epifluorescence microscope. Representative images were combined, and processed using ImageJ software.

3.3.7 SERS measurement on living cancer cells

Cells were used at a density of 0.5×10^5 cells per milliliter. Media (2 mL) containing cells were placed on a cleaned magnesium fluoride (MgF_2) optical window (United Crystals Co., Port Washington, NY) in order to minimize background in Raman

measurement. Cells cultured on MgF_2 were incubated with the antibody conjugated SERS probes for different time (1.5, 3, 4.5 and 6 hr) and washed with PBS to remove non-adsorbed probes prior to Raman measurements.

Raman spectra were measured by a Renishaw inVia Raman system (controlled by WiRE 3.3 software, Renishaw, UK) connected to a Leica microscope (Leica DMLM, Leica microsystems, USA) equipped with a 785 nm near-IR laser that was focused through a 63× water immersion objective (NA=0.90, Leica Microsystems). The instrument was calibrated with silicon (Raman peak centered at 520.5 cm^{-1}). Raman spectra (600 and 1800 cm^{-1}) were recorded using 1 accumulation per 10 sec laser exposure (1% laser intensity (3 mW) static mode). For Raman line and depth profiling, multiple spectra were acquired at different locations with constant intervals (line: 3 μm; depth: 1.5 μm). Spectral smoothing, baseline subtraction and Raman mapping generation were performed using Renishaw WiRE 3.3 software. The processed spectra were exported to Origin Pro 8.5 software (OriginLab Corp., USA) for statistical analysis.

3.3.8 Cell viability test

The cell viability was analyzed using LIVE/DEAD Viability/Cytotoxicity Assay Kit (Invitrogen) according to the manufacturer's instruction. Briefly, (1) cells were cultured in poly-D-lysine coated glass-bottom dishes (MatTek Cop. USA) and MgF_2 substrate which was put in Petri dishes for 24 hr; (2) cells were then washed with PBS twice; (3) 2 ml of mixed solution of 2 μM Calcein AM and 4 μM ethidium homodimer-1 (EthD-1) (both from Invitrogen) was added directly to cells, and incubated cells for 30 min at room temperature; (5) cells were imaged using fluorescence microscope with DP30BW CCD camera (Olympus IX71) to analyze the relative proportion of live/dead cells. Here, a 10×

objective was used to observe fluorescence. Calcein AM is well retained within live cells producing green fluorescence; however, EthD-1 enters cells with damaged membrane and binds to nucleic acids, thereby producing a red fluorescence in dead or membrane-damaged cells. Therefore, the live/dead cells were differentiated visually.

3.4 RESULTS AND DISCUSSION

3.4.1 Characterization of the SERS probe

Figure 3.1a illustrates preparation of the MBA-encoded, PAH-coated, and anti-EGFR functionalized AuNRs as the SERS probes. The size and morphology of the SERS probes were visualized by TEM (Figure 3.1b). The successful coating of PAH and antibody was confirmed by a thin dim film on the surface of AuNRs and the slight red-shift of the maximum plasmon peaks (Figure 3.1c). MBA was used as a Raman reporter molecule to optimize SERS sensitivity due to its strong affinity to Au surface and simple SERS spectrum. The PAH molecule, a polyelectrolyte with positive charge, plays an important role by, not only preventing AuNR aggregation, but also providing biocompatibility to the SERS probes (Figure 3.2). Compared with other polymer coatings, such as thiol-PEG and silica, polyelectrolyte coating simplified the process, and more importantly, avoided adsorption competition with Raman reporters [14, 28]. Taken together, these conditions were expected to provide higher SERS sensitivity.

Figure 3.1c shows the stepwise extinction spectra of the AuNR during the preparation process. The longitudinal plasmon resonance band for bare AuNR is located at *ca*. 770 nm, which is related to the 3.7 aspect ratio of the nanorods (Figure 3.1b). The nanorod longitudinal plasmon band (770 nm) is favorable in this work because it overlaps, in part, with the excitation laser source (785 nm), providing >10× surface enhancement

than substrates whose Plasmon bands do not overlap with the excitation source [29]. After coating with MBA, PAH and antibody, the longitudinal plasmon band maxima red-shifted 5 nm, which is thought to be due to changes in local refractive index. Red shifts were also reported previously [14, 30, 31]. A typical SERS spectrum of the MBA-linked SERS probe is shown in Figure 3.1d. The two highest Raman peaks (1077 and 1588 cm^{-1}) were observed and could be assigned to the ring breathing and axial deformation modes of MBA, respectively [32, 33]. Since the peak at 1077 cm^{-1} was the most stable and reproducible characteristic band for the reporter, MBA, it was used for further Raman analysis in this study.

3.4.2 Detection of EGFR on single A431 cells

SERS has been widely applied since 1970s when it's reported that molecular adsorption onto a roughened noble metal surface led to electromagnetic and chemical enhancement mechanisms [34, 35]. Using a molecule with an intense and distinguishable Raman signature as a reporter molecule for sensing and quantification is called extrinsic SERS (reviewed in [36]). In the presented work, the extrinsic SERS strategy is used—we are trying to detect cell surface receptor EGFR using anti-EGFR antibody targeted SERS nanoprobes, conjugated with MBA as reporter molecule, and track the EGFR localization by measuring the specific Raman signature of MBA.

In order to investigate whether the anti-EGFR functionalized SERS probe can successfully detect the expression of EGFR on cells, A431, which highly expresses EGFR [37-39], was used (Figure 3.3). The SERS probe were incubated with A431 cells under three different conditions: (1) cells were incubated with SERS probes without anti-EGFR antibody conjugation for 1.5 hr at 37°C ("No Antibody", representing non-specific

interaction); (2) cells were incubated with anti-EGFR antibody-conjugated SERS probes for 1.5 hr at 37°C ("Antibody"); (3) cells were pre-blocked with free anti-EGFR antibody for 1 hr before incubation with the antibody-conjugated SERS probe for 1.5 hr ("Antibody_Block"). Typical SERS spectra for the three groups are shown in Figure 3.3a. "Antibody group" shows two major intense peaks at 1077 cm^{-1} and 1588 cm^{-1}, while the peak intensities are very low in "No Antibody" group and "Antibody_Block" group. The Raman intensities at 1077 cm^{-1} for "Antibody" group was significantly higher ($P<0.001$, $n=60$) than the other two treatment groups (Figure 3.3b), demonstrating the specificity of the antibody-antigen interaction. SERS mapping images revealed intense signals in "Antibody" group but significantly less in the other two conditions (Figure 3.3c). Thus, the findings confirm that SERS specifically recognizes EGFR on A431 cells by antibody-antigen interactions.

3.4.3 Local distribution and depth profiling of EGFR on single A431 cells

The spatial distribution of EGFR on single A431 cell surface was also studied. Figure 3.4 shows the Raman line profiling spectra when the laser spot was scanning over different locations on a single A431 cell. Eleven separated locations across the cell were measured along a straight line (Figure 3.4a). Only at central locations (# 4~7) were there distinguishable SERS bands (Figure 3.4b). Figure 3.4c shows normalized SERS intensity at 1077 cm^{-1} at all 11 points on the cell surface. This Raman line profiling shows that EGFR markers were not homogeneously distributed on the cell surface, and seem mainly located on the central region of the cell surface of this selected cell. This kind of EGFR distribution had also been reported in some other studies, especially when EGF had been introduced [40, 41].

To study antibody-functionalized gold nanoparticles are internalized via receptor-mediated endocytosis [42, 43], a confocal Raman setting was applied to detect the SERS spectra collected at depth levels ranging from 0 (top, upper cell surface), 3 μm (middle, middle surface of the cell), to 6 μm (bottom, lower surface of the cell) (Figure 3.5). At 3-hr incubation of the SERS probes with A431 cells, Raman streamline mapping (at 1077 cm^{-1}) of the same cells at three different depths (0, 3, and 6 μm) were captured sequentially (Figure 3.5a). Red areas in the mapping images represent the presence of the EGFR molecules in single A431 cells. Raman spectra at an EGFR aggregate at different depths (points 1-3, Figure 3.5a) are shown in Figure 3.5b. It shows the highest peak intensity at the apical surface and lowest at the basal cell membrane, indicating that majority of the AuNRs has still yet to be internalized at 3-hr incubation. To further study the EGFR-mediated endocytosis of nanoparticle, we measured the Raman peak intensities at EGFR aggregates at top, middle and bottom of the cells with 1.5 hr, 3 hr, 4.5 hr and 6 hr incubation of SERS probes. As shown in Figure 3.5c, at 1-3 hr incubation, the highest peak intensities are at the top surface of the cells, indicating that the internalization level is low; while at 4-6 hr incubation, the highest intensities are at the middle, which means most of the AuNRs are internalized into the cells. As reported, the process of EGFR mediated endocytosis is strongly influenced by the applied targeting ligands [44]. Here we used monoclonal antibody as the targeting ligand, which is much slower than the EGF targeted EGFR endocytosis [34]. This is because EGF can activate the receptor signaling, whereas the antibody binding is unable to lead to considerable downstream receptor activation. Fluorescence live/dead imaging test was conducted to prove that cells remained high viability (>95 %) after incubation with SERS probes for 1.5, 3, 4.5 and 6 hr (Figure 3.2).

3.4.4 BRMS1-regulated EGFR expression on MDA-MB-435 and MDA-MB-231 breast cancer cells

EGFR was significantly down-regulated in BRMS1-expressing human breast cancer cell lines as previously reported [21]. In this report, the immunoblotting results showed that reduction of EGFR in 231^{BRMS1} cells was not as dramatic as previously reported. Nonetheless, the complete loss of EGFR in 435^{BRMS1} cells was readily apparent by immunoblotting (Figure 3.6a). Using SERS probe to measure EGFR (Figure 3.6b), 435^{BRMS1} cells have significantly ($P<0.001$, $n=60$) lower levels than parental 435 cells. The results are not significantly different when comparing 231 and 231^{BRMS1} cells ($P>0.05$, $n=60$). The SERS results are essentially consistent with traditional western blot data (Figure 3.6a). However, SERS mapping provides the spatial distribution of EGFR at the single cell level that western blot does not have.

Dark-field microscopic imaging was also done (Figure 3.6c-f) since AuNR scatter light intensely and they are much brighter than cells in the dark field [45, 46]. The presence of many bright spots on 435 cells (Figure3.6c) reflects abundant EGFR expressed, while the abundance of spots is negligible on 435^{BRSM1} cells (Figure 3.6d). The numbers of bright spots in 231 cells are not readily distinguishable than those observed in 231^{BRMS1} cells, consistent with the western blot results. Based on the dark field images and SERS spectra in living cells, the constructed SERS probes can be utilized as multimodal cell imaging sensors.

Recognition of EGFR molecules and analysis of their distribution on single cells was done by SERS mapping at 1077 cm^{-1} comparing 231 and 435 cells with their BRMS1-expressing counterparts (Figure 3.7). Bright field images (upper panel) and their

corresponding SERS maps (lower panel) were simultaneously recorded. EGFR was heterogeneously distributed on the plasma membrane. To further validate the observations from SERS method, 435, 231, 435^{BRMS1} and 231^{BRMS1} cells were labeled with anti-EGFR antibody conjugated to Alexia Fluor 555 to measure EGFR localization using immunofluorescence (IF) imaging. As presented in Figure 3.8, the IF images confirmed the down-regulation of EGFR expression by BRMS1 gene in MDA-MB-435 and MDA-MB-231 cells as our SERS results suggested. The consistency between SERS and IF results indicates SERS is a tool as powerful as IF to detect cellular receptors as single-cell level. Moreover, SERS possesses potential advantages over fluorescence in multiplex imaging of cell receptors due to much narrower spectroscopic bands of Raman spectra.

3.5 CONCLUSIONS

We developed a AuNR-based SERS probe that allows live-cell targeting and imaging of EGFR, a widely recognized breast cancer marker. The probe successfully detected EGFR and distinguished heterogeneity in its distribution on the plasma membrane of cells growing in culture. Furthermore, using Raman depth mapping, internalization of the SERS probes could be monitored temporally and spatially. Data using the SERS probes are consistent with standard detection methods, but affords the capability to measure dynamic changes molecules in living cells. Thus, our SERS probes can be used as a noninvasive sensing agent for detection of spatial distribution and dynamic change of EGFR on living breast cancer cells at the single cell level, which is a significantly complement to the traditional biochemical approaches like immunoblotting and immunofluorescence. This work also demonstrated the potential of using SERS to investigate EGFR-involved physiological process such as EGFR-mediated nanoparticle

uptake and EGF-EGFR interaction. Our future work is to study multiple cell surface receptors and their interactions by using different Raman reporter labeling; besides, using tip-enhanced Raman Spectroscopy (TERS) would be alternative option allowing us to achieve single-molecular detection of cell receptors at nanoscale cell surface.

3.6 REFERENCES

[1] H. Masuda, D.W. Zhang, C. Bartholomeusz, H. Doihara, G.N. Hortobagyi, N.T. Ueno, Role of epidermal growth factor receptor in breast cancer, Breast Cancer. Res. Tr. 136 (2012) 331-345.

[2] J.R.C. Sainsbury, J.R. Farndon, G.K. Needham, A.J. Malcolm, A.L. Harris, Epidermal-growth factor receptor status as predictor of early recurrence of and death from breast cancer, Lancet 1 (1987) 1398-1402.

[3] V. Grunwald, M. Hidalgo, Developing inhibitors of the epidermal growth factor receptor for cancer treatment, J. Natl. Cancer I. 95 (2003) 851-867.

[4] G. Chen, P. Kronenberger, E. Teugels, I.A. Umelo, J. De Greve, Targeting the epidermal growth factor receptor in non-small cell lung cancer cells: the effect of combining RNA interference with tyrosine kinase inhibitors or cetuximab, BMC Med. 10 (2012) 28.

[5] S. Siena, A. Sartore-Bianchi, F. Di Nicolantonio, J. Balfour, A. Bardelli, Biomarkers predicting clinical outcome of epidermal growth factor receptor-targeted therapy in metastatic colorectal cancer, J. Natl. Cancer I. 101 (2009) 1308-1324.

[6] S. Muller, L. Su, M. Tighiouart, N. Saba, H.Z. Zhang, D.M. Shin, Z. Chen, Distinctive E-cadherin and epidermal growth factor receptor expression in metastatic and

nonmetastatic head and neck squamous cell carcinoma—predictive and prognostic correlation, Cancer-Am. Cancer Soc. 113 (2008) 97-107.

[7] A. Psyrri, M. Kassar, Z.W. Yu, A. Bamias, P.M. Weinberger, S. Markakis, D. Kowalski, R.L. Camp, D.L. Rimm, M.A. Dimopoulos, Effect of epidermal growth factor receptor expression level on survival in patients with epithelial ovarian cancer, Clin. Cancer Res. 11 (2005) 8637-8643.

[8] X.Q. Yang, C. Chen, C.W. Peng, J.X. Hou, S.P. Liu, C.B. Qi, Y.P. Gong, X.B. Zhu, D.W. Pang, Y. Li, Quantum dot-based quantitative immunofluorescence detection and spectrum analysis of epidermal growth factor receptor in breast cancer tissue arrays, Int. J. Nanomed. 6 (2011) 2265-2273.

[9] J. Kneipp, H. Kneipp, K. Kneipp, SERS—a single-molecule and nanoscale tool for bioanalytics, Chem. Soc. Rev. 37 (2008) 1052-1060.

[10] R.A. Alvarez-Puebla, L.M. Liz-Marzan, SERS-based diagnosis and biodetection, Small 6 (2010) 604-610.

[11] K.K. Maiti, U.S. Dinish, C.Y. Fu, J.J. Lee, K.S. Soh, S.W. Yun, R. Bhuvaneswari, M. Olivo, Y.T. Chang, Development of biocompatible SERS nanotag with increased stability by chemisorption of reporter molecule for in vivo cancer detection, Biosens. Bioelectron. 26 (2010) 398-403.

[12] G. von Maltzahn, A. Centrone, J.H. Park, R. Ramanathan, M.J. Sailor, T.A. Hatton, S.N. Bhatia, SERS-coded gold nanorods as a multifunctional platform for densely multiplexed near-infrared imaging and photothermal heating, Adv. Mater. 21 (2009) 3175-3180.

[13] C.L. Zavaleta, B.R. Smith, I. Walton, W. Doering, G. Davis, B. Shojaei, M.J. Natan, S.S. Gambhir, Multiplexed imaging of surface enhanced Raman scattering nanotags in living mice using noninvasive Raman spectroscopy, Proc. Natl. Acad. Sci. USA 106 (2009) 13511-13516.

[14] L. Jiang, J. Qian, F.H. Cai, S.L. He, Raman reporter-coated gold nanorods and their applications in multimodal optical imaging of cancer cells, Anal. Bioanal. Chem. 400 (2011) 2793-2800.

[15] X.M. Qian, X.H. Peng, D.O. Ansari, Q. Yin-Goen, G.Z. Chen, D.M. Shin, L. Yang, A.N. Young, M.D. Wang, S.M. Nie, In vivo tumor targeting and spectroscopic detection with surface-enhanced Raman nanoparticle tags, Nat. Biotechnol. 26 (2008) 83-90.

[16] D.C. Kennedy, D.R. Duguay, L.L. Tay, D.S. Richeson, J.P. Pezacki, SERS detection and boron delivery to cancer cells using carborane labelled nanoparticles, Chem. Commun. (2009) 6750-6752.

[17] P. Wu, Y. Gao, H. Zhang, C.X. Cai, Aptamer-guided silver-gold bimetallic nanostructures with highly active surface-enhanced Raman scattering for specific detection and near-infrared photothermal therapy of human breast cancer cells, Anal. Chem. 84 (2012) 7692-7699.

[18] J. Yang, Z.Y. Wang, S.F. Zong, C.Y. Song, R.H. Zhang, Y.P. Cui, Distinguishing breast cancer cells using surface-enhanced Raman scattering, Anal. Bioanal. Chem. 402 (2012) 1093-1100.

[19] X. Wang, X.M. Qian, J.J. Beitler, Z.G. Chen, F.R. Khuri, M.M. Lewis, H.J.C. Shin, S.M. Nie, D.M. Shin, Detection of circulating tumor cells in human peripheral blood using surface-enhanced Raman scattering nanoparticles, Cancer Res. 71 (2011) 1526-1532.

[20] S.A. Eccles, D.R. Welch, Metastasis: recent discoveries and novel treatment strategies, Lancet 369 (2007) 1742-1757.

[21] K.S. Vaidya, S. Harihar, P.A. Phadke, L.J. Stafford, D.R. Hurst, D.G. Hicks, G. Casey, D.B. DeWald, D.R. Welch, Breast cancer metastasis suppressor-1 differentially modulates growth factor signaling, J. Biol. Chem. 283 (2008) 28354-28360.

[22] R.S. Samant, D.W. Clark, R.A. Fillmore, M. Cicek, B.J. Metge, K.H. Chandramouli, A.F. Chambers, G. Casey, D.R. Welch, L.A. Shevde, Breast cancer metastasis suppressor 1 (BRMS1) inhibits osteopontin transcription by abrogating NF-kappa B activation, Mol. Cancer 6 (2007) 6.

[23] D.B. DeWald, J. Torabinejad, R.S. Samant, D. Johnston, N. Erin, J.C. Shope, Y. Xie, D.R. Welch, Metastasis suppression by breast cancer metastasis suppressor 1 involves reduction of phosphoinositide signaling in MDA-MB-435 breast carcinoma cells, Cancer Res. 65 (2005) 713-717.

[24] M. Cicek, R. Fukuyama, D.R. Welch, N. Sizemore, G. Casey, Breast cancer metastasis suppressor 1 inhibits gene expression by targeting nuclear factor-kappa B activity, Cancer Res. 65 (2005) 3586-3595.

[25] T.M. Bodenstine, K.S. Vaidya, A. Ismail, B.H. Beck, L.M. Cook, A.R. Diers, A. Landar, D.R. Welch, Homotypic gap junctional communication associated with metastasis suppression increases with PKA activity and is unaffected by PI3K inhibition, Cancer Res. 70 (2010) 10002-10011.

[26] M.M. Saunders, M.J. Seraj, Z.Y. Li, Z.Y. Zhou, C.R. Winter, D.R. Welch, H.J. Donahue, Breast cancer metastatic potential correlates with a breakdown in homospecific

and heterospecific gap junctional intercellular communication, Cancer Res 61 (2001) 1765-1767.

[27] D.R. Hurst, D.R. Welch, Unraveling the enigmatic complexities of BRMS1-mediated metastasis suppression, FEBS Lett. 585 (2011) 3185-3190.

[28] X.B. Tan, Z.Y. Wang, J. Yang, C.Y. Song, R.H. Zhang, Y.P. Cui, Polyvinylpyrrolidone- (PVP-) coated silver aggregates for high performance surface-enhanced Raman scattering in living cells, Nanotechnology 20 (2009) 445102.

[29] C.J. Orendorff, L. Gearheart, N.R. Jana, C.J. Murphy, Aspect ratio dependence on surface enhanced Raman scattering using silver and gold nanorod substrates, Phys. Chem. Chem. Phys. 8 (2006) 165-170.

[30] H. Ding, K.T. Yong, I. Roy, H.E. Pudavar, W.C. Law, E.J. Bergey, P.N. Prasad, Gold nanorods coated with multilayer polyelectrolyte as contrast agents for multimodal imaging, J. Phys. Chem. C 111 (2007) 12552-12557.

[31] A. Gole, C.J. Murphy, Polyelectrolyte-coated gold nanorods: Synthesis, characterization and immobilization, Chem. Mater. 17 (2005) 1325-1330.

[32] S.W. Bishnoi, C.J. Rozell, C.S. Levin, M.K. Gheith, B.R. Johnson, D.H. Johnson, N.J. Halas, All-optical nanoscale pH meter, Nano Lett. 6 (2006) 1687-1692.

[33] A. Michota, J. Bukowska, Surface-enhanced Raman scattering (SERS) of 4-mercaptobenzoic acid on silver and gold substrates, J. Raman Spectrosc. 34 (2003) 21-25.

[34] M.G. Albrecht, J.A. Creighton, Anomalously intense Raman-spectra of pyridine at a slver electrode, J. Am. Chem. Soc. 99 (1977) 5215-5217.

[35] D.L. Jeanmaire, R.P. Van Duyne, Surface Raman spectroelectrochemistry: Part I. heterocyclic, aromatic, and aliphatic amines adsorbed on the anodized silver electrode, J. Electroanal. Chem. 84 (1977) 1-20.

[36] K.C. Bantz, A.F. Meyer, N.J. Wittenberg, H. Im, O. Kurtulus, S.H. Lee, N.C. Lindquist, S.H. Oh, C.L. Haynes, Recent progress in SERS biosensing, Phys. Chem. Chem. Phys. 13 (2011) 11551-11567.

[37] Z. Novy, P. Barta, J. Mandikova, M. Laznicek, F. Trejtnar, A comparison of in vitro methods for determining the membrane receptor expression in cell lines, Nucl. Med. Biol. 39 (2012) 893-896.

[38] C. Linassier, M. Pierre, J.B. Lepecq, J. Pierre, Mechanisms of action in NIH-3T3 cells of genistein, an inhibitor of EGF receptor tyrosine kinase activity, Biochem. Pharmacol. 39 (1990) 187-193.

[39] T. Akiyama, J. Ishida, S. Nakagawa, H. Ogawara, S. Watanabe, N. Itoh, M. Shibuya, Y. Fukami, Genistein, a specific inhibitor of tyrosine-specific protein kinases, J. Biol. Chem. 262 (1987) 5592-5595.

[40] J. Merlin, L. Stechly, S. de Beauce, D. Monte, E. Leteurtre, I. van Seuningen, G. Huet, P. Pigny, Galectin-3 regulates MUC1 and EGFR cellular distribution and EGFR downstream pathways in pancreatic cancer cells, Oncogene 30 (2011) 2514-2525.

[41] B.G. Bitler, A. Goverdhan, J.A. Schroeder, MUC1 regulates nuclear localization and function of the epidermal growth factor receptor, J. Cell Sci. 123 (2010) 1716-1723.

[42] A.E. Nel, L. Madler, D. Velegol, T. Xia, E.M.V. Hoek, P. Somasundaran, F. Klaessig, V. Castranova, M. Thompson, Understanding biophysicochemical interactions at the nano-bio interface, Nat. Mater. 8 (2009) 543-557.

[43] I. Lynch, K.A. Dawson, Protein-nanoparticle interactions, Nano Today 3 (2008) 40-47.

[44] F.M. Mickler, L. Mockl, N. Ruthardt, M. Ogris, E. Wagner, C. Brauchle, Tuning nanoparticle uptake: live-cell imaging reveals two distinct endocytosis mechanisms mediated by natural and artificial EGFR targeting ligand, Nano Lett 12 (2012) 3417-3423.

[45] X.H. Huang, I.H. El-Sayed, W. Qian, M.A. El-Sayed, Cancer cell imaging and photothermal therapy in the near-infrared region by using gold nanorods, J. Am. Chem. Soc. 128 (2006) 2115-2120.

[46] X.H. Huang, I.H. El-Sayed, W. Qian, M.A. El-Sayed, Cancer cells assemble and align gold nanorods conjugated to antibodies to produce highly enhanced, sharp, and polarized surface Raman spectra: a potential cancer diagnostic marker, Nano Lett. 7 (2007) 1591-1597.

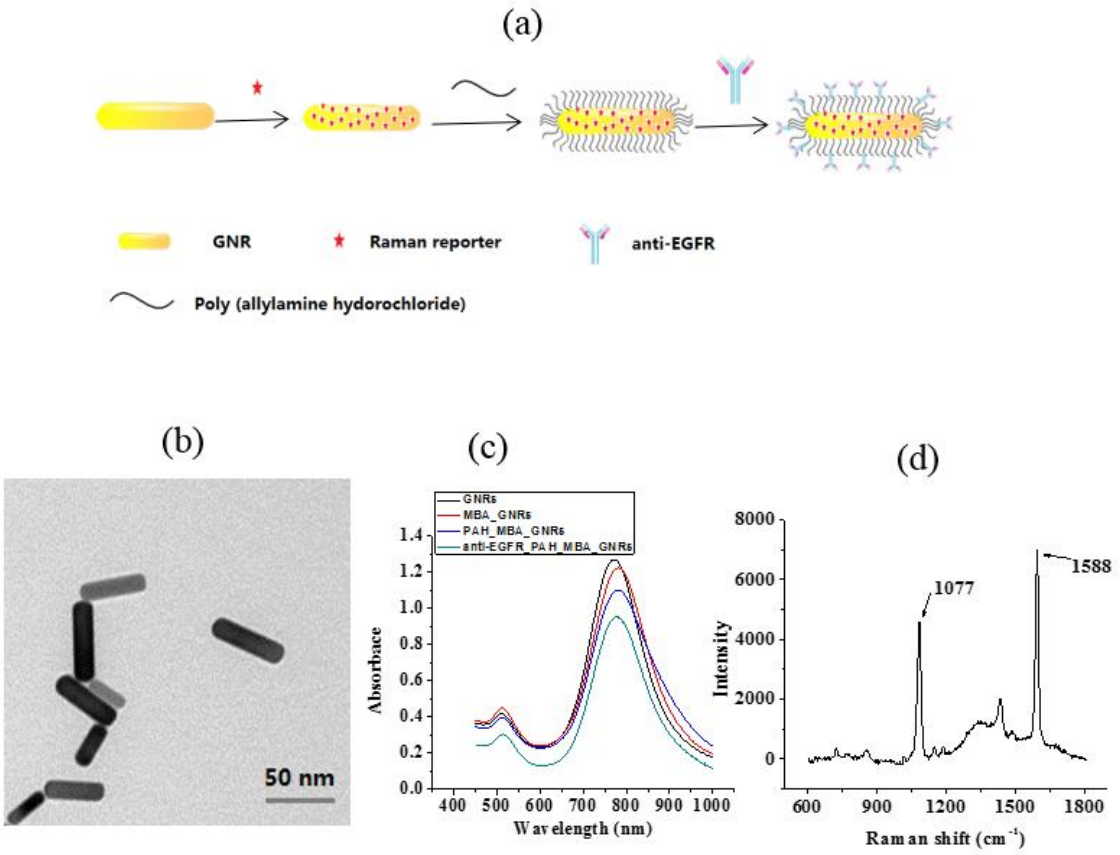


Figure 3.1 (a) Schematic illustration of the fabrication of the gold nanorods-based, antibody-functionalized SERS probe. (b-d) Characterizations of the SERS probe. (b) TEM image of the bare AuNRs, scale bar is 50 nm. (c) Extinction spectra of the AuNRs at each step of the coating process. (d) SERS spectrum of the antibody-functionalized AuNRs with 4-MBA as the reporter molecules. AuNR: gold nanorod; 4-MBA: 4-mercaptobenzoic acid.

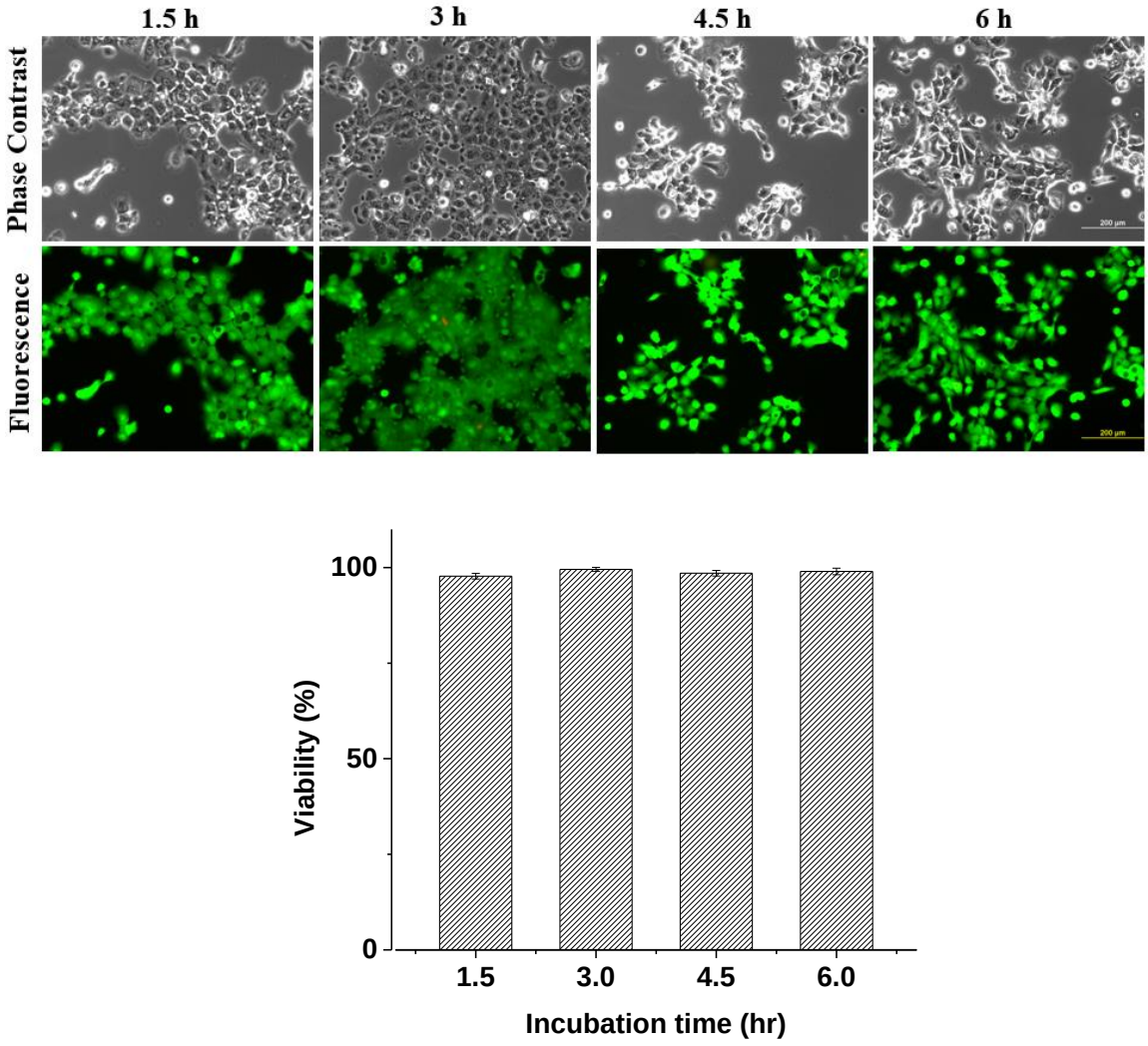


Figure 3.2 Fluorescence cell viability test. Cells were stained with Invitrogen LIVE/DEAD Viability/Cytotoxicity Assay Kit. Green fluorescence presented live cells, whereas red fluorescence showed dead or membrane-damaged cells. All images were obtained with 10× lens. The viability test shows that over 95% of A431 cells are alive after incubation with SERS probes for 1.5, 3, 4.5 and 6 hr. Over 500 cells were counted for each of the incubation times.

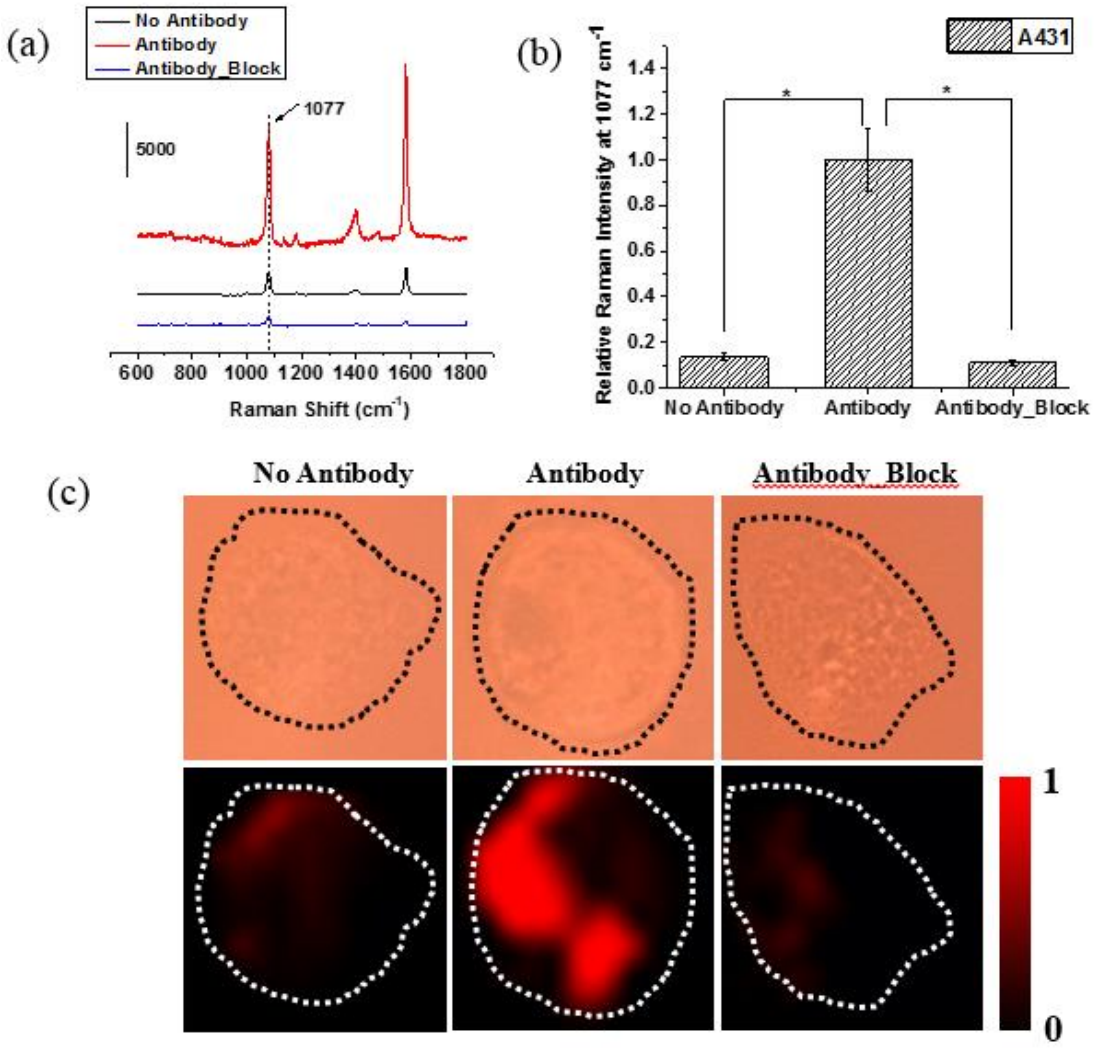


Figure 3.3 Performance assessment of constructed SERS probe. (a) Typical SERS spectra, (b) normalized average Raman intensities at 1077 cm^{-1} (curve numbers, n=60), and (c) typical single-cell bright-field and corresponding SERS mapping images of A431 cells incubated with (1) SERS probes without anti-EGFR antibody conjugation (No Antibody); (2) anti-EGFR antibody-conjugated SERS probes (Antibody); (3) free anti-EGFR antibody molecules prior to the incubation with antibody-conjugated SERS probes (Antibody_Block). Raman spectral images were created by the selection of peak 1077 cm^{-1}. The intensities were normalized between the lowest (0) and highest (1) color values. Image size: 30 × 30 μm^2. * P<0.001.

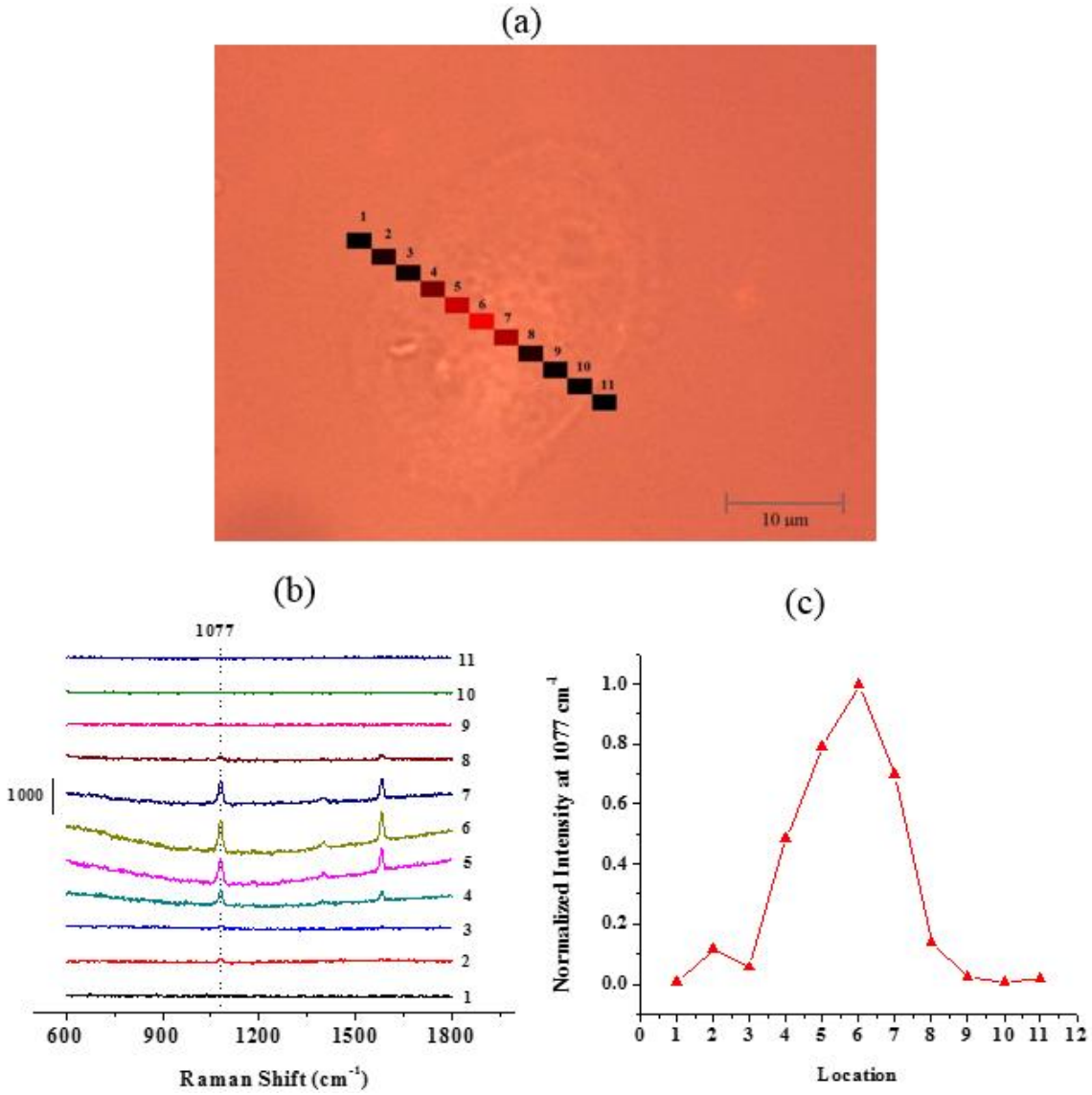


Figure 3.4 Raman line profiling of SERS probes bind to single A431 cell surface. (a) Image of an A431 cell showing 11 different locations with Raman measurements. (b) Raman profiles of the 11 points shown in (a). (c) Normalized Raman intensities at 1077 cm^{-1} at those eleven different locations.

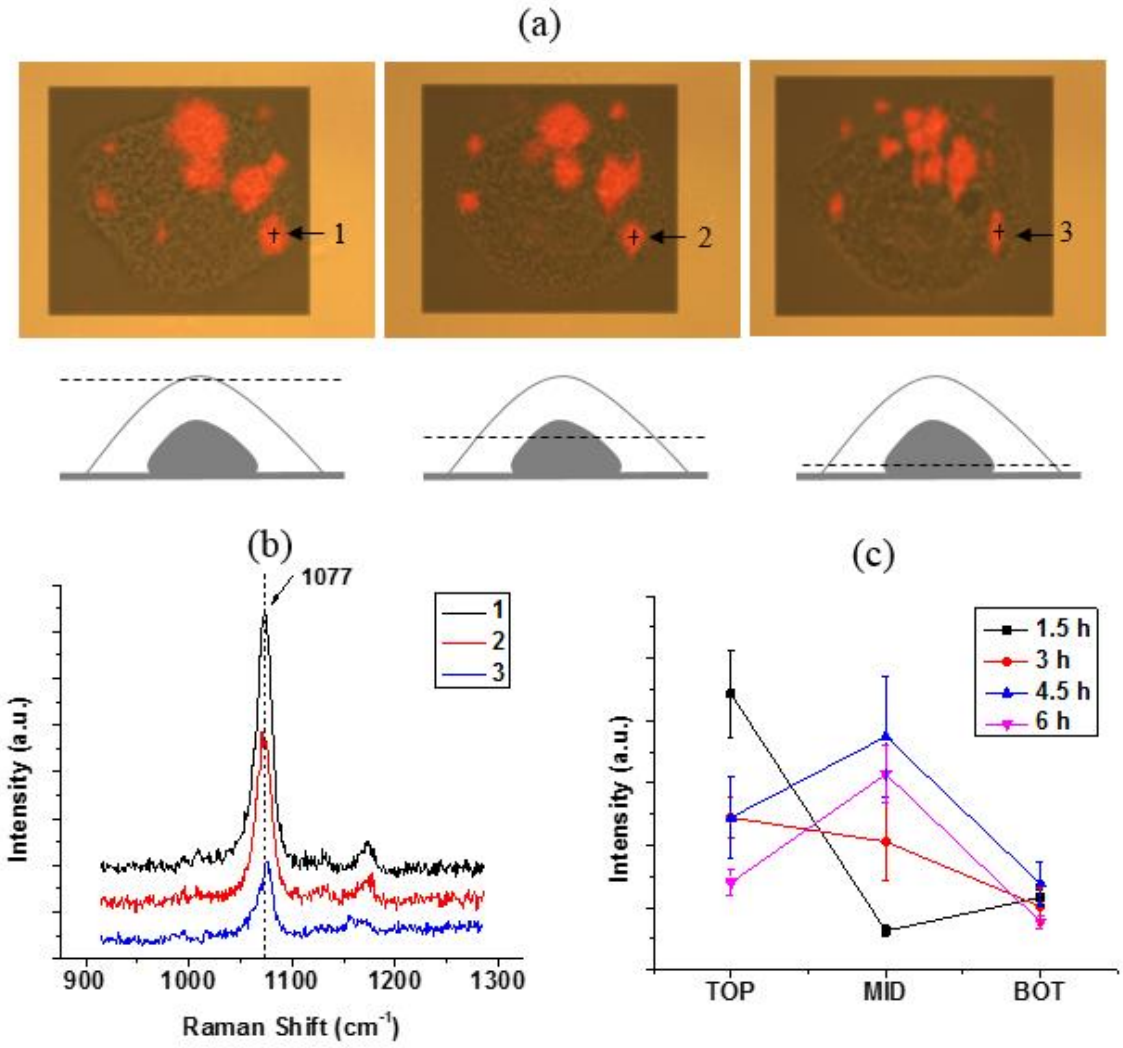


Figure 3.5 Raman depth profiling of SERS probes bound to single A431 cell surface. (a) Raman streamline mapping (at 1077 cm^{-1}) of a living A431 cell. Three images (top, middle, and bottom) were respectively obtained at three different depths (0, 3 and 6 μm), when the cells were incubated with the SERS probes for 3 hrs. (b) The typical SERS spectra measured on the single cell shown in (a) at locations 1-3 with different depths. (c) Raman intensities (1077 cm^{-1}) at different depths with 1.5, 3, 4.5 and 6 hr incubation times, n=90, Error bar: SE of mean. Image size: 52 × 39 μm^2.

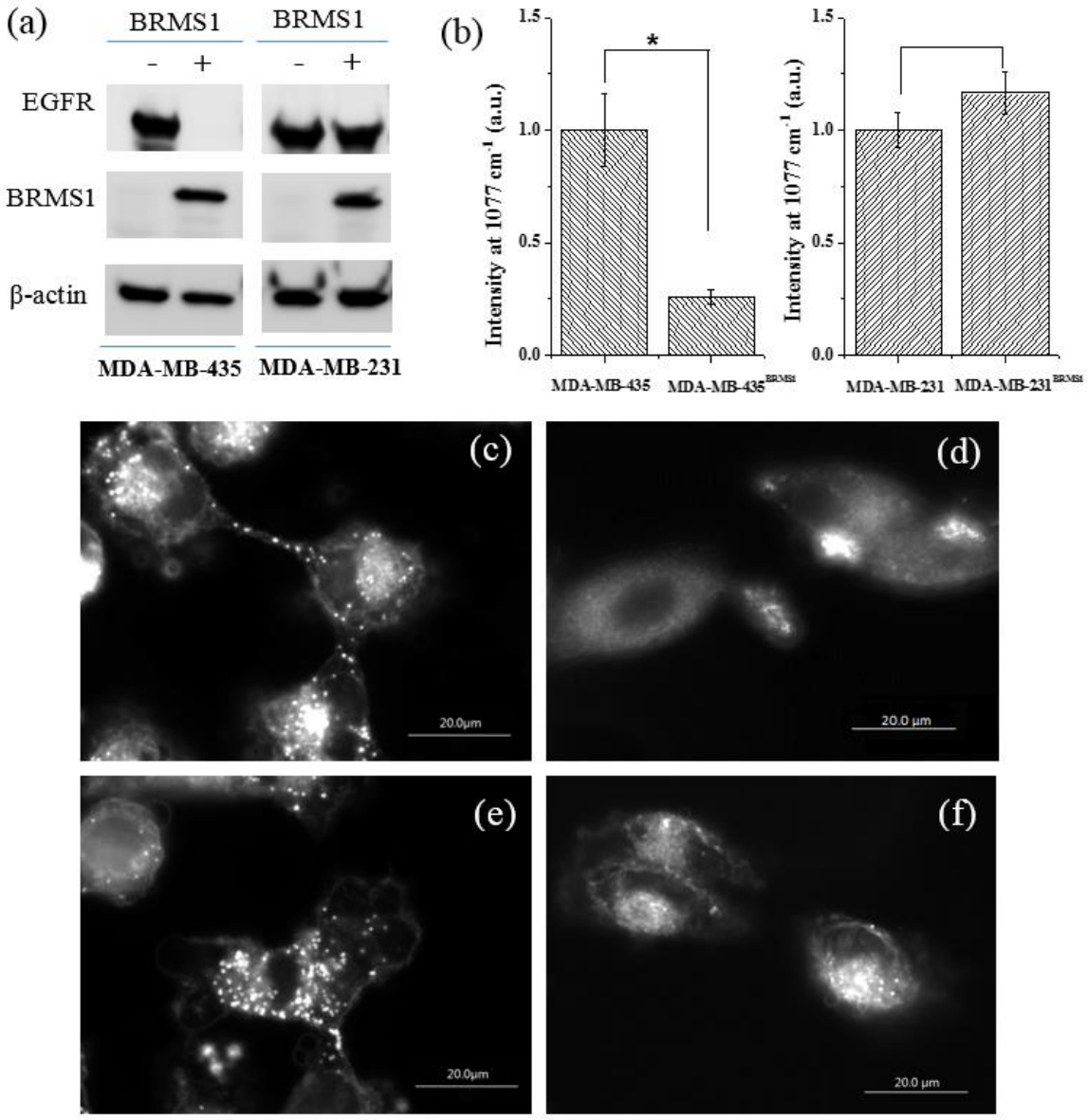


Figure 3.6 Comparison of EGFR detection by (a) immunoblotting and (b) SERS probes on MDA-MB-435 and MDA-MB-231 breast cancer cells, and their BRMS1 expressing cell lines MDA-MB-435^{BRMS1} and MDA-MB-231^{BRMS1}. (c-f) Dark field images of the SERS probes on MDA-MB-435 and MDA-MB-231 cells with (c, e) and without (d, f) BRMS1 expression. * $P<0.001$. n = 60, number of spectra collected.

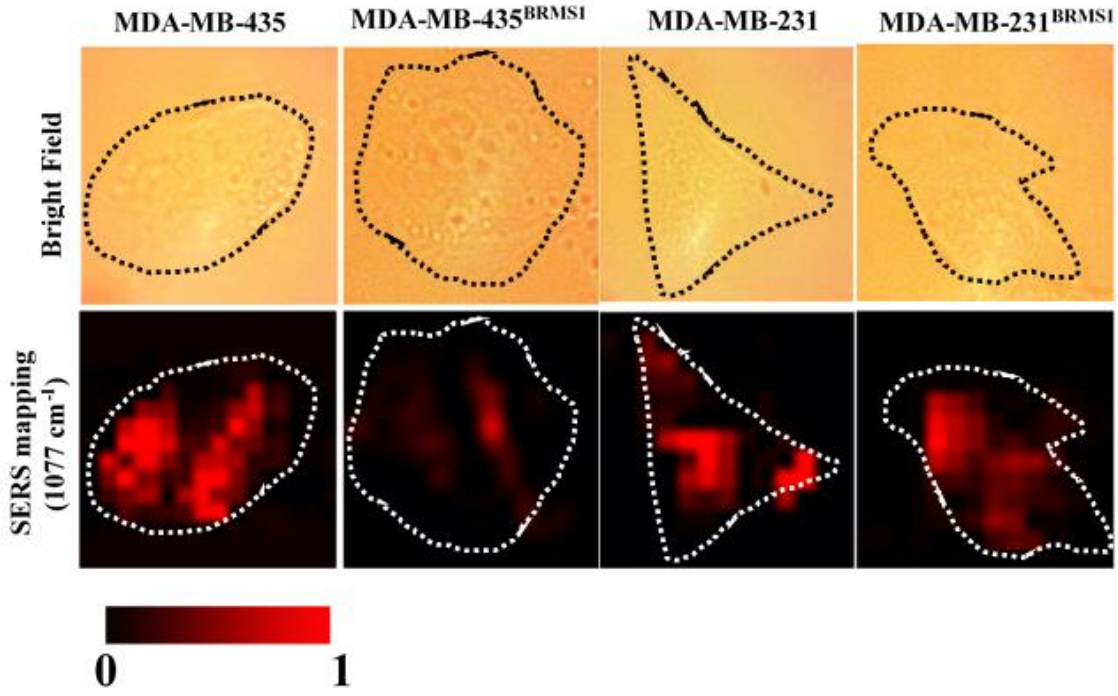


Figure 3.7 Bright field and SERS mapping (1077 cm^{-1}) images of four breast cancer cell lines: 435, 435^{BRMS1}, 231 and 231^{BRMS1}. The intensities were normalized between the lowest (0) and the highest (1) color values for each pair of 435 vs. 435^{BRMS1}, and 231 vs. 231^{BRMS1}. Mapping size for all images is 30×30 μm^2.

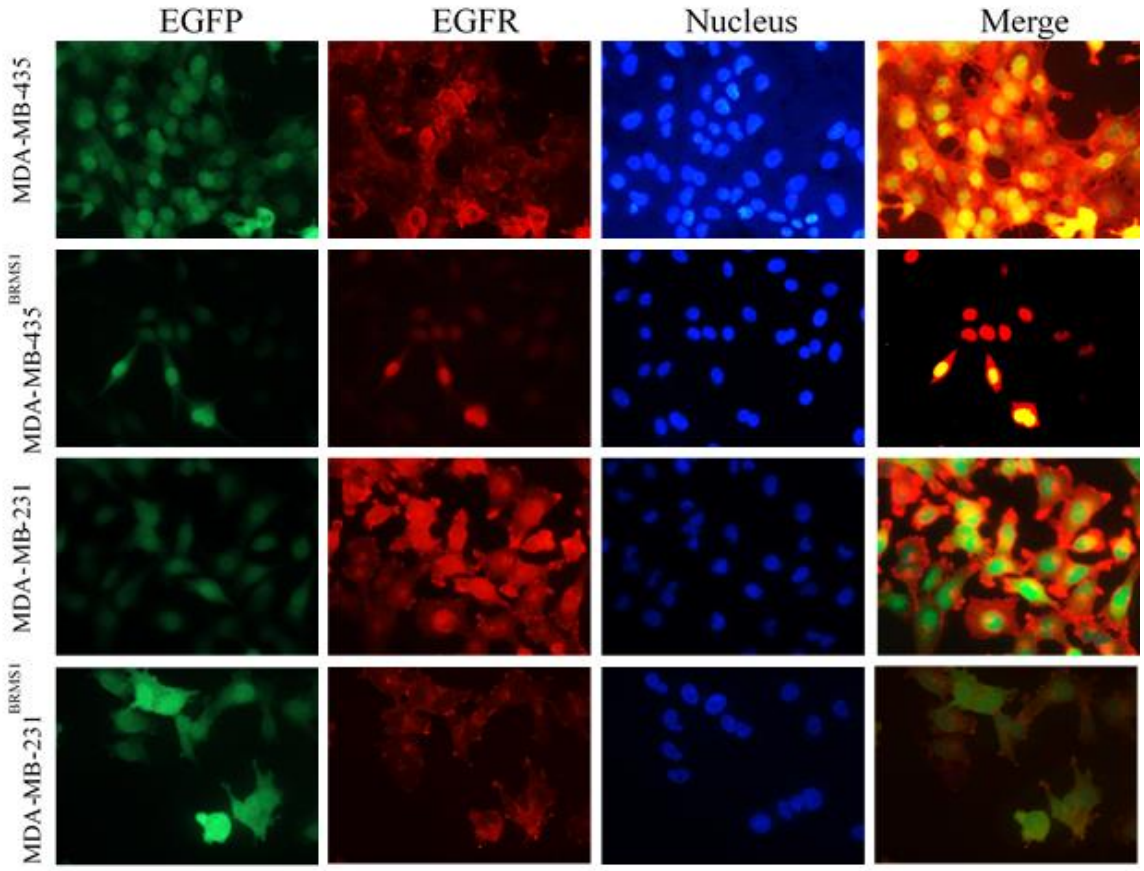


Figure 3.8 Immune-fluorescence images for showing the expression of EGFR in MDA-MB-435, MDA-MB-435^{BRMS1}, MDA-MB-231 and MDA-MB-231^{BRMS1} cells. First column: EGFP; second column: EGFR; third column: nucleus; fourth column: merge of first three columns.

CHAPTER 4

SIMULTANEOUS TOPOGRAPHIC AND SINGLE MOLECULE RECOGNITION IMAGING OF EPIDERMAL GROWTH FACTOR RECEPTOR (EGFR) ON SINGLE HUMAN BREAST CANCER CELLS

4.1 ABSTRACT

Epidermal growth factor receptor (EGFR) plays an important role in signaling pathway of the development of breast cancer cells. Since EGFR over expresses in most breast cancer cells, it is regarded as a biomarker molecule of breast cancer cells. Here we demonstrated a new AFM technique—topography and recognition imaging (TREC)—to simultaneously obtain highly sensitive and specific single-molecule recognition images and high-resolution topographic images of EGFR on single breast cancer cells.

4.2 INTRODUCTION

Epidermal growth factor receptor (EGFR) is a member of receptor tyrosine kinase (RTK) family of signaling proteins. It was the first mammalian signaling protein to be fully characterized [1]. The activation of EGFR is normally controlled by the interaction with their ligands such as EGF and TGF-α, providing cells with substantial differentiation and growth advantages [2]. However, it has been found that aberrant expression or activation of EGFR appears to be an important factor in both the initiation and the progression of human caner [3-5]. For example, in human breast carcinoma (EGFR positive), expression of EGFR was reported to support the existence of tumor cells with aggressive potentials [6]. The expression level of EGFR in metastatic breast tumors was often higher than primary tumors, indicating that EGFR was involved in the process of metastasis [7, 8]. Overexpression and abnormal function of EGFR and its ligands have been found in many

different types of human cancers [5]; this makes it a great prognostic indicator for the development of malignancies. Furthermore, therapeutic strategies have been developed, using small biomolecules (e.g. monoclonal antibody, kinase inhibitors) to block the binding of EGFR and its ligands, consequently blocking receptor activation and transduction of post-receptor signals [9, 10].

Recent study has shown that EGFR functionality can be dependent on its subcellular location and mislocated EGFR may regulate tumor response to therapy [11]. Therefore, localization of EGFR on cancer cells is of great importance. However, it is very challenging to probe the spatial and temporal distribution of specific cell receptors and their signaling-related molecular actions in molecular cell biology [12, 13]. In recent years, sophisticated technologies have been developed to achieve the identification and localization of those biomolecules in cells. Among them are (1) fluorescence imaging with improved spatial resolution, which can offer the approach to monitor the dynamic information about the localization, distribution of biomolecules and their cell-signaling actions [14, 15]; (2) electron-dense probes and electron microscopy, which provide nanometer resolution in characterizing and mapping membrane receptors and signaling molecules [16]; (3) a combination of quantitative mass spectrometry and cryo-electron tomography, providing insights into the distribution of specific protein complexes in cytoplasm [17, 18]. Although these advanced technologies have significantly improved the capability of detecting and localizing cell receptors, some limitations still remain: high spatial and temporal resolution, the requirement of physiological and dynamic condition, and the chemical specificity. Few techniques can overcome all these limitations and provide critical measurements of cell membrane receptors.

Since its invention in 1980s, atomic force microscopy (AFM) has become a powerful tool technique for analyzing the morphology of individual molecules at nanometer scale and the forces acting on them with piconewton sensitivity. As to the study of biological samples, AFM presents significant advantages than other microscopic methods since it allows single-molecule level studies of the structure and interaction of complicated biomolecules and cells with nanometer spatial resolution [19], and it allows samples to be measured in liquid phase, enabling the study of dynamic interactions between biomolecules under physiological condition. Simultaneous Topography and RECognition (TREC) imaging, a new AFM technique based on the high-resolution topographic imaging and single-molecule force measurement [20, 21], has been developed for receptor imaging with high spatial and temporal resolution, providing exceptional information that is complementary to that obtained by fluorescence and electron microscopy [22]. For example, TREC imaging has been successfully used to visualize, at the first time, the localization and distribution of Na^+-K^+ ATPases in the inner leaflet of cell membranes at single-molecule level [23]; by employing TREC, the local organization of Fcγ receptors on single macrophage cell has been determined at single-molecule level [24]. In addition to cell receptor imaging, TREC imaging technique has also been extensively used to monitor specific biomolecules while they are undergoing biological processes. Wang *et al.* [20, 25, 26] applied TREC to study the action of human Swi-Snf nucleosome remodeling complex and its interaction with mouse mammary tumor virus promoter during the process of nucleosome remodeling, proving the crucial role of ATP activation in the process. Besides, they were also able to recognize the glycosylation process of

biomolecules by using TREC imaging, and distinguish normal and aberrant antibodies based on their glycosylation [27].

In this context, we applied TREC imaging method to detect and localize EGFR at single molecule level. Single molecule recognition using monoclonal antibody (anti-EGFR) tethered scanning tip was converted to high resolution Topography and Recognition images. The recognition efficiency was tested in a spatio-temporal manner by introducing EGF as a competing ligand, when conducting TREC imaging of EGFR using antibody-tethered AFM tips. We measured the density and distribution of EGFR on breast cancer cell lines—MDA-MB-435 (435) and 435 transfected with BRMS1 gene (BReast cancer Metastasis Supressor 1 [28, 29], 435^{BRMS1}). In addition, the advantages of TREC imaging over conventional detection methods (e.g. immunofluorescence, western blot) have been discussed.

4.3 MATERIALS AND METHODS

4.3.1 Sample preparation and cell culture

For TREC imaging on mica, epidermal growth factor receptor (EGFR, Life Technologies, Grand Island, NY) solution (21μg/ml, in 0.1X PBS) was dropped onto newly pealed mica surface and left 10min for adsorption. Rinse several times with DI water to wash away incompletely adsorbed EGFR and then load mica onto sample plate for recognition imaging.

435 and 435^{BRMS1} cells were measured. 435^{BRMS1} cells were transfected with a lentiviral vector construct expressing full length BRMS1 cDNA under the control of a cytomegalovirus promoter [30]. 435 and 435^{BRMS1} cells were cultured in a 1:1 mixture of Dulbecco's-modified eagle's medium (DMEM) and Ham's F-12 medium supplemented

with 5% fetal bovine serum (Hyclone, Logan, UT). Cells were cultured in 25-cm^2 corning tissue culture dishes at 37 ℃ with 5% CO2 in a humidified atmosphere. Cells were passaged at 80–90% confluence using 2 mM EDTA in Ca^{2+}/Mg^2-free PBS (PBS, 0.01 M, pH 7.4, Thermo Scientific). Cell lines were confirmed to be free of mycoplasma contamination using PCR (TaKaRa-Clontech, Mountain View, CA). No antibiotics or antimycotics were used during routine culture. For TREC imaging on cell surface, cells were fixed with paraformaldehyde and measured in PBS buffer.

4.3.2 AFM tip functionalization

Magnetically coated silicon-nitride AFM tips (Type VI MAC Levers, Agilent Technologies, Chandler, AZ) were functionalized with anti-EGFR antibody using the method reported previously [20]. Briefly, MAC levers were first amino-functionalized with APTES (aminopropyltriethoxysilane, Sigma-Aldrich, St. Louis, MO) under the atmosphere of argon. Subsequently, after rinsing with methylene chloride (Sigma-Aldrich) for 3 times, MAC levers were attached to NHS-PEG-SS-Pyr (PolyPure, Oslo, Norway) by incubating the tips with the PEG linker for 2hr, with the presence of triethylamine. At the same time, monoclonal antibody to EGFR (anti-EGFR, Life Technologies, Grand Island, NY) was thiolated by reacting with with N-cuccinimidyl 3-(acetylthio) propionate (SATP, Sigma-Aldrich) and subsequently purified in a PD-10 column (GE Healthcare). Finally, the thiolated antibody was conjugated to the AFM tip via the PEG crosslinker by 1h incubation in deacetylation buffer (hydroxylamine hydrochloride and Triz Base, Sigma Aldrich). Antibody functionalized MAC levers were then rinsed with PBS buffer and stored in 4 ℃ before use.

4.3.3 AFM recognition imaging

AFM recognition imaging was performed on a PicoPlus AFM system with a commercially available electronic attachment (PicoTREC, Agilent Technologies). Topography and recognition images were recorded simultaneously by using functionalized MAC levers with nominal spring constant of 0.292 N/m. During TREC measurement, a half-amplitude feedback loop was used to measure the unbiased topography. Eight to ten nm free oscillation amplitude and ~20 kHz driving frequency of the tips were chosen to obtain optimized recognition images. All these parameters were set to make the TREC measurements more easy, robust and reliable [31]. Image processes (including smooth, contrast adjustment) and the height and width measurements of tested proteins were performed using PicoView software (Agilent Technologies).

The single cell AFM images were taken under contact mode with the instrument setting exactly the same as previously described [32, 33].

4.3.4 Image processing

We employ an adaptive threshold-based segmentation method to find white spots in a topological image and dark spots in a recognition image. We first convert the original color image to a grayscale image. For the recognition image, we also invert its intensity so the darkest spot turns to the brightest spot and vice versa. After this processing, we aim to separately find white spots in the grayscale image of the topological image and the inverted grayscale image of the recognition image. To this end, we first compute the average intensity and the standard deviation of the grayscale image. The threshold is then computed as the sum of the average intensity and the standard deviation. For the topological image, we simply mark any position with the pixel intensity larger than the

threshold as the white spot. For the recognition image, we similarly mark any position with the pixel intensity larger than the threshold as the dark spot due to the inversion process. Finally, we apply a logical "AND" operation to find the common areas shown up in both white spots of the topological image and dark spots of its paired recognition image. These areas are then overlaid on top of the original topological image to show the white spots in topological image that have been simultaneously recognized in the recognition image as the dark spots.

We implemented the image segmentation method using Matlab 2012(b).

4.4 RESULTS

4.4.1 Functionalization and SEM characterization of AFM MAC lever

Functionalization of AFM MAC Lever tips with anti-EGFR antibody was the key point to achieve successful TREC measurements. As shown in Figure 4.1a, a procedure with 4 steps involved has been implemented to conjugate anti-EGFR monoclonal antibody with AFM tip to construct an EGFR-specific AFM nanosensor tip. It should be noted that, in this method, a PEG chain was applied to link the tip and the antibody due to its flexibility that allows for reorientation of the sensor molecule when the tip approaches the surface [34, 35]. The free oscillation amplitude was set comparable to the extended length of the PEG linker (~8nm) so that antibody on the tip remained bounding to the antigen on the surface during imaging and kept high lateral accuracy as well [35]. The morphologies of bare MAC Lever tip (Figure 4.1b) and anti-EGFR antibodies modified tip (Figure 4.1c) were characterized by scanning electron microscope (SEM). It is clearly seen that the morphology of modified probe was different from bare probe with the presence of “bumps” or “clusters” on the surface.

4.4.2 Specificity, Efficiency and Reproducibility of TREC

To evaluate the feasibility and efficiency of this TREC imaging method, we first chose mica as the substrate, since it's flat at atomic level and its much simpler circumstances than cell membrane surface. EGFR molecules were adsorbed onto the mica surface through electrostatic interaction. When anti-EGFR antibody-tethered AFM tip approached the surface and scanned through the surface, antibody-antigen recognition events occurred, simultaneously generating maps of the surface topography (Figure 4.2a) and recognition (Figure 4.2b) signals. "Bright spots" on Figure 4.2a represent single molecules or aggregates of EGFR, and the corresponding "dark spots" on Figure 4.2b represent the recognition events of EGFR. These events were originated from the tip-tethered antibody binds to antigens, restricting the tip to oscillate upwards and leading to the reduction of the oscillation amplitude. To test the specificity of the recognition process, an anti-EGFR solution (20 μg/mL) was injected via a liquid flow cell to block the interaction between tip-tethered anti-EGFR and EGFR on the surface. After 10 min adsorption, "dark spots" on recognition image were disappeared when conducting scan on the same location (Figure 4.2c). Cross section analysis along the recognition events (green lines on Figure 4.2a, b, and c) showed that before free anti-EGFR blocking, there were significant recognition signals (Figure 4.2e) corresponding to the topography signals (Figure 4.2d), which indicated the height of molecules on the surface; however, as blocked by excess specific antibody, recognition signals of the antigens were dramatically decreased (Figure 4.2f). Furthermore, as a control experiment, bare tip was employed to scan EGFR on mica surface (Figure 4.3a). Apparent features on topography image were presented, while no features were shown on recognition image. After a BSA solution (50

μg/mL) was injected and let adsorbed for 10 min, recognition events still appeared as antibody-tethered tip scanning on the surface (Figure 4.3b), showing that non-specific protein-protein interaction wouldn't affect the recognition. All these results indicate the recognition events were highly specific—only EGFR molecules were recognized when sensing with anti-EGFR antibody-tethered AFM tip.

Efficiency of the EGFR recognition was also tested on mica. As shown in Figure 4.4, bright spots in topography image and dark spots in recognition image were labeled by a pair of green dots, representing a pair of recognition events took place. In this typical image, almost all features (45 out of 47) in topography image were recognized, indicating perfect recognition efficiency of this TREC imaging method to detect EGFR through specific antibody-antigen interaction. In addition, to test the reproducibility of recognition, the sample was rescanned at the same position. Only a few changes labeled with blue dots and circles had happened in the rescan of the same area, showing generally high reproducibility of the recognition.

4.4.3 EGF effects on TREC imaging of EGFR

EGF acts as a competing ligand that may affect the recognition of EGFR by AFM tip-tethered anti-EGFR. To investigate how EGF affects the antibody-antigen recognition between EGFR and its antibody, we applied TREC imaging to measure EGFR on mica with and without EGF presence. As shown in Figure 4.5, when EGFR was presented alone on the mica surface (Figure 4.5a), the recognition events (green) occurred at the most of the "bright spots" area, indicating the high recognition efficiency between the tip-tethered antibody and the EGFR; however, the TREC image scanned at 10 min after EGF (20 μg/mL) introduction (Figure 4.5b) showed only reduced level of recognition, revealing the

incomplete blocking by EGF on the binding sites between EGFR and its antibody. Analyses of multiple images show that the average recognition percentage dropped from 84.3% to 57.4% when EGF is presented as a competitor (Figure 4.5c). Comparing the partial block by EGF with the complete block by anti-EGFR antibody (Figure 4.2c), it is suggested that the binding affinity to EGFR is higher for anti-EGFR antibody than for EGF.

4.4.4 TREC Imaging of EGFR on 435 and 435^{BRMS1} cells

Morphologies of single 435 and 435^{BRMS1} cells were visualized by contact mode AFM, and they have been shown to be very different (Figure 4.6a-d). Typical topography and deflection images of 435 cells are shown in Figure 4.6a and c. The shape of 435 cells was observed to be round-like and the nucleic area possessed the most part of cell, which is typical for cancer cells. Nevertheless, as shown in Figure 4.6b and d, the 435^{BRMS1} cell has an elongated morphology and nucleus is smaller comparing with the 435 cell. Changes in cell morphology caused by BRMS1 transfection has also been previously reported [36]. While features like chemosensitivity were not significantly affected by BRMS1 [37], the BRMS1 did regulate the expression of several cellular receptors, such as EGFR [8, 38].

TREC imaging method was carried out to further probe the local distribution of EGFR molecules on the membrane surface of 435 and 435^{BRMS1} cells. Comparing with the TREC images on mica surface, the images on cells were less distinct with the distribution of EGFR due to the complexity of cell membrane surface. We then applied an image segmentation method to find out the corresponding “recognition sites” in topography and recognition images, and superimpose the recognitions sites (green) onto corresponding topography images (Figure 4.7a). The presence of recognition events were also confirmed by the corresponding peaks occurred in the line profiles along the images (Figure 4.7b). It

is found that EGFR heterogeneously distributed on 435 cells and tended to form domains with a scale of a few nanometers (Figure 4.6e); with the expression of BRMS1, the numbers of EGFR binding sites reduced and smaller domains were observed (Figure 4.6f). The smallest "clusters" showing the recognition sites of EGFR molecules were nanometer scale, which is comparative to the size of single molecule of EGFR, indicating that TREC is able to achieve analysis of biomolecules at single-molecule level. Furthermore, the whole imaging process was done within several min, which means TREC imaging is capable of in situ monitoring many biological processes such as the activation of EGFR molecules by their specific ligands (e.g. EGF, TGF-α).

4.5 DISCUSSION

4.5.1 BRMS1 role in EGFR regulation

It has been known that BRMS1 is a member of metastasis suppressors, which inhibit metastasis without blocking orthotopic tumor formation in metastatic cascade [39, 40]. Previous studies have shown that the expression of BRMS1 in 435 cells regulates biomechanical properties including cell adhesion and cell elasticity [36], which probably induced by reorganization of cytoskeletal structures [41, 42]. Also, it has been reported that BRSM1 regulates the expression of growth factor receptors in 435 cells by differentially modulates their signaling pathway [8]. Aberrant EGFR signaling results in many pathological diseases like neural developmental disorders and cancer [43]. Further, EGFR signaling is mainly up-regulated in breast cancers through activation of NF-κB activity, and BRMS1 has been shown to affect NF-κB activity [44, 45]. To probe this link, we explored whether BRMS1 altered signaling through EGFR. Our previous work [38] has confirmed that BRSM1 down-regulated the expression of EGFR in 435 breast carcinoma

cells. However, up to now, there is no study reported the ability to obtain the information about the local distribution of EGFR with nanoscale spatial resolution, which is necessary to study the cellular biology of cell receptors, such as the interaction between receptors and their specific ligands. TREC imaging presented high specificity, reproducibility and recognition efficiency at nanoscale. Therefore, TREC imaging method has been applied in order to identify the local binding sites of EGFR on single breast cancer cells.

4.5.2 Biological application of TREC imaging

Figure 4.8 briefly shows the principle of TREC imaging method. The basic principle of TREC imaging is based on small alterations in cantilever oscillation amplitude that occur when tip-tethered antibodies bind to their antigens. When the oscillating antibody-tethered AFM tip scans through the sample, the tethered antibody binds to an antigen on the surface and the upward oscillation of the cantilever is restricted by specific antibody-antigen binding force, leading to the decrease in the oscillation amplitude. This reduction of amplitude is sensed by the microscope servo and converted into reduction of the recognition signal (peak voltages). Therefore, a map of recognition signals, together with simultaneously generated topographic image, localizes the antibody-antigen binding events with pairs of bright and dark spots showing on the image.

Applications of TREC technique in biomedical research is certainly an increasingly demanding task. Up to now, TREC imaging method has been applied to visualize quite a few different biomolecule systems, such as biotin-avidin [46, 47], ligand-receptor [48, 49], and antibody-antigen interactions [20, 23]. In this study, we utilized TREC imaging to visualize EGFR molecules on complex cell membrane surface, providing a new example of the applications of this methodology in biomedical research. Due to the significant role

of EGFR in cancer research, our work appears to inspire an alternative approach to primary cancer diagnostics. Furthermore, TREC approach has the potential to study the dynamic activation process of EGFR, which is of great significance, because EGFR can be activated by its specific ligands (e.g. EGF, TGF-α), leading to the growth and spread of tumor [50]. Time resolution may be the concern. At present, it takes several min to record a recognition image, which is more than enough for the activation and endocytosis of EGFR molecules.

4.6 REFERENCES

[1] A. Ullrich, L. Coussens, J.S. Hayflick, T.J. Dull, A. Gray, A.W. Tam, J. Lee, Y. Yarden, T.A. Libermann, J. Schlessinger, J. Downward, E.L.V. Mayes, N. Whittle, M.D. Waterfield, P.H. Seeburg, Human epidermal growth factor receptor cDNA sequence and aberrant expression of the amplified gene in A431 epidermoid carcinoma cells, Nature 309 (1984) 418-425.

[2] D. Gospodarowicz, Epidermal and nerve growth factors in mammalian development, Annu. Rev. Physiol. 43 (1981) 251-263.

[3] D.S. Salomon, R. Brandt, F. Ciardiello, N. Normanno, Epidermal growth factor related peptides and their receptors in human malignancies, Crit. Rev. Oncol. Hemat. 19 (1995) 183-232.

[4] K. Khazaie, V. Schirrmacher, R.B. Lichtner, EGF receptor in neoplasia and metastasis, Cancer Metast. Rev. 12 (1993) 255-274.

[5] R.I. Nicholson, J.M.W. Gee, M.E. Harper, EGFR and cancer prognosis, Eur. J. Cancer 37 (2001) S9-S15.

[6] M. Bilous, J. Milliken, J.M. Mathijs, Immunocytochemistry and in situ hybridization of epidermal growth factor receptor and relation to prognostic factors in breast cancer, Eur. J. Cancer 28 (1992) 1033-1037.

[7] M. Toi, A. Osaki, H. Yamada, T. Toge, Epidermal growth factor receptor expression as a prognostic indicator in breast cancer, Eur. J. Cancer 27 (1991) 977-980.

[8] K.S. Vaidya, S. Harihar, P.A. Phadke, L.J. Stafford, D.R. Hurst, D.G. Hicks, G. Casey, D.B. DeWald, D.R. Welch, Breast cancer metastasis suppressor-1 differentially modulates growth factor signaling, J. Biol. Chem. 283 (2008) 28354-28360.

[9] E.K. Rowinsky, The erbB family: targets for therapeutic development against cancer and therapeutic strategies using monoclonal antibodies and tyrosine kinase inhibitors, Annu. Rev. Med. 55 (2004) 433-457.

[10] N.E. Hynes, H.A. Lane, ERBB receptors and cancer: the complexity of targeted inhibitors, Nat. Rev. Cancer 5 (2005) 341-354.

[11] W. Han, H.W. Lo, Landscape of EGFR signaling network in human cancers: biology and therapeutic response in relation to receptor subcellular locations, Cancer Lett. 318 (2012) 124-134.

[12] J.Y. Yang, M. Reth, Oligomeric organization of the B-cell antigen receptor on resting cells, Nature 467 (2010) 465-469.

[13] M. Beck, M. Topf, Z. Frazier, H. Tjong, M. Xu, S.H. Zhang, F. Alber, Exploring the spatial and temporal organization of a cell's proteome, J. Struct. Biol. 173 (2011) 483-496.

[14] J.N. Werner, E.Y. Chen, J.M. Guberman, A.R. Zippilli, J.J. Irgon, Z. Gitai, Quantitative genome-scale analysis of protein localization in an asymmetric bacterium, Proc. Natl. Acad. Sci. USA 106 (2009) 7858-7863.

[15] D.R. Stabley, C. Jurchenko, S.S. Marshall, K.S. Salaita, Visualizing mechanical tension across membrane receptors with a fluorescent sensor, Nat. Methods 9 (2012) 64-67.

[16] J. Zhang, K. Leiderman, J.R. Pfeiffer, B.S. Wilson, J.M. Oliver, S.L. Steinberg, Characterizing the topography of membrane receptors and signaling molecules from spatial patterns obtained using nanometer-scale electron-dense probes and electron microscopy, Micron 37 (2006) 14-34.

[17] M. Beck, J.A. Malmstrom, V. Lange, A. Schmidt, E.W. Deutsch, R. Aebersold, Visual proteomics of the human pathogen Leptospira interrogans, Nat. Methods 6 (2009) 817-U855.

[18] K. Grunewald, Adding a spatial dimension to the proteome, Nat. Methods 6 (2009) 798-800.

[19] J.K.H. Horber, M.J. Miles, Scanning probe evolution in biology, Science 302 (2003) 1002-1005.

[20] C. Stroh, H. Wang, R. Bash, B. Ashcroft, J. Nelson, H. Gruber, D. Lohr, S.M. Lindsay, P. Hinterdorfer, Single-molecule recognition imaging-microscopy, Proc. Natl. Acad. Sci. USA 101 (2004) 12503-12507.

[21] P. Hinterdorfer, Y.F. Dufrene, Detection and localization of single molecular recognition events using atomic force microscopy, Nat. Methods 3 (2006) 347-355.

[22] L.A. Chtcheglova, P. Hinterdorfer, Simultaneous topography and recognition imaging on endothelial cells, J. Mol. Recognit. 24 (2011) 788-794.

[23] J.G. Jiang, X. Hao, M.J. Cai, Y.P. Shan, X. Shang, Z.Y. Tang, H.D. Wang, Localization of Na^+-K^+ ATPases in quasi-native cell membranes, Nano Lett. 9 (2009) 4489-4493.

[24] S.F. Ahmad, L.A. Chtcheglova, B. Mayer, S.A. Kuznetsov, P. Hinterdorfer, Nanosensing of Fcγ receptors on macrophages, Anal. Bioanal. Chem. 399 (2011) 2359-2367.

[25] H. Wang, R. Bash, J.G. Yodh, G. Hager, S.M. Lindsay, D. Lohr, Using atomic force microscopy to study nucleosome remodeling on individual nucleosomal arrays in situ, Biophys. J. 87 (2004) 1964-1971.

[26] H. Wang, R. Bash, S.M. Lindsay, D. Lohr, Solution AFM studies of human Swi-Snf and its interactions with MMTV DNA and chromatin, Biophys. J. 89 (2005) 3386-3398.

[27] H.D. Wang, L. Obenauer-Kutner, M. Lin, Y.P. Huang, M.J. Grace, S.M. Lindsay, Imaging glycosylation, J. Am. Chem. Soc. 130 (2008) 8154-8155.

[28] M.J. Seraj, R.S. Samant, M.F. Verderame, D.R. Welch, Functional evidence for a novel human breast carcinoma metastasis suppressor, BRMS1, encoded at chromosome 11q13, Cancer Res. 60 (2000) 2764-2769.

[29] L.J. Stafford, K.S. Vaidya, D.R. Welch, Metastasis suppressors genes in cancer, Int. J. Biochem. Cell B 40 (2008) 874-891.

[30] P.A. Phadke, K.S. Vaidya, K.T. Nash, D.R. Hurst, D.R. Welch, BRMS1 suppresses breast cancer experimental metastasis to multiple organs by inhibiting several steps of the metastatic process, Am. J. Pathol. 172 (2008) 809-817.

[31] J. Preiner, A. Ebner, L. Chtcheglova, R. Zhu, P. Hinterdorfer, Simultaneous topography and recognition imaging: physical aspects and optimal imaging conditions, Nanotechnology 20 (2009) 215103.

[32] M.J. Tang, Q.F. Li, L.F. Xiao, Y.P. Li, J.L. Jensen, T.G. Liou, A.H. Zhou, Toxicity effects of short term diesel exhaust particles exposure to human small airway epithelial cells (SAECs) and human lung carcinoma epithelial cells (A549), Toxicol. Lett. 215 (2012) 181-192.

[33] L. Xiao, M. Tang, Q. Li, A. Zhou, Noninvasive detection of biomechanical and biochemical responses of human lung cells to short time chemotherapy exposure using AFM and confocal Raman spectroscopy, Anal. Methods 5 (2013) 874-879.

[34] A.S.M. Kamruzzahan, A. Ebner, L. Wildling, F. Kienberger, C.K. Riener, C.D. Hahn, P.D. Pollheimer, P. Winklehner, M. Holzl, B. Lackner, D.M. Schorkl, P. Hinterdorfer, H.J. Gruber, Antibody linking to atomic force microscope tips via disulfide bond formation, Bioconjugate Chem. 17 (2006) 1473-1481.

[35] C.K. Riener, C.M. Stroh, A. Ebner, C. Klampfl, A.A. Gall, C. Romanin, Y.L. Lyubchenko, P. Hinterdorfer, H.J. Gruber, Simple test system for single molecule recognition force microscopy, Anal. Chim. Acta 479 (2003) 59-75.

[36] Y.Z. Wu, G.D. McEwen, S. Harihar, S.M. Baker, D.B. DeWald, A.H. Zhou, BRMS1 expression alters the ultrastructural, biomechanical and biochemical properties of MDA-MB-435 human breast carcinoma cells: an AFM and Raman microspectroscopy study, Cancer Lett. 293 (2010) 82-91.

[37] K.S. Vaidya, J.J. Sanchez, E.L. Kim, D.R. Welch, Expression of the Breast Cancer Metastasis Suppressor 1 (BRMS1) maintains in vitro chemosensitivity of breast cancer cells, Cancer Lett. 281 (2009) 100-107.

[38] L. Xiao, S. Harihar, D.R. Welch, A. Zhou, Imaging of epidermal growth factor receptor on single breast cancer cells using surface-enhanced Raman spectroscopy, Anal. Chim. Acta 843 (2014) 73-82.

[39] C.W. Rinker-Schaeffer, J.P. O'Keefe, D.R. Welch, D. Theodorescu, Metastasis suppressor proteins: discovery, molecular mechanisms, and clinical application, Clin. Cancer Res. 12 (2006) 3882-3889.

[40] P.S. Steeg, Metastasis suppressors alter the signal transduction of cancer cells, Nat. Rev. Cancer 3 (2003) 55-63.

[41] P.J. Champine, J. Michaelson, B.C. Weimer, D.R. Welch, D.B. DeWald, Microarray analysis reveals potential mechanisms of BRMS1-mediated metastasis suppression, Clin. Exp. Metastas. 24 (2007) 551-565.

[42] D.B. DeWald, J. Torabinejad, R.S. Samant, D. Johnston, N. Erin, J.C. Shope, Y. Xie, D.R. Welch, Metastasis suppression by breast cancer metastasis suppressor 1 involves reduction of phosphoinositide signaling in MDA-MB-435 breast carcinoma cells, Cancer Res. 65 (2005) 713-717.

[43] Y. Yarden, M.X. Sliwkowski, Untangling the ErbB signalling network, Nat. Rev. Mol. Cell Bio. 2 (2001) 127-137.

[44] G. Sethi, K.S. Ahn, M.M. Chaturvedi, B.B. Aggarwal, Epidermal growth factor (EGF) activates nuclear factor-κB through IκBα kinase-independent but EGF receptor-kinase dependent tyrosine 42 phosphorylation of IκBα, Oncogene 26 (2007) 7324-7332.

[45] M. Cicek, R. Fukuyama, D.R. Welch, N. Sizemore, G. Casey, Breast cancer metastasis suppressor 1 inhibits gene expression by targeting nuclear factor-κB activity, Cancer Res. 65 (2005) 3586-3595.

[46] C.M. Stroh, A. Ebner, M. Geretschlager, G. Freudenthaler, F. Kienberger, A.S.M. Kamruzzahan, S.J. Smith-Gil, H.J. Gruber, P. Hinterdorfer, Simultaneous topography and recognition Imaging using force microscopy, Biophys. J. 87 (2004) 1981-1990.

[47] A. Ebner, F. Kienberger, C. Huber, A.S.M. Kamruzzahan, V.P. Pastushenko, J.L. Tang, G. Kada, H.J. Gruber, U.B. Sleytr, M. Sara, P. Hinterdorfer, Atomic-force-microscopy imaging and molecular-recognition-force microscopy of recrystallized heterotetramers comprising an S-layer-streptavidin fusion protein, Chembiochem 7 (2006) 588-591.

[48] L. Lin, H.D. Wang, Y. Liu, H. Yan, S. Lindsay, Recognition imaging with a DNA aptamer, Biophys. J. 90 (2006) 4236-4238.

[49] L. Lin, D. Hom, S.M. Lindsay, J.C. Chaput, In vitro selection of histone H4 aptamers for recognition imaging microscopy, J. Am. Chem. Soc. 129 (2007) 14568-14569.

[50] R. Singh, P. Lei, S.T. Andreadis, PKC-δ binds to E-cadherin and mediates EGF-induced cell scattering, Exp. Cell Res. 315 (2009) 2899-2913.

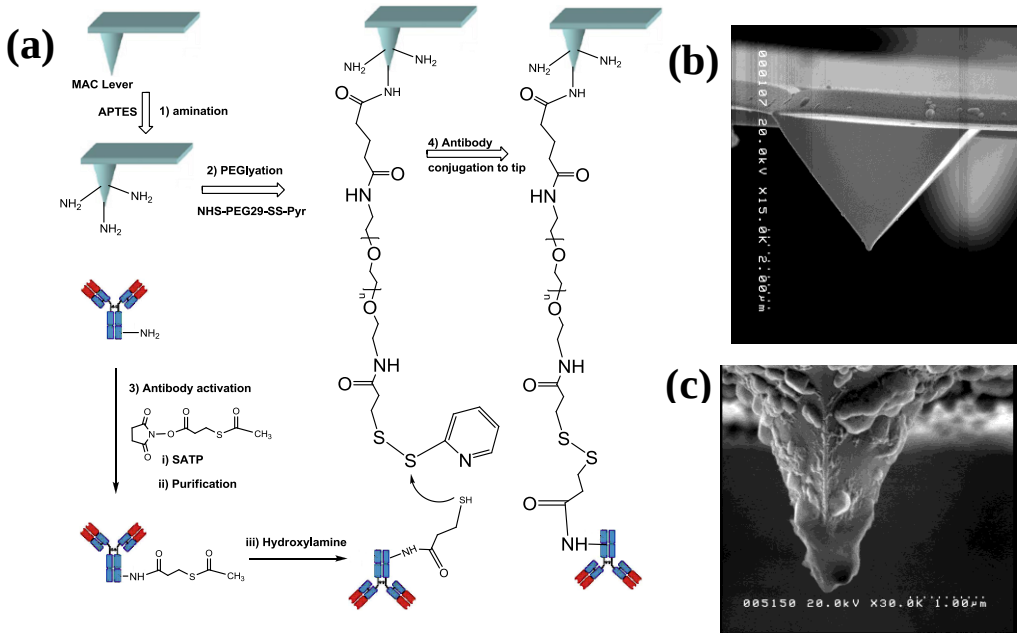


Figure 4.1 (a) Fabrication AFM MAC lever: (1) MAC lever amination; (2) link MAC lever with PEG linker; (3) antibody activation by SATP; (4) SATP-antibody conjugate to AFM tip. (b) SEM image for bare tip. (c) SEM image for anti-EGFR functionalized tip.

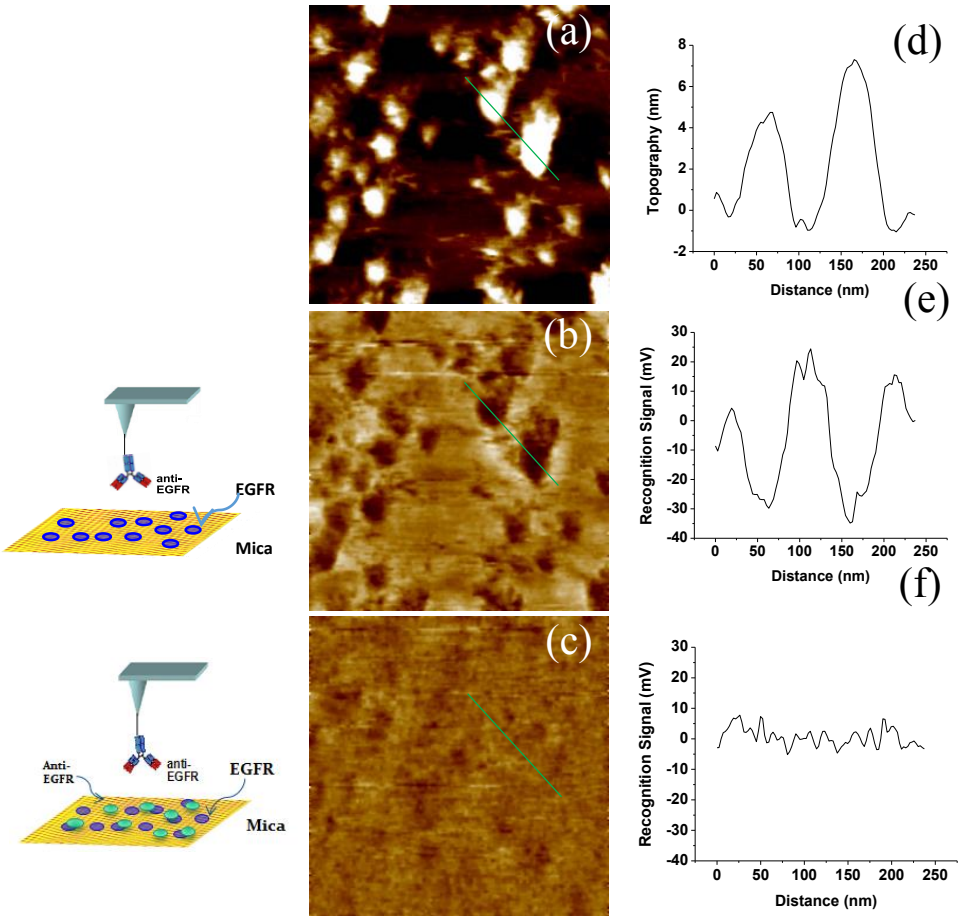


Figure 4.2 Specificity of recognition. (a) Topographic image and (b) corresponding recognition image of EGFR on mica. (c) Recognition image of EGFR after blocking by free anti-EGFR. (d, e, f) Cross section analysis along the green line in (a, b, c). Scan area: 500nm*500nm.

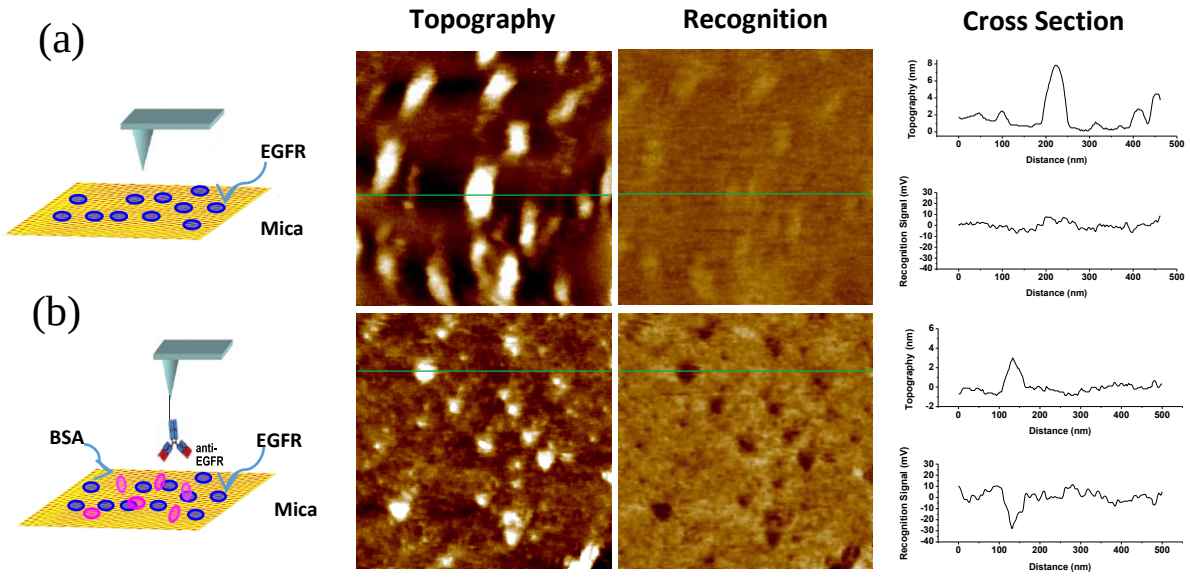


Figure 4.3 Topographic image, corresponding recognition and cross section profile of EGFR on mica under two conditions: (a) bare tip scans on EGFR only; (b) anti-EGFR antibody-tethered tip scans on EGFR with BSA presence. Scan area: 500nm*500nm.

(a) (b)

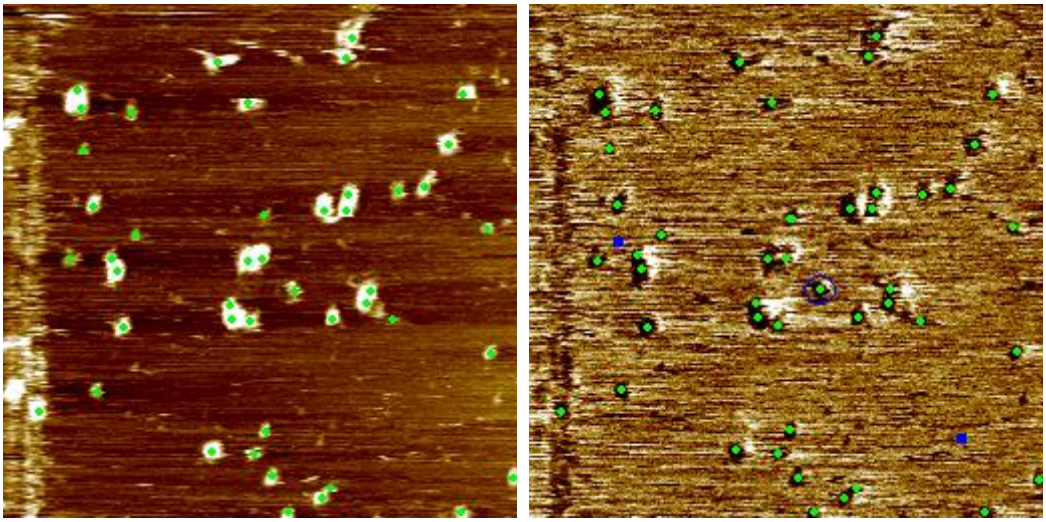


Figure 4.4 Demonstration of recognition events. A pair of green dots in topography (a) and corresponding recognition (b) images represents a recognition event. After rescanning at the same location, changes in recognition events are labeled in the same recognition image (b). Green dot surrounded by a blue circle means a recognition event appear in the first scan but not in the second scan; blue dots represent recognition events appeared in the second scan but not in the first scan. Scan area: 2000nm*2000nm.

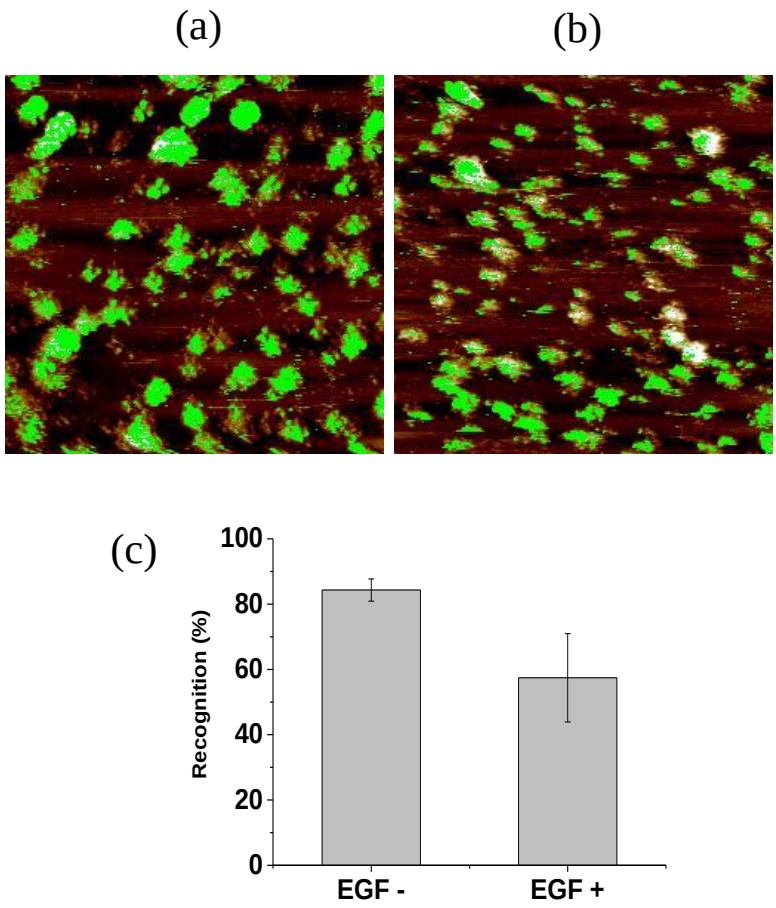


Figure 4.5 EGF influence on the recognition of EGFR on mica. Recognition events of EGFRs (green) superimposed on corresponding topography images before (a) and 10 min after (b) the introduction of EGF solution (20 μg/mL). (c) EGF effect on recognition percentage.

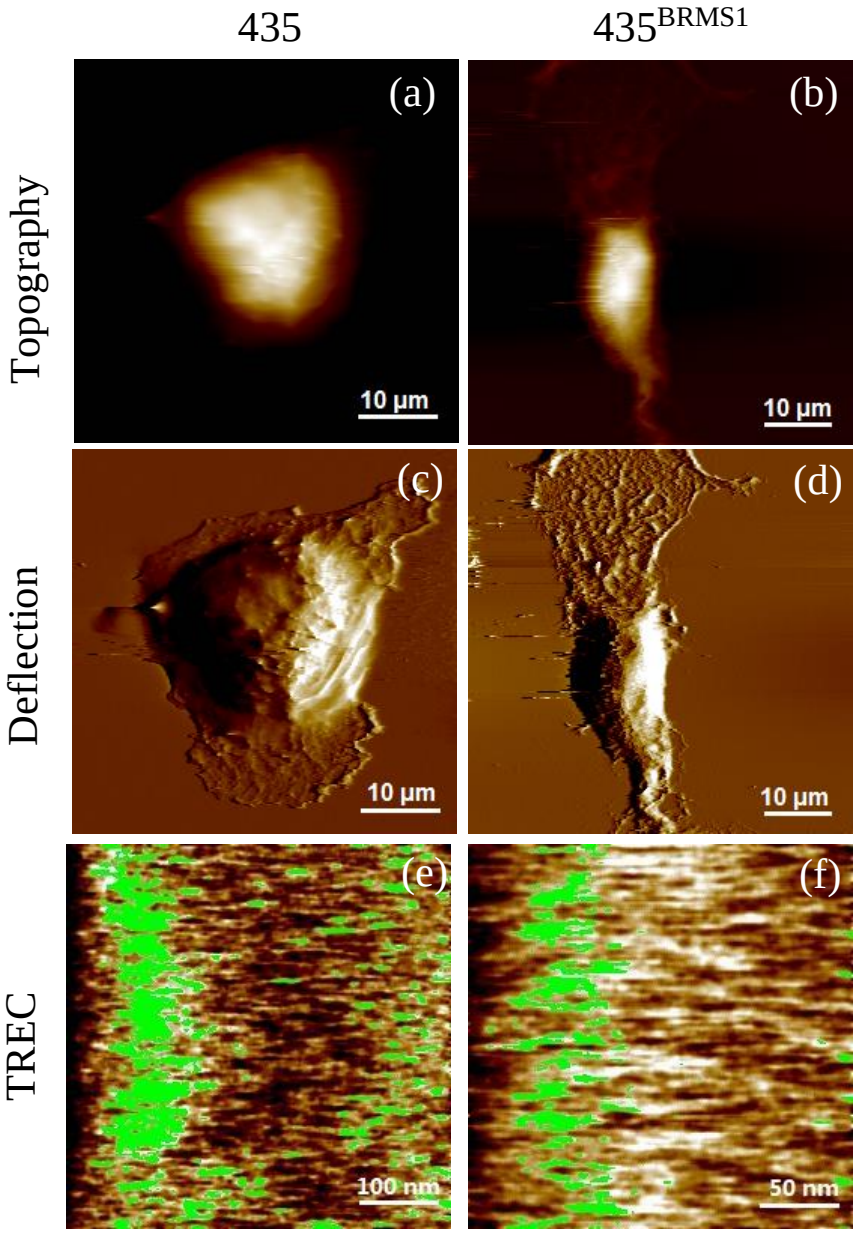


Figure 4.6 Single 435 and 435^{BRMS1} cells' morphologies and their EGFR expression measured by TREC. (a-d) are the topography images (a, b) and corresponding deflection images (c, d) of Single 435 (a, c) and 435^{BRMS1} (b, d) cells. (e, f) are recognition events of EGFRs (green) superimposed onto corresponding topography images of 435 (e) and 435^{BRMS1} cells (f).

(a) (b)

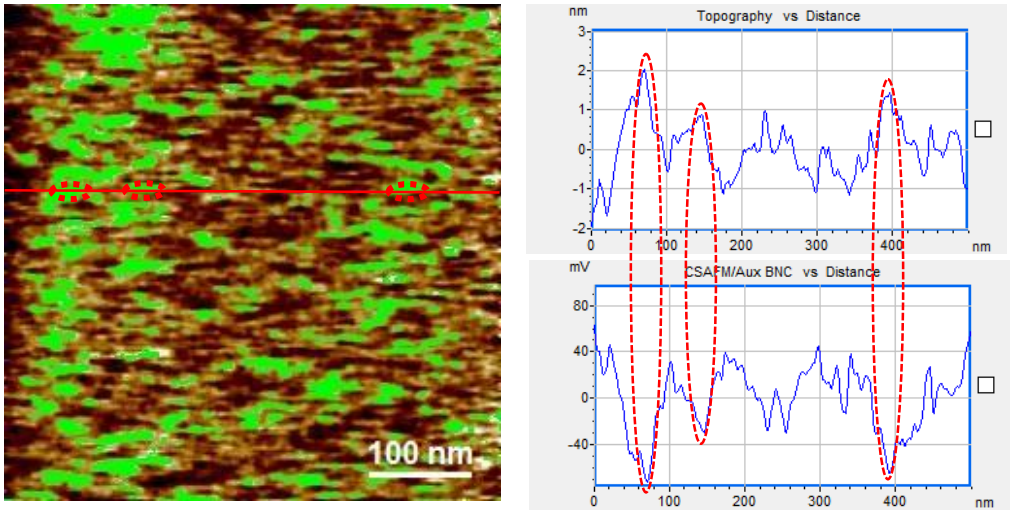


Figure 4.7 (a) Recognition image of EGFRs (green) superimposed on corresponding topography images of 435 cell. (b) Cross section profile along the red line in (a). Corresponding peaks were occurred at the positions of recognition sites, indicating the recognition events.

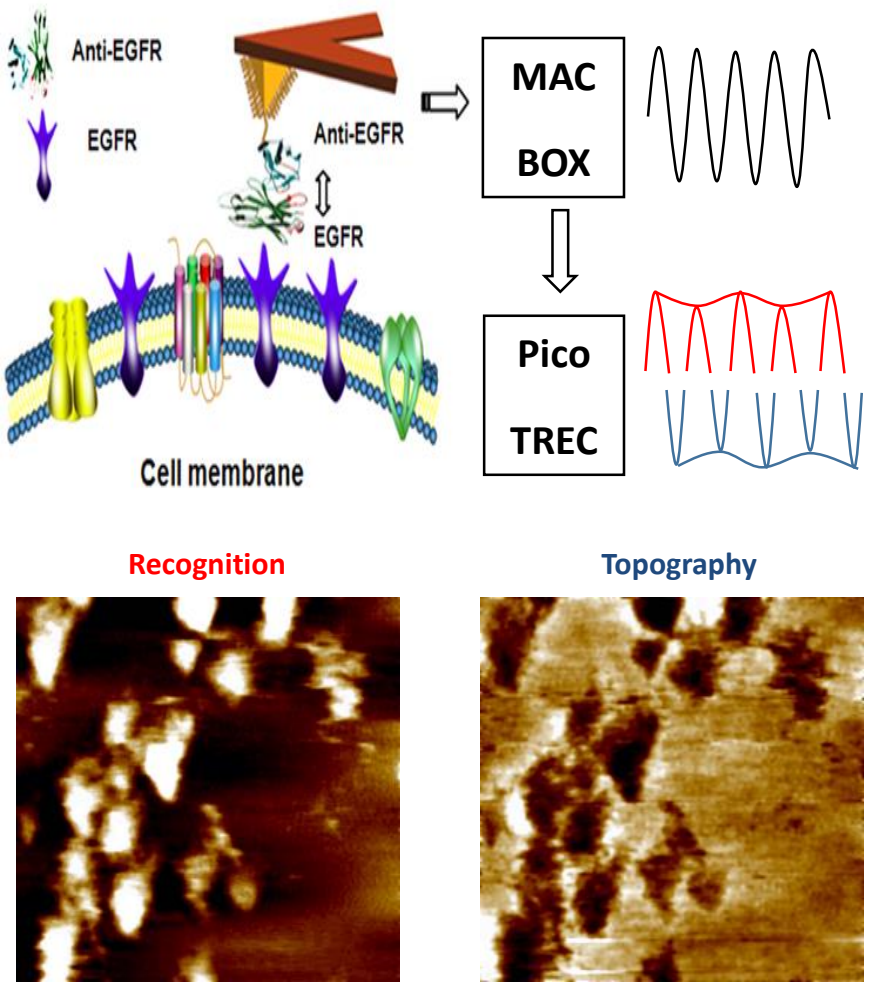


Figure 4.8 Schematic illustration of the TREC imaging method.

CHAPTER 5

Gd_2O_3-DOPED SILICA @ GOLD NANOPARTICLES AS PROBES FOR IN VITRO CANCER BIOMARKER IMAGING USING SURFACE-ENHANCED RAMAN SPECTROSCOPY

5.1 ABSTRACT

Here we report a novel nanomaterial composed of gadolinium oxide-doped silica nanoparticles and gold nanoparticles (Gd-Au NPs), which can be used for detection and imaging of epidermal growth factor receptor (EGFR) on individual human cancer cells with surface-enhanced Raman scattering (SERS). The Gd-Au NPs were sequentially conjugated with a monoclonal antibody recognizing EGFR and a Raman reporter molecule, 4-meraptobenzoic acid (MBA), to generate characteristic SERS signal at 1075 cm^{-1}. By spatially mapping the SERS intensity at 1075 cm^{-1}, cellular distribution of EGFR and relocalization on the plasma membrane were measured. In addition, the EGFR expression level in three human cancer cell lines (S18, A431 and A549) was measured using this SERS probe, which was consistent with the comparable measurements using immunoblotting and immunofluorescence.

5.2 INTRODUCTION

Noninvasive cancer imaging to exhibit tumor anatomical structure and to investigate its metabolism plays an important role in early cancer detection and localization [1]. Currently, there are several imaging modalities widely applied in cancer research, such as magnetic resonance imaging (MRI) [2-5], photoacoustic (PA) imaging [6-8], surface-enhanced Raman scattering (SERS) [9-11] and optical fluorescent imaging [12-15]. Although each individual modality has specific advantages in cancer imaging, none of

them is able to support comprehensive structural and functional studies of tumors independently. Thus, there has been an interest in developing multimodal approaches to combine the advantages of these individual imaging modalities, as well as to compensate for the weaknesses of individual imaging modalities. Recently, several composite nanoparticles have been successfully synthesized and applied to multimodal imaging [16-21]. These composite nanoparticles are usually constructed by combining together nano-components, which are effective contrast agents for different imaging modalities. For example, Gao and co-workers [16] synthesized an iron oxide and gold-coupled core-shell nanoparticles to integrate both MRI and PA imaging, which provided remarkable contrast enhancement in bioimaging. Despite quickly growing interest in designing multifunctional imaging contrast agents, the challenge remains to combine different imaging modalities while preserving the controlled particle size.

Among varied imaging modalities, MRI has the advantages of high spatial and temporal resolution and unlimited tissue penetration, which make it a great technique for clinical diagnostics. But it also suffers the limitation of insufficient sensitivity and it is unable to detect the subcellular distribution of the nanoscale contrast agent in living cancer cells. In recent years, SERS has become an emerging non-invasive imaging tool in detection of cancer cells and cancer biomarkers, due to its ultrahigh sensitivity and the ability to reflect subtle changes in chemical composition and molecular structure of living cells [22-24]. To date, only a few studies have been published integrating MRI and SERS for multimodal bioimaging [17, 18], even though this combination can achieve both high resolution and high sensitivity. We previously reported a gadolinium-doped mesoporous silica nanoparticle (Gd_2O_3@MCM-41) as an efficient MRI contrast agent for cancer

imaging [25, 26]. In addition, we incorporated the gadolinium-doped mesoporous silica nanoparticle and gold nanoparticle (AuNP) into one single nano-system to form a composite Gd-Au nanostructure (Gd_2O_3@MCM-41@Au) [27]. The Gd-Au nanocomposite was an efficient amplification strategy to increase MRI signals for *in vivo* cancer imaging. MRI alone did not show enough sensitivity to study the relocation and endocytosis of surface markers at subcellular level.

Epidermal growth factor receptor (EGFR) is a cell surface receptor tyrosine kinase that, when activated by binding its specific ligands (e.g. EGF, TGF-α), triggers cell signaling pathways that result in cell proliferation, inhibition of apoptosis, angiogenesis, cell migration, adhesion and invasion [28, 29]. EGFR over-expression and up-regulation have been reported in variety of cancers, including breast [30], lung [31], and esophageal [32]. As a result, EGFR is the target in an expanding class of anticancer therapies [31, 33].

Here we report synthesis and characterization of a Gd-Au nanocomposite (Gd_2O_3@MCM-41@Au) functionalization to make it capable of SERS detection, conjugation with a monoclonal antibody (mAb) to target EGFR and validation of function human nasopharyngeal carcinoma (S18), epidermoid carcinoma (A431), and lung adenocarcinoma (A549) cells. Importantly, SERS allowed mapping of EGFR cellular distribution of EGFR on individual cancer cells in real time.

5.3 EXPERIMENTAL METHODS

5.3.1 Materials

4-mercaptobenzoic acid (MBA), 1-ethyl-3-(3-dimethylaminopropyl) carbodiimide hydrochloride (EDC), N-hydroxysuccinimide (NHS), Tris-HCl, ß-glycerol phosphate, EDTA, glycerol, triton X-100, sodium orthovanadate, benzamidine, aprotinin, leupeptin,

phenylmethylsulfonyl fluoride, tween 20, phosphate buffer saline (PBS) and bovine serum albumin (BSA) were purchased from Sigma-Aldrich (St. Louis, MO). All solutions were prepared using deionized water (18 MΩ cm^{-1}). Monoclonal anti-EGFR antibody was purchased from Life Technology (Carlsbad, CA). The polyethylene glycol (PEG) products, Thiol-PEG-COOH and mPEG-Thiol, were purchased from Nanocs Inc. (New York, NY).

5.3.2 Preparation of the Gd-Au nanoprobe

The Gd-Au nanocomposite composed of Gd_2O_3-MCM41 silica nanoparticle and gold (Au) nanoparticle were synthesized as previously described [26, 27]. The synthesized Gd-Au nanocomposite was imaged by high-angle annular dark-field scanning electron microscopy (HAADF-STEM, University of Oregon). The size distribution of the Gd-Au nanocomposite was measured by dynamic light scattering (DynaPro NanoStar, Wyatt Technology, Santa Barbara, CA).

The Gd-Au nanocomposite was sequentially coated with Raman reporter molecule 4-mercaptobenzoic acid (MBA), polyethylene glycol (PEG), and anti-EGFR antibody (Life Technology, AHR5062) to achieve SERS capability, biocompatibility and specific targeting as detailed below. Gd-Au (8.1 mg) was dissolved in phosphate-buffered saline (10 mL) followed by addition of MBA solution (100 µL in 0.03 M in EtOH) before stirring for 30 min. Then Thiol-PEG-COOH (1 mL, 0.24 mM, MW 5000) was introduced to react for 30 min before 2.8 mL of mPEG-Thiol (0.42 mM, MW 5000) was added to stir for another 3 hr. The resulting mixture solution was centrifuged (9700 g, 10 min) twice to remove excess PEG molecules. The conjugation of monoclonal antibody was achieved by using EDC/NHS method [34, 35] to activate the Gd-Au nanoparticle. PEGylated Gd-Au nanocomposite was re-suspended in water. EDC (10 µL, 10 mM) and 10 µL of NHS

solution (25 mM) were added to 1 mL of Gd-Au suspension (0.8 mg/mL) and incubated for 30 min at room temperature. Activated Gd-Au suspension was then incubated with 20 µL of mAb EGFR (0.21 mg/mL) for 1 hr at room temperature. Excess antibody was removed by centrifugation (9700 g, 10 min). The antibody functionalized Gd-Au bioprobes were stored at 4 °C before measurements. The nanoparticles were stable for several days.

5.3.3 Cell culture, viability and sample preparation

All cells were purchased from ATCC and were determined to be free of *Mycoplasma* contamination. Cells were grown at 37°C with 5% CO_2 in a humidified atmosphere. The human epidermoid carcinoma cell line A431 was cultured in Dulbecco's-modified eagle's medium (DMEM) and Ham's F-12 medium (1:1) with 10% fetal bovine serum (FBS). The human lung carcinoma cell line A549 was cultured in F-12k medium with 5% FBS and 1% penicillin-streptomycin. The human nasopharyngeal carcinoma cell line S18 was cultured in DMEM with 10% FBS.

Cells were passaged at 80-90% confluence and seeded at a density of 10^5 cells per 2 mL of media. Cells were let grow for 24 hr after seeding before imaging measurements. For Raman measurements, cells were seeded on magnesium fluoride (MgF_2) substrates to minimize the background noise. Cells were seeded on glass bottom Petri dishes for other optical imaging measurements.

The cell viability was analyzed using LIVE/DEAD Viability/Cytotoxicity Assay Kit (Invitrogen) according to manufacturer's instructions.

5.3.4 Cellular SERS measurements

Raman measurements were performed by a Renishaw inVia Raman system (Renishaw, UK) coupled with a Leica DMLM microscope (Leica microsystems, USA)

equipped with a 785 nm near-IR laser. A 63X water immersion objective (NA = 0/90) was used to image the cells in culture media and a temperature control unit (ALA Scientific Instruments, USA) was used to keep cells under physiological temperature (37.5 °C). The Raman instrument was calibrated with silicon at 520.5 cm^{-1}.

Prior to Raman measurements, all three cell lines (A431, A549 and S18) were incubated with anti-EGFR-conjugated Gd-Au nanoprobes for 1 hr and rinsed with PBS to remove unbounded nanoparticles. Raman spectra (600~1800 cm^{-1}) and Raman streamline mapping (at 1075 cm^{-1}) of the nanoprobe-treated cells were recorded under a laser intensity of 3 mW. Spectra smoothing, baseline subtraction and mapping generation were performed by Renishaw WiRE 3.3 software. Processed data were exported to Origin Pro 9 software (OriginLab Corp., USA) for statistical analysis.

5.3.5 Cellular optical imaging

Fluorescence images of the nanoprobe-treated cells were collected by an Olympus IX71 inverted fluorescence microscope equipped with an Olympus DP30BW CCD camera. Dark field images were obtained by using an oil-immersed dark field condenser (NA=1.5). Images were acquired with 40x objectives using DPController software (Olympus).

5.3.6 Western blot

Cells were rinsed twice with ice-cold PBS and lysed in a buffer containing 25 mM Tris-HCl (pH 7.4), ß-glycerol phosphate (50 mM), EDTA (0.5 mM), glycerol (5%), triton X-100 (0.1%), sodium orthovanadate (1 mM), benzamidine (1 mM), and a protease inhibitor cocktail containing aprotinin, leupeptin, and phenylmethylsulfonyl fluoride. Protein concentration was determined using a BCA assay (Pierce, Rockford, IL). Protein

was denatured with Laemmli's buffer at 95°C for 5 min and lysate (50 μg) was loaded to each well. Proteins were separated using 10% SDS-PAGE gel electrophoresis and resolved proteins were transferred to PVDF before incubating in Tris-buffered saline containing Tween-20 (0.05%) and fat-free dry milk (5%) for 1 hr at room temperature. Membranes were incubated with primary antibodies to EGFR and β-Actin overnight at 4°C and subsequently with HRP-conjugated secondary antibody at room temperature for 1 hr. Signals were visualized using ECL (Pierce, Rockford, IL) following manufacturer's instructions.

5.3.7 Immunofluorescence imaging

S18, A431 and A549 cells grown on coverslips for 24 hr were fixed using 4% paraformaldehyde for 20 min and permeabilized using 0.1% trion X-100 for 10 min. After blocking with 5% BSA in PBS, cells were incubated with anti-EGFR antibody conjugated with Alexia Fluor 555 at 1:50 dilution in 5% BSA solution overnight at 4°C. After washing the cells thrice with PBS, the cover slips were mounted using Vectashield mounting solution containing the nuclear counter-stain 4', 6-diamidino-2-phenylindole (DAPI). Images were collected under a Nikon inverted epifluorescence microscope. Representative images were combined and processed using ImageJ software.

5.4 RESULTS AND DISCUSSION

5.4.1 Characterization of the Gd-Au nanocomposite

The synthesized Gd-Au nanoparticle has a composite structure illustrated in Figure 5.1a. Gadolinium oxide (Gd_2O_3) nanoparticles were embedded in the mesoporous silica structure (MCM-41). Gd_2O_3-MCM41 is conjugated with gold (Au) nanoparticles through a polymer linker polyethylenimine (PEI). The structure of the Gd-Au nanocomposite can

be visualized by HAADF-STEM imaging (Figure 5.1b). Energy dispersive X-ray (EDX) spectrum (supporting information, Figure 5.2a) and the elemental mapping (Figure 5.1c) have presented the existence of gadolinium and gold, indicating the successful assembly of the core-shell like structure of the Gd-Au nanocomposite. A line profile of integrated intensity plot shows the elemental distribution across the nanocompostie (Figure 5.2b). The hydraulic diameter is measured to be 208.05 ± 5.98 nm using dynamic light scattering (DLS) (Figure 5.1d).

5.4.2 Functionalization of the Gd-Au nanocomposite

To make the Gd-Au nanocomposite a specific SERS probe for EGFR sensing and imaging, step-by-step fucntionalization was conducted. As presented in Figure 5.3a, Gd-Au nanoparticles were firstly conjugated with 4-mercaptobenzoic acid (MBA) through Au-S covalent bond as a Raman reporter molecule. The reasons to use MBA were: (1) MBA can produce high SERS effect when binding with gold nanoparticle due to its high binding affinity with gold and relatively large cross section area for Raman scattering [36]; (2) MBA has simple SERS spectrum in the fingerprint region (600~1800 cm^{-1}) with two intensive characteristic peaks at 1075 and 1587 cm^{-1}. The presence of both characteristic peaks on spectra of nanoparticle-treated S18 cells (Figure 5.3b) confirmed the successful adsorption of MBA on the Gd-Au nanocomposite. Then, thiolated PEG linkers were also coated onto Au surfaces (PEG-NP) to eliminate the non-specific particle-cell binding as well as to improve the biocompatibility of the Gd-Au nanoprobes when incubated with cells *in vitro*. Lastly, to realize specific EGFR targeting, monoclonal antibody to EGFR was introduced and conjugated with the PEGylated Gd-Au nanocomposite using EDC/NHS method. The antibody-targeted Gd-Au nanoprobe (mAb-NP) was then used for

in vitro SERS detection of EGFR and SERS imaging of cellular EGFR distribution at single cell level.

5.4.3 Specificity of EGFR targeting

In order to study how anti-EGFR functionalized Gd-Au nanoprobes specifically bind to EGFR and are subsequently internalized via receptor-mediated endocytosis, control experiments are performed under different conditions. S18 cells (EGFR-positive)were incubated with Gd-Au nanoprobes under three conditions: (1) PEG-NP for 1 hr; (2) mAb-NP for 1 hr; and, (3) pre-blocked with free anti-EGFR antibody for 1 hr, followed by incubation with mAb-NP for 1 hr. Cells were rinsed with PBS thrice to remove unbound nanoprobes, before Raman measurements.

Typical Raman spectra are shown in Figure 5.3b. Cells with PEG-NP incubation typically present a much lower SERS signal compared to cells incubated with mAb-NP, while cells in the pre-block group (block-mAb-NP) show almost non-observable SERS spectra (Figure 5.3c). Moreover, as shown in Figure 5.3c, the average intensities at 1075 cm^{-1} calculated from 50 spectra (1 cell/spectra) for each condition confirm the same finding. S18 cells alone (CTRL) or treated with PEG-NP or mAb-NP were also visualized using dark field imaging (Figure 5.3d). PEG-NP–treated cells exhibit minimal light scattering, similar to CTRL, while cells incubated with mAb-NP have many more bright spots, indicative of nanoparticles binding to the cells.

Thus, both SERS and dark field imaging indicate that the Gd-Au nanoprobes bind to the S18 cells through a selective antibody-antigen recognition. Nonspecific binding was minimal (i.e., few PEG-NP particles and low SERS signal) and selective (i.e., significant suppression when pre-blocked with free anti-EGFR). High SERS signal was only observed

in cells incubated with mAb-NP, indicating that the Gd-Au nanoprobe is capable of specific SERS detection of EGFR.

5.4.4 Biocompatibility of the Gd-Au nanoprobe

To investigate the biocompatibility of the Gd-Au nanoprobe, viability of S18 cells was measured following incubation with mAb-NPs at different concentrations (8, 20, 28, 40 and 48 μg/ml) for 24 hr. As shown in Figure 5.4, the cell viability remains >90% even at the highest concentrations. For further SERS detection studies, a dose of 40 μg/ml was chosen.

5.4.5 SERS mapping of cellular EGFR distribution

Raman mapping is generated by firstly taking spectral acquisition (2s exposure) centered at 1100 cm^{-1} (400 cm^{-1} bandwidth) at each point over the 2D area of a single cell with 0.8 μm spacing. Then, color mapping with the peak intensity at 1075 cm^{-1} is plotted to depict the intensity variation over the area, which reflects the cellular EGFR distribution via the binding of Gd-Au nanoprobes.

Changes of cellular EGFR distribution were measured (Figure 5.5). A single S18 cell after 1 hr incubation with mAb-NPs is presented in the Raman bright field image (Figure 5.5a). *In situ* Raman mapping is performed over the area of cell body (dotted area in Figure 5.5a) at 60, 90 and 120 min. As shown in Figure 5.5b-d, the bright spots, which represent EGFR molecules, are heterogeneously distributed and are relocating in the cell. Figure 5.5e-g show the Raman spectra at the same position (green crosses) in the mappings at different times (Figure 5.5b-d). The time-dependent changes indicates the reorganization of cell membrane after nanoparticle binding. The membrane reorganization is most likely due to internalization of nanoprobes after binding through a receptor-mediated endocytosis,

as suggested by a decreased mapping intensity with longer incubation (Figure 5.6). The results of *in situ* Raman mapping have demonstrated the feasibility of the methodology to detect and monitor dynamic cellular processes, although the mechanisms underlying the cellular relocalization will require additional studies.

5.4.6 EGFR detection in three human cancer cell lines (S18, A431 and A549)

The proof-of-concept studies with S18 were validated using two unrelated human cancer cell lines. As shown in Figure 5.7, SERS mapping shows EGFR in discrete domains on each cell, but at different intensities, suggesting that the EGFR expression varies between the cell lines.

To verify the EGFR levels, average Raman peak intensity at 1075 cm^{-1} was calculated using data from 50 cells (1 spectrum/cell) in each cell line. A431 cell had significantly (**P<0.01, one-way ANOVA) higher EGFR level than S18 or A549 cells (Figure 5.8a). These observations were consistent with the western blot (i.e., EGFR band is darker in A431 than S18 and A549, Figure 5.8b) and immunofluorescence imaging (Figure 5.9). Importantly, SERS has the advantage over immunofluorescence because there is no photo-bleaching. Since SERS has narrower spectral bands than fluorescence, it represents a better candidate for multiplex imaging in complex biosystems.

5.5 CONCLUSION

In conclusion, we have synthesized a gadolinium-gold composite nanoparticle and functionalized this nanoparticle for specific in vitro detection and imaging of EGFR using surface-enhanced Raman scattering. Applying this Gd-Au nanoprobe, EGFR expression level and cellular distribution were detected by SERS, and confirmed with immunoblotting and immunofluorescence imaging. SERS shows the advantage of non-invasive detection

over immunoblotting and immunofluorescence. In addition, changes in single cell EGFR distribution could be monitored in situ, demonstrating the potential of SERS to study cell activity under physiological conditions. These SERS results, combined with previously reported MRI results [27], demonstrate the potential of this Gd-Au composite nanoparticle as a multifunctional nanoprobe not only for the early detection and localization of cancer in vivo, but also for the investigation of cancer metabolism and biochemistry at single cell level.

5.6 REFERENCES

[1] J.S. Xu, J.W. Huang, R.G. Qin, G.H. Hinkle, S.P. Povoski, E.W. Martin, R.X. Xu, Synthesizing and binding dual-mode poly (lactic-co-glycolic acid) (PLGA) nanobubbles for cancer targeting and imaging, Biomaterials 31 (2010) 1716-1722.

[2] K. El-Boubbou, D.C. Zhu, C. Vasileiou, B. Borhan, D. Prosperi, W. Li, X.F. Huang, Magnetic glyco-nanoparticles: a tool to detect, differentiate, and unlock the glyco-codes of cancer via magnetic resonance imaging, J. Am. Chem. Soc. 132 (2010) 4490-4499.

[3] Y. Chen, H.R. Chen, D.P. Zeng, Y.B. Tian, F. Chen, J.W. Feng, J.L. Shi, Core/shell structured hollow mesoporous nanocapsules: a potential platform for simultaneous cell imaging and anticancer drug delivery, ACS Nano 4 (2010) 6001-6013.

[4] M.G. Harisinghani, J. Barentsz, P.F. Hahn, W.M. Deserno, S. Tabatabaei, C.H. van de Kaa, J. de la Rosette, R. Weissleder, Noninvasive detection of clinically occult lymph-node metastases in prostate cancer, New Engl. J. Med. 348 (2003) 2491-2499.

[5] J.H. Lee, Y.M. Huh, Y. Jun, J. Seo, J. Jang, H.T. Song, S. Kim, E.J. Cho, H.G. Yoon, J.S. Suh, J. Cheon, Artificially engineered magnetic nanoparticles for ultra-sensitive molecular imaging, Nat. Med. 13 (2007) 95-99.

[6] E.I. Galanzha, E.V. Shashkov, T. Kelly, J.W. Kim, L.L. Yang, V.P. Zharov, In vivo magnetic enrichment and multiplex photoacoustic detection of circulating tumour cells, Nat. Nanotechnol. 4 (2009) 855-860.

[7] S.A. Ermilov, T. Khamapirad, A. Conjusteau, M.H. Leonard, R. Lacewell, K. Mehta, T. Miller, A.A. Oraevsky, Laser optoacoustic imaging system for detection of breast cancer, J. Biomed. Opt. 14 (2009) 024007.

[8] S. Manohar, S.E. Vaartjes, J.C.G. van Hespen, J.M. Klaase, F.M. van den Engh, W. Steenbergen, T.G. van Leeuwen, Initial results of in vivo non-invasive cancer imaging in the human breast using near-infrared photoacoustics, Opt. Express 15 (2007) 12277-12285.

[9] S. Keren, C. Zavaleta, Z. Cheng, A. de la Zerda, O. Gheysens, S.S. Gambhir, Noninvasive molecular imaging of small living subjects using Raman spectroscopy, Proc. Natl. Acad. Sci. USA 105 (2008) 5844-5849.

[10] A. Samanta, K.K. Maiti, K.S. Soh, X. Liao, M. Vendrell, U.S. Dinish, S.W. Yun, R. Bhuvaneswari, H. Kim, S. Rautela, J. Chung, M. Olivo, Y.T. Chang, Ultrasensitive near-infrared Raman reporters for SERS-based in vivo cancer detection, Angew Chem. Int. Ed. Engl. 50 (2011) 6089-6092.

[11] L. Xiao, S. Harihar, D.R. Welch, A. Zhou, Imaging of epidermal growth factor receptor on single breast cancer cells using surface-enhanced Raman spectroscopy, Anal. Chim. Acta 843 (2014) 73-82.

[12] A. Becker, C. Hessenius, K. Licha, B. Ebert, U. Sukowski, W. Semmler, B. Wiedenmann, C. Grotzinger, Receptor-targeted optical imaging of tumors with near-infrared fluorescent ligands, Nat. Biotechnol. 19 (2001) 327-331.

[13] M. Wang, C.C. Mi, W.X. Wang, C.H. Liu, Y.F. Wu, Z.R. Xu, C.B. Mao, S.K. Xu, Immunolabeling and NIR-excited fluorescent imaging of HeLa cells by using $NaYF_4$:Yb,Er upconversion nanoparticles, ACS Nano 3 (2009) 1580-1586.

[14] Y. Urano, D. Asanuma, Y. Hama, Y. Koyama, T. Barrett, M. Kamiya, T. Nagano, T. Watanabe, A. Hasegawa, P.L. Choyke, H. Kobayashi, Selective molecular imaging of viable cancer cells with pH-activatable fluorescence probes, Nat. Med. 15 (2009) 104-109.

[15] M. Yang, E. Baranov, P. Jiang, F.X. Sun, X.M. Li, L.N. Li, S. Hasegawa, M. Bouvet, M. Al-Tuwaijri, T. Chishima, H. Shimada, A.R. Moossa, S. Penman, R.M. Hoffman, Whole-body optical imaging of green fluorescent protein-expressing tumors and metastases, Proc. Natl. Acad. Sci. USA 97 (2000) 1206-1211.

[16] Y.D. Jin, C.X. Jia, S.W. Huang, M. O'Donnell, X.H. Gao, Multifunctional nanoparticles as coupled contrast agents, Nat. Commun. 1 (2010) 41.

[17] M.F. Kircher, A. de la Zerda, J.V. Jokerst, C.L. Zavaleta, P.J. Kempen, E. Mittra, K. Pitter, R.M. Huang, C. Campos, F. Habte, R. Sinclair, C.W. Brennan, I.K. Mellinghoff, E.C. Holland, S.S. Gambhir, A brain tumor molecular imaging strategy using a new triple-modality MRI-photoacoustic-Raman nanoparticle, Nat. Med. 18 (2012) 829-834.

[18] M.V. Yigit, L.Y. Zhu, M.A. Ifediba, Y. Zhang, K. Carr, A. Moore, Z. Medarova, Noninvasive MRI-SERS imaging in living mice using an innately bimodal nanomaterial, ACS Nano 5 (2011) 1056-1066.

[19] T. Zhou, B.Y. Wu, D. Xing, Bio-modified Fe_3O_4 core/Au shell nanoparticles for targeting and multimodal imaging of cancer cells, J. Mater. Chem. 22 (2012) 470-477.

[20] X. Niu, H. Chen, Y. Wang, W. Wang, X. Sun, L. Chen, Upconversion fluorescence-SERS dual-mode tags for cellular and in vivo imaging, ACS Appl. Mater. Inter. 6 (2014) 5152-5160.

[21] M. Kacenka, O. Kaman, J. Kotek, L. Falteisek, J. Cerny, D. Jirak, V. Herynek, K. Zacharovova, Z. Berkova, P. Jendelova, J. Kupcik, E. Pollert, P. Veverka, I. Lukes, Dual imaging probes for magnetic resonance imaging and fluorescence microscopy based on perovskite manganite nanoparticles, J. Mater. Chem. 21 (2011) 157-164.

[22] Y.Q. Wang, B. Yan, L.X. Chen, SERS tags: novel optical nanoprobes for bioanalysis, Chem. Rev. 113 (2013) 1391-1428.

[23] J. Ando, K. Fujita, N.I. Smith, S. Kawata, Dynamic SERS imaging of cellular transport pathways with endocytosed gold nanoparticles, Nano Lett. 11 (2011) 5344-5348.

[24] Y.L. Wang, J.L. Seebald, D.P. Szeto, J. Irudayaraj, Biocompatibility and biodistribution of surface-enhanced Raman scattering nanoprobes in zebrafish embryos: in vivo and multiplex imaging, ACS Nano 4 (2010) 4039-4053.

[25] S.A. Li, H.A. Liu, L. Li, N.Q. Luo, R.H. Cao, D.H. Chen, Y.Z. Shao, Mesoporous silica nanoparticles encapsulating Gd_2O_3 as a highly efficient magnetic resonance imaging contrast agent, Appl. Phys. Lett. 98 (2011) 093704.

[26] Y.Z. Shao, X.M. Tian, W.Y. Hu, Y.Y. Zhang, H. Liu, H.Q. He, Y.Y. Shen, F.K. Xie, L. Li, The properties of Gd2O3-assembled silica nanocomposite targeted nanoprobes and their application in MRI, Biomaterials 33 (2012) 6438-6446.

[27] X.M. Tian, Y.Z. Shao, H.Q. He, H. Liu, Y.Y. Shen, W.L. Huang, L. Li, Nanoamplifiers synthesized from gadolinium and gold nanocomposites for magnetic resonance imaging, Nanoscale 5 (2013) 3322-3329.

[28] Y. Wan, D. Tamuly, P.B. Allen, Y.T. Kim, R. Bachoo, A.D. Ellington, S.M. Iqbal, Proliferation and migration of tumor cells in tapered channels, Biomed. Microdevices 15 (2013) 635-643.

[29] C.D. Andl, T. Mizushima, H. Nakagawa, K. Oyama, H. Harada, K. Chruma, M. Herlyn, A.K. Rustgi, Epidermal growth factor receptor mediates increased cell proliferation, migration, and aggregation in esophageal Keratinocytes in vitro and in vivo, J. Biol. Chem. 278 (2003) 1824-1830.

[30] R. Bhargava, W.L. Gerald, A.R. Li, Q.L. Pan, P. Lal, M. Ladanyi, B.Y. Chen, EGFR gene amplification in breast cancer: correlation with epidermal growth factor receptor mRNA and protein expression and HER-2 status and absence of EGFR-activating mutations, Modern Pathol. 18 (2005) 1027-1033.

[31] J.G. Paez, P.A. Janne, J.C. Lee, S. Tracy, H. Greulich, S. Gabriel, P. Herman, F.J. Kaye, N. Lindeman, T.J. Boggon, K. Naoki, H. Sasaki, Y. Fujii, M.J. Eck, W.R. Sellers, B.E. Johnson, M. Meyerson, EGFR mutations in lung cancer: correlation with clinical response to gefitinib therapy, Science 304 (2004) 1497-1500.

[32] Y. Itakura, H. Sasano, C. Shiga, Y. Furukawa, K. Shiga, S. Mori, H. Nagura, Epidermal growth factor receptor overexpression in esophageal carcinoma-an immunohistochemical study correlated with clinicopathological findings and DNA amplification, Cancer 74 (1994) 795-804.

[33] H. Zhang, A. Berezov, Q. Wang, G. Zhang, J. Drebin, R. Murali, M.I. Greene, ErbB receptors: from oncogenes to targeted cancer therapies, J. Clin. Invest. 117 (2007) 2051-2058.

[34] S.P. Wang, N. Mamedova, N.A. Kotov, W. Chen, J. Studer, Antigen/antibody immunocomplex from CdTe nanoparticle bioconjugates, Nano Lett. 2 (2002) 817-822.

[35] B. Johnsson, S. Lofas, G. Lindquist, A. Edstrom, R.M. Muller Hillgren, A. Hansson, Comparison of methods for immobilization to carboxymethyl dextran sensor surfaces by analysis of the specific activity of monoclonal antibodies, J. Mol. Recognit. 8 (1995) 125-131.

[36] A. Michota, J. Bukowska, Surface-enhanced Raman scattering (SERS) of 4-mercaptobenzoic acid on silver and gold substrates, J. Raman Spectrosc. 34 (2003) 21-25.

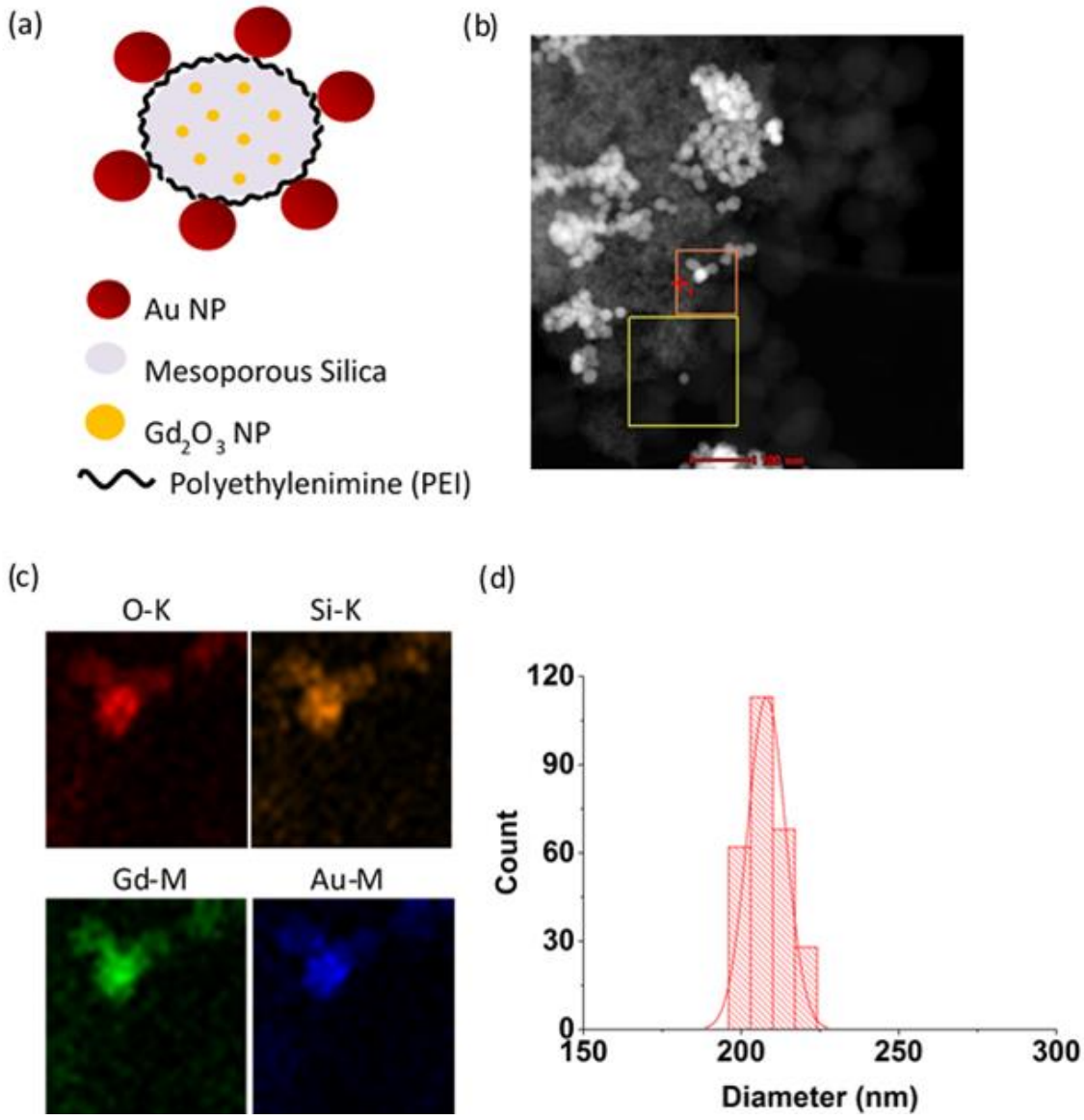
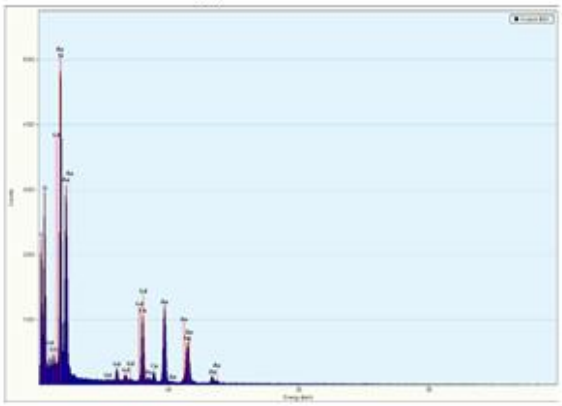


Figure 5.1 (a) Schematic illustration of the Gd-Au nanocomposite. (b) HAADF-STEM image of the Gd-Au nanocomposite. (c) EDX elemental mapping of oxygen (O), silicon (Si), gadolinium (Gd) and gold (Au) within the area labeled with an orange square in (b). (d) Hydraulic diameter of the nanocomposite determined by DLS.

(a)



(b)

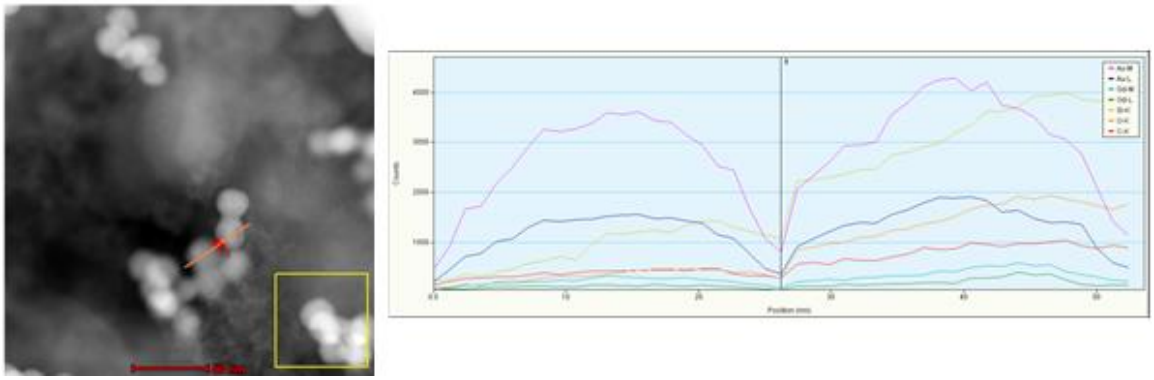


Figure 5.2 (a) Parallel beam EDX spectrum of Gd-Au nanocomposite. (b) STEM image and corresponding elemental line profile of the Gd-Au nanocomposite.

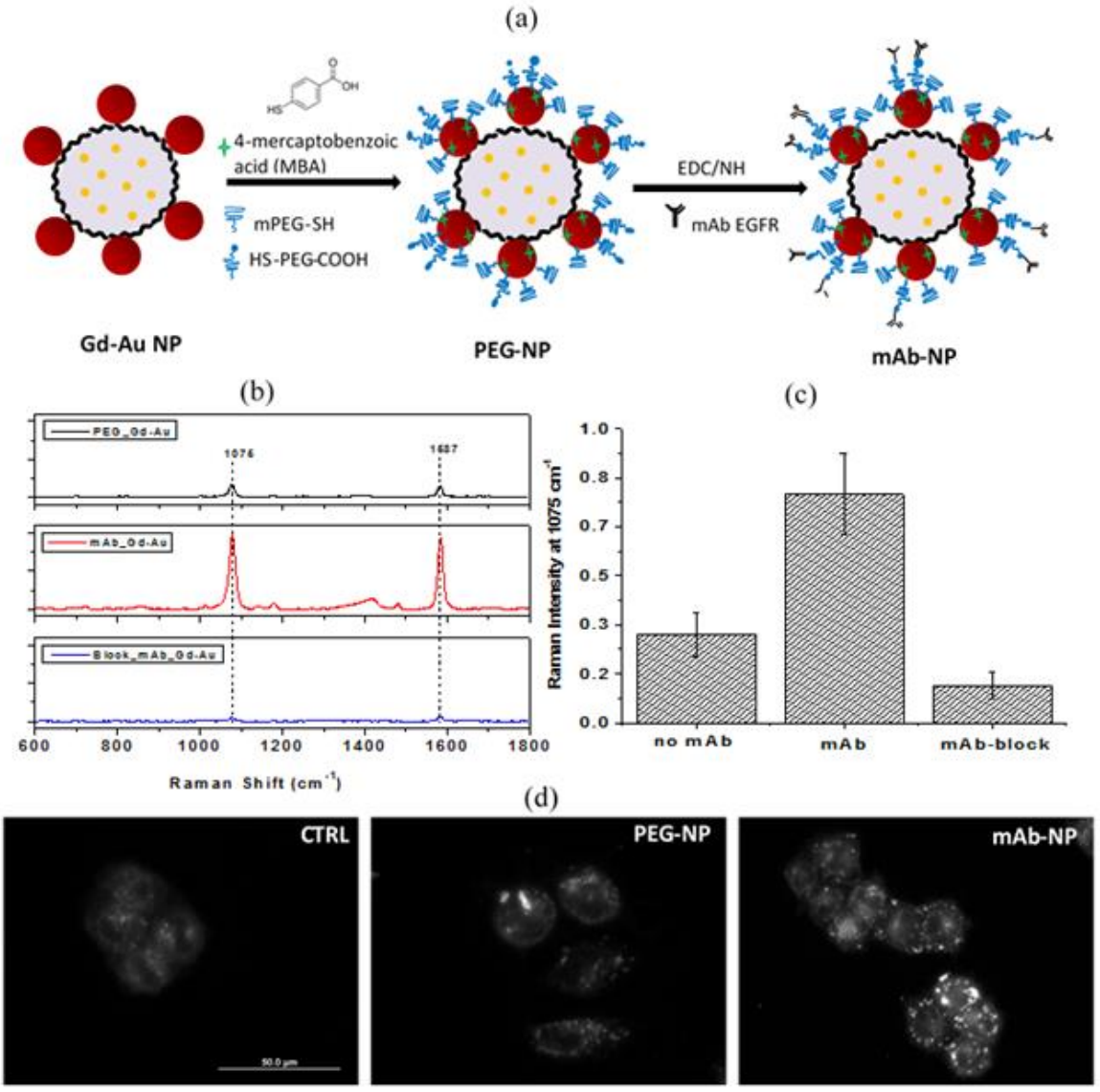


Figure 5.3 (a) Schematic of the functionalization of Gd-Au nanocomposite. (b) Typical Raman spectra (600~1800 cm^{-1}) and (c) average Raman intensity at 1075 cm^{-1} of S18 cells under the treatments of PEG-NP, mAb-NP, and first free anti-EGFR molecules then mAb-NP. Error bar represents standard error of mean (SEM). (d) Dark field images of S18 cells alone (CTRL), cells incubated with PEG-NP, and cells incubated with mAb-NP.

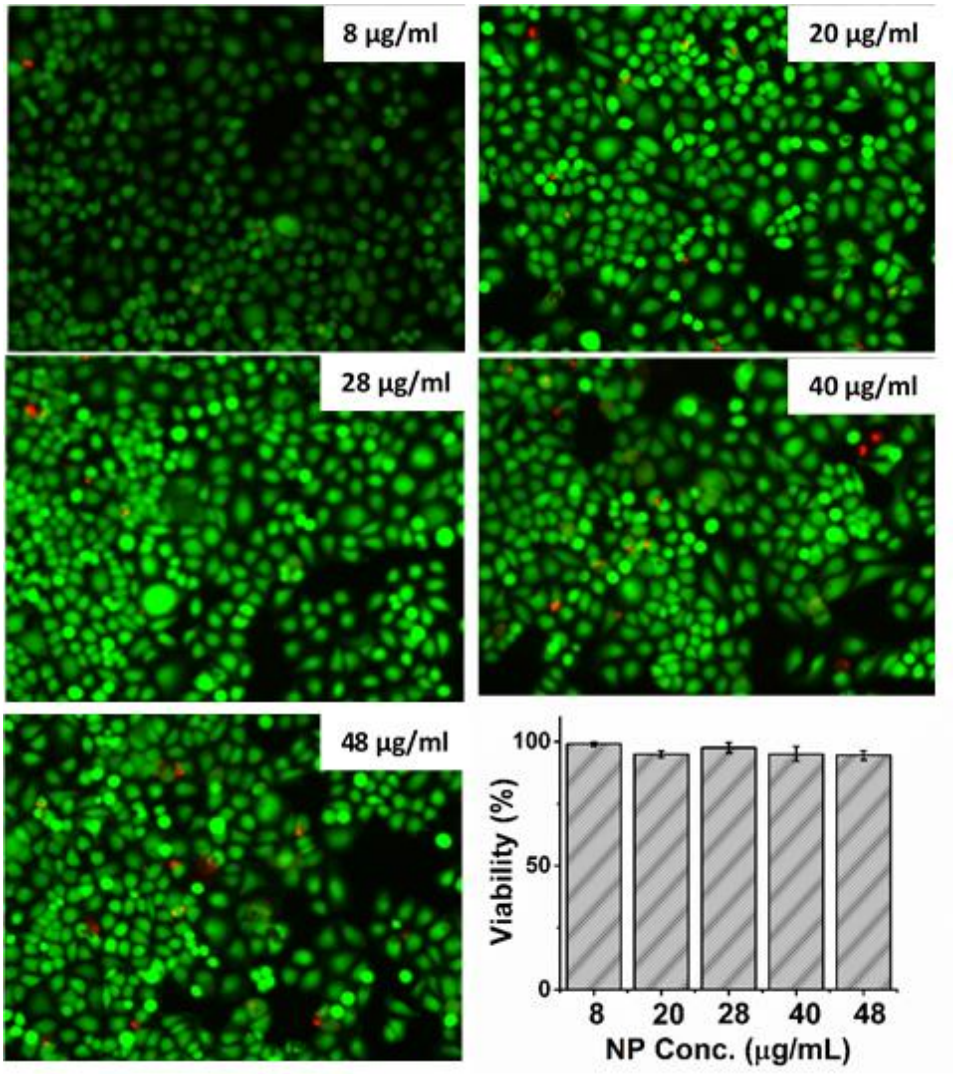


Figure 5.4 Live/dead fluorescent images of S18 cells with mAb-NP incubation at concentrations of 8, 20, 28, 40 and 48 μg/ml. Cell viability is analyzed in the column graph.

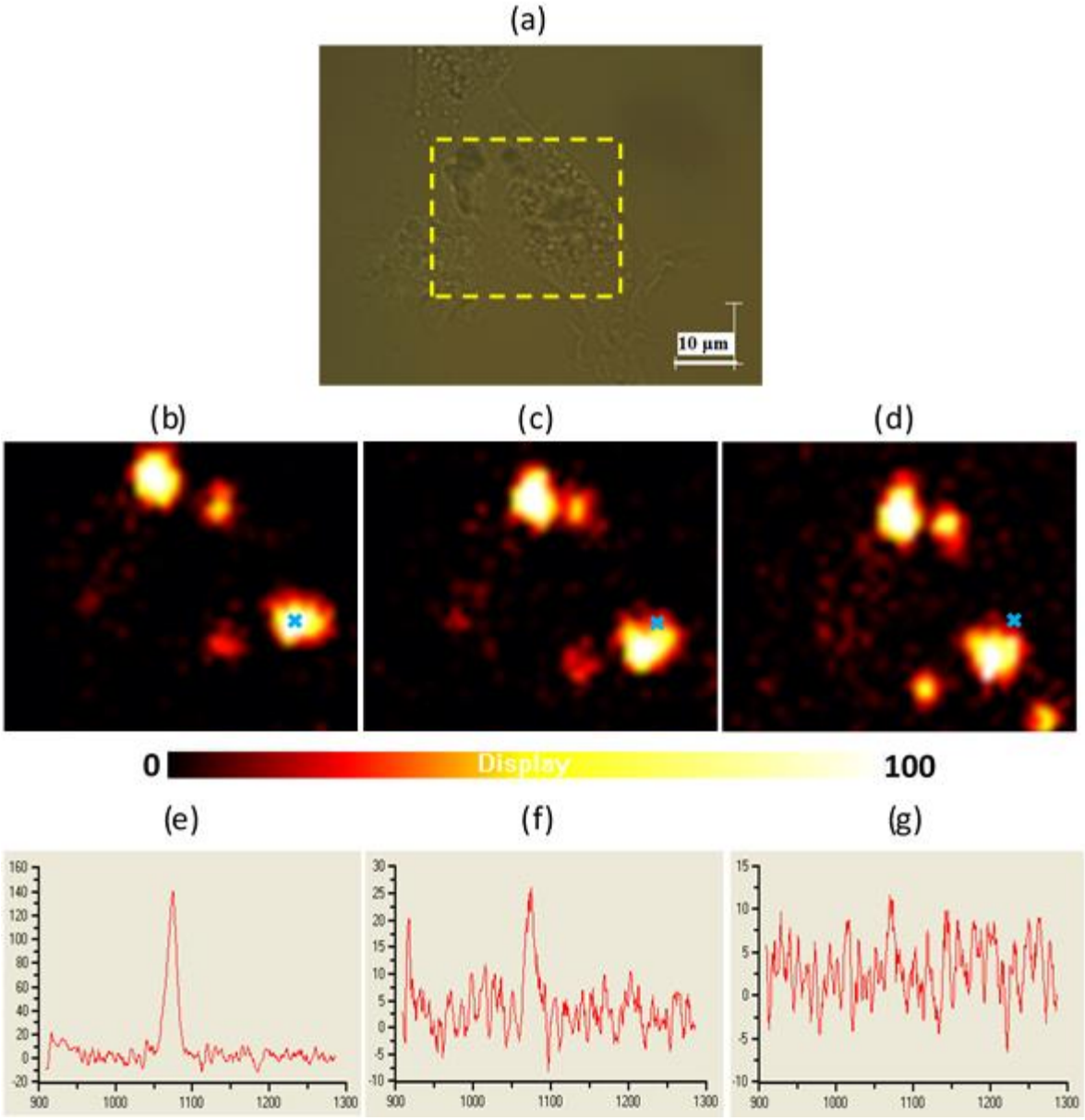


Figure 5.5 (a) Bright field image of a single S18 cell with 1-h incubation with mAb-NP and the selected area for Raman mapping. Scale bar: 10 µm. (b-d) Raman images of the selected area after 60, 90 and 120 min incubation, respectively. The color scale is generated using peak intensity at 1075 cm^{-1}. (e-g) Extracted Raman spectra at the same position (green crosses) in (b-d).

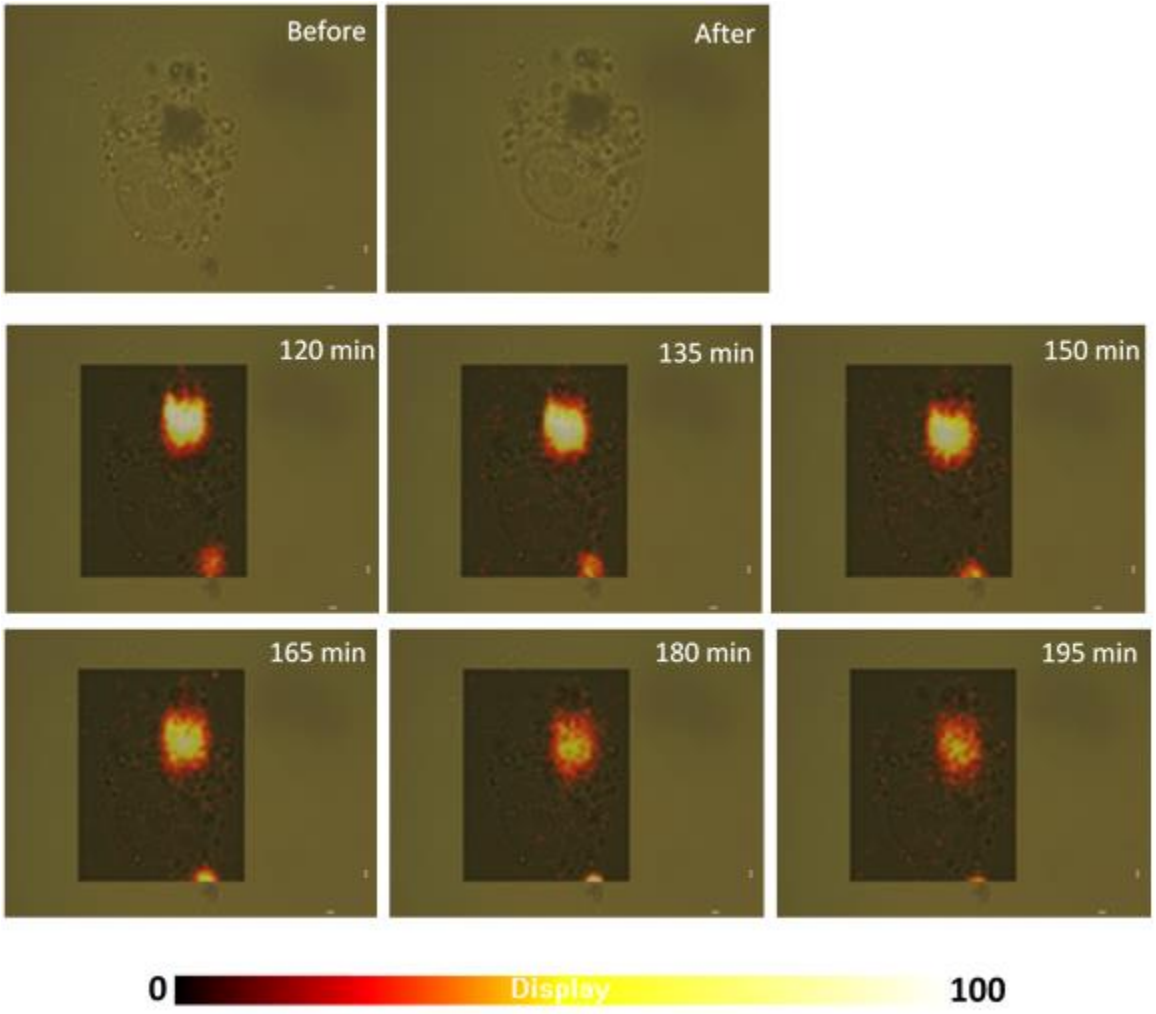


Figure 5.6 Single cell Raman mapping of S18 cells after 120, 135, 150, 165, 180 and 195 min incubation of Gd-Au nanoprobes. The color scale is generated with peak intensity at 1075 cm^{-1} and is kept constant with Figure 5.5.

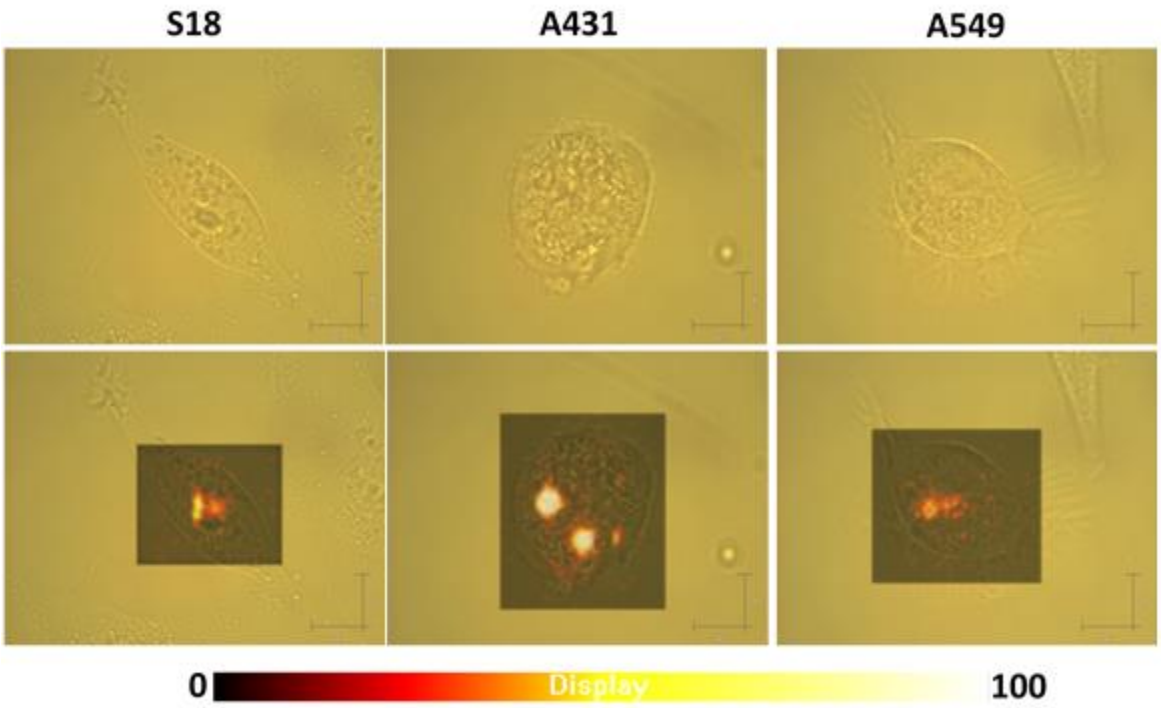


Figure 5.7 Representative Raman images of single S18, A431 and A549 cells incubated with Gd-Au nanoprobes (mAb-NPs). The first row shows bright field image and the selected area, and second row shows the corresponding Raman images. The color scale is generated with peak intensity at 1075 cm^{-1} and is kept constant with Figure 5.5.

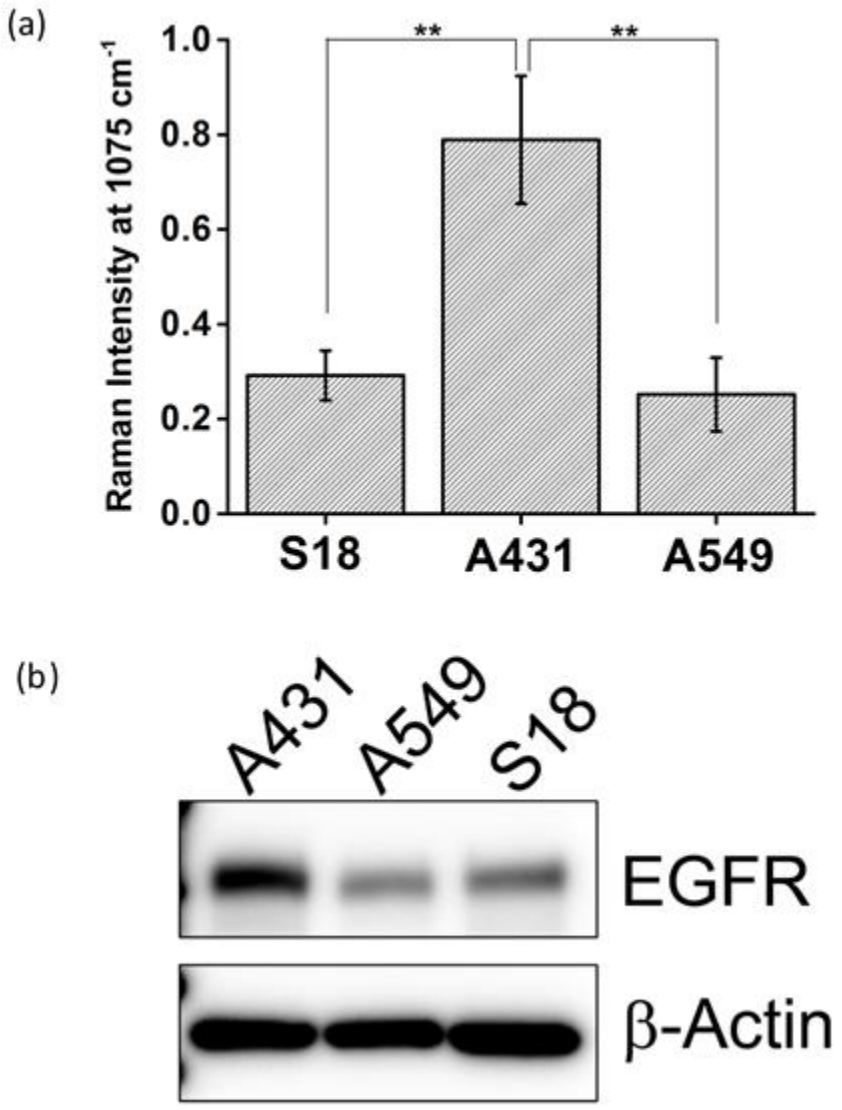


Figure 5.8 (a) Average peak intensity at 1075 cm^{-1} for S18, A431 and A549 cells with Gd-Au nanoprobes incubation. Data are collected from 50 spectra for each sample. **P<0.01. (b) Western blot result showing EGFR expression levels in S18, A431 and A549 cells.

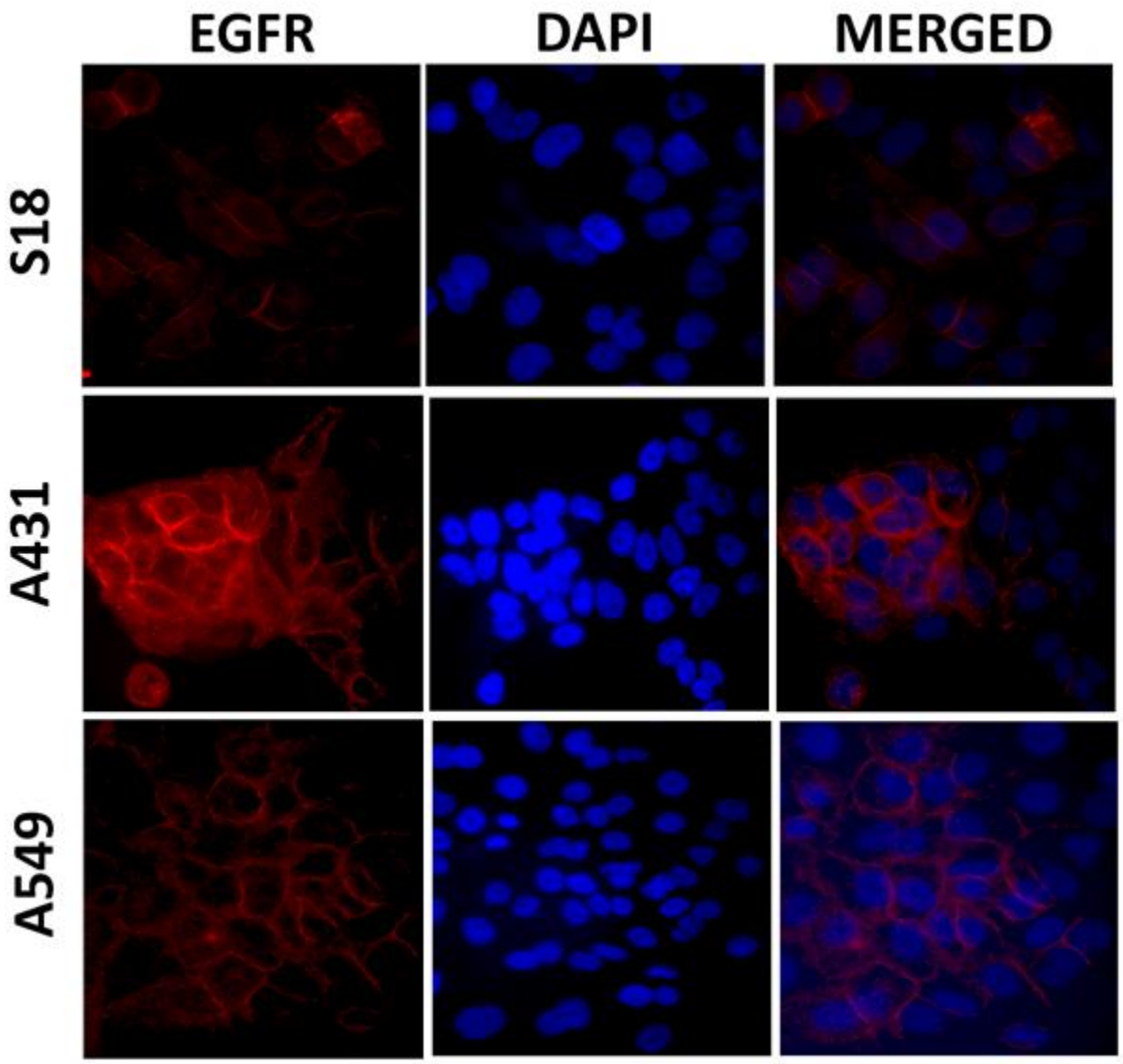


Figure 5.9 Immunofluorescence images showing the EGFR expression in S18, A431 and A549 cells.

CHAPTER 6

SERS-FLUORESCENCE BIMODAL IMAGING OF FATTY ACID RESPONSIVE RECEPTOR GPR120

6.1 ABSTRACT

G-protein-coupled receptor 120 (GPR120), as a member of the rhodopsin family of G-protein-coupled receptors, has been shown to function as a sensor for dietary fat in the gustatory and digestive systems. Its specific role in the chemoreception of fatty acids, which is thought to be crucial in understanding mechanism of fat intake and treatment of obesity, remains unclear. Here we report a novel imaging technique using surface-enhanced Raman spectroscopy (SERS)-fluorescence bimodal nanoprobes for detection and imaging of GPR120 in single living cells. Construction and characterization of the bimodal nanoprobes are described in detail. Biocompatibility and imaging capability of the probes are investigated using a model HEK293 cell line with a inducible GPR120 gene transfection. Cellular distribution of GPR120 are visualized by single-cell SERS and fluorescence imaging. A dose-dependent GPR120 response to linoleic acid (LA) treatment is measured by SERS.

6.2 INTRODUCTION

Dietary lipids (e.g. fatty acids, triglycerides) make up as high as 40% of daily caloric intakes in Western diet, which is thought contribute greatly to the prevalence of obesity and associated diseases [1-3]. Understanding the mechanisms underlying the perception of dietary lipids thus is important to help control fat intake preference and develop treatment of obesity. G protein-coupled receptors (GPCRs) have been shown to play important roles in cellular signaling pathways that affect human sense of taste (e.g.

sweet, bitter) [4, 5]. GPR120 and GPR40, members of GPCR family, have recently been reported to mediate response to long chain fatty acids (LCFAs) [6]. Both GPR120 and GPR40 knock-out mice showed a diminished preference for linoleic acid and oleic acid, and diminished taste nerve responses. In addition, studies have shown that GPR120 and CD36, LCFA receptors identified in rodent taste bud cells, mediate differential Ca^{2+} response to fatty acids, and are differentially regulated by dietary lipids [7, 8]. Though several lipid receptor candidates (e.g. GPR120, GPR40, and CD36) have been found in the tongue papillae, the mechanism how these receptors act in the perception of LCFAs remains unresolved and merits further extensive studies [3]. It will be beneficial to develop an imaging technique that can visualize how these receptors act when binding with LCFAs in single cells, in order to understand their specific roles in fat perception.

Surface-enhanced Raman spectroscopy (SERS) is a novel and powerful optical imaging technique that can be applied in single cell bioanalysis. SERS is able to achieve 10~14 orders of magnitude enhancement of spontaneous Raman signal by conjugate a molecule to a noble metal (e.g. Au, Ag) nanostructure [9], which allows detection of biomolecules with ultrahigh sensitivity [10, 11]. To generate SERS activity, a SERS nanoprobe composed of noble metal nanoparticle, Raman reporter molecule, and surface stabilizer are usually constructed and applied. Due to advantages of high stability and biocompatibility, especially great capability of multiplex detection, SERS nanoprobes have been applied in a variety of bioapplications such as molecular detection [12, 13], single living cell imaging [14-16], and *in vivo* biosensor [17, 18]. In addition, SERS imaging, by generating a pseudo-color map based on relative intensities of selected Raman bands, is able to map the distribution of biomolecules such as lipids and proteins [19, 20], cell

surface receptors [17, 21] and even bacterial species [22, 23] at single cell level. However, SERS is a low-throughput imaging technique and it requires a long acquisition time (e.g. several seconds) to get reliable Raman spectrum, due to relatively weak signal by Raman scattering (even after SERS enhancement). This limits the application of SERS in biological analysis, especially for high-throughput cell sorting and imaging [24].

To overcome the limitation and expand the functionality, multimodal imaging probes have been developed to integrate SERS with other imaging modalities, such as magnetic resonance imaging (MRI) [25], X-ray computed tomography (CT) [26, 27] and fluorescence imaging [28-30]. Among these modalities, fluorescence, due to its fast imaging speed and high-throughput imaging ability, is considered as a promising complementary technique to SERS. Fluorescence functions for quick recognition of the analytes in complex biosystems, while SERS is used to accurately detect multiplex targets in single cells. Recently, Choo *et al.* [31] reported a SERS-fluorescence bimodal imaging technique to investigate multiple cancer markers co-localized in single breast cancer cells.

Here we developed a SERS-fluorescence bimodal nanoprobe for detection and imaging of GPR120 in single cells. Europium-doped calcium molybdate nanoparticles ($CaMoO_4:Eu^{3+}$) showed intense red fluorescence emission under UV light excitation [32]. This fluorescence-active $CaMoO_4:Eu^{3+}$ nanoparticle was conjugated with SERS-active gold nanorods (AuNR) encapsulated with Raman reporter molecule 4-mercaptobenzoic acid (MBA), to realize SERS-fluorescence dual functions. The composite nanoparticle was conjugated with antibody for specific targeting of GPR120 expressed in living cells. By using this bimodal nanoprobe, we successfully realize SERS-fluorescence imaging

specifically for GPR120 at single cell level. In addition, for the first time, we observed a linear dose-dependence of GPR120 on linoleic acid (LA) treatments.

6.3 MATERIALS AND METHODS

6.3.1 Materials

4-mercaptobenzoic acid (MBA), N-(3-Dimethylaminopropyl)-N'-ethylcarbodiimide hydrochloride (EDC), N-hydroxysuccinimide (NHS), doxycycline hydrochloride (DOX), linoleic acid (LA), europium(III) nitrate hydrate ($Eu(NO_3)_3 \cdot xH_2O$) were purchased from Sigma-Aldrich (St. Louis, MO). Calcium nitrate tetrahydrate, ($Ca(NO_3)_2 \cdot 4H_2O$), ammonium molybdate ($H_8MoN_2O_4$), oleic acid, 1-octadecene were purchased from Alfa Aesar (Ward Hill, MA). Blasticidin S HCl, Hygromycin B, phosphate-buffered saline (PBS), 0.5% trypsin-EDTA, LIVE/DEAD Viability/Cytotoxicity Assay Kit were purchased from Life Technologies (Carlsbad, CA). The polyethylene glycol (PEG) products, thiol PEG acid (HS-PEG-COOH, MW 5000) and methoxyl PEG thiol (mPEG-SH, MW 5000), were purchased from Nanocs Inc. (USA). Polyclonal GPR120 antibody was purchased from Santa Cruz Biotechnology Inc. (sc-99105). Ultrapure water (18 $M\Omega\ cm^{-1}$) was used in this work.

6.3.2 Characterization techniques

Transmission electron microscopy (TEM) images and energy-dispersive X-ray spectroscopy spectrum (EDX) were acquired using an FEI Titan 80–300 kV (S) TEM equipped with a spherical aberration (Cs) image corrector (300 kV). For the TEM measurements, the powder samples were ground and dispersed in methanol. Few drop of dispersed particles were placed on a carbon coated-copper grid and allowed to dry at room temperature. Absorption spectra were acquired by Multiskan Spectrum spectrophotometer

(Thermo Scientific). FT-IR spectra were acquired by Varian 660-IR FT-IR spectrometer (Agilent Technologies). Luminescent spectra were acquired by FluoroMax-3 fluorometer (Horiba Scientific). Raman spectra were measured by Renishaw inVia Raman spectrometer equipped with a 785 nm near-IR laser, which was focused through a 63x water immersion lens (NA=0.90, Leica Microsystems). Spectral smoothing and autofluorescence background subtraction were performed using an automated algorithm program kindly provided by BC Cancer Research Center [33]. The processed spectra were exported to OriginPro 9 software for plotting. Data were reported as mean ± SE (standard error of mean). Statistical difference was analyzed by one-way analysis of variance (ANOVA).

6.3.3 Synthesis of $CaMoO_4:Eu^{3+}$@AuNR hybrid nanoparticles

Europium-doped calcium molybdate ($CaMoO_4:Eu^{3+}$) nanoparticles were prepared via a simple thermolysis process ~309 ^oC. The preparation procedure can be briefly described as follows: 21 mg of $Eu(NO_3)_3 \cdot xH_2O$, 50 mg of NaOH, and 1.0 g of $Ca(NO_3)_2.4H_2O$ were dissolved in 2 mL of distilled water. The mixture was treated with 2 mL of OA and 18 mL ODE and heated in a round-bottom flask at 80 °C for 1 hr under continuous stirring. In another beaker, 0.423 g of $H_8MoN_2O_4$ was dissolved in 3 mL of DI water, and 0.1 g of NaOH, 2 mL of OA, and 18 mL of ODE were added and stirred the solution at 80 °C for 1 hr. The two solutions were mixed under continuous stirring and heated at 80 °C for 30 min, and then the reaction was refluxed at 309 °C for 1 hr. The resulting precipitate was collected by centrifugation at ~2500 g after washing with ethanol. The obtained precipitate was cooled at room temperature for 2 days.

For the synthesis of $CaMoO_4:Eu^{3+}$@AuNR hybrid nanoparticles, commercially available Au nanorods (AuNRs) with 10 nm in diameter and 35 nm in length were purchased from Nanopartz. Initially, 4 mL of the AuNR was centrifuged at 12000 g for 30 min to remove the excess of CTAB and then redispersed in PBS. Centrifugation was repeated for three times to reduce the excess of CTAB present on the surface of the AuNR. 4 mL of AuNR dispersed in PBS was added to 1 mL of the PEGylated $CaMoO_4:Eu^{3+}$ nanoparticles under continuous stirring and then sonicated for 1 hr. The resulting solution was centrifuged, and the hybrid nanoparticles precipitated was collected. These particles were washed with a PBS solution for three times and redispersed in PBS.

6.3.4 Functionalization of SERS-fluorescence bimodal probe

One mL of as-prepared $CaMoO_4:Eu^{3+}$@AuNR composite nanoparticle solution was mixed with MBA solution (1mM, 10 µL) and reacted for 30 min. Solutions of HS-PEG-COOH (1 mg/mL, 10 µL) and mPEG-SH (1 mg/mL, 40 µL) were sequentially added to the nanoparticle solution and incubated for 2 hr. The resultant solution was then centrifuged (12000 g, 15 min) to remove excess PEG and MBA. Particles were resuspend in water. Freshly prepared EDC (10 mM, 10 µL) and NHS (25 mM, 10 µL) solutions were mixed with the nanoparticle solution and reacted for 30 min. The resultant solution was centrifuged and particles were resuspended in PBS. Finally, anti-GPR120 antibody (0.2 mg/mL, 10 µL) was added to the nanoparticle solution and reacted for 1 hr. Excess antibody was removed by centrifugation. Nanoparticles were resuspended in PBS. The functionalized nanoprobe ($CaMoO_4:Eu^{3+}$@AuNR-MBA-Ab) was stable in solution for several days at 4 ºC.

6.3.5 Cell culture

HEK293 cell lines transfected with an inducible GPR120 gene (HEK293-GPR120) and a constitutive CD36 gene (HEK293-CD36) were used in this context. Cells were grown in DMEM-GlutaMAX media (Life Technologies, 10569-010) supplemented with 10% Tet-free fetal bovine serum (Fisher, NC0290780). Cells were cultured in a humidified atmosphere at 37 ºC with 5% CO_2, and were passaged at 80~90% confluence. Blasticidin S HCl (10 µg/mL) and Hygromycin B (100 µg/mL) were added to cell culture medium specifically for maintenance of inducible GPR120 gene. To express GPR120, HEK293-GPR120 cells were induced with DOX at 0.5 µg/mL for 48 hr.

6.3.6 Cell staining and Viability test

The cell viability was analyzed using LIVE/DEAD Viability/Cytotoxicity Assay Kit (Invitrogen) according to the manufacturer's instruction. Briefly, (1) cells were cultured in poly-D-lysine coated glass-bottom dishes (MatTek Cop. USA) for 24 hr; (2) cells were then washed with PBS twice; (3) 2 ml of mixed solution of 2 µM Calcein AM and 4 µM ethidium homodimer-1 (EthD-1) (both from Invitrogen) was added directly to cells, and incubated cells for 30 min at room temperature; (5) cells were imaged using fluorescence microscope to analyze the relative proportion of live/dead cells. A 10× objective was used to observe fluorescence.

Calcein AM was well retained within live cells producing green fluorescence; however, EthD-1 entered cells with damaged membrane and bonded to nucleic acids, producing a red fluorescence in dead or membrane-damaged cells. Therefore, the live/dead cells were differentiated visually.

6.3.7 Cellular fluorescence and SERS imaging

For fluorescence and SERS imaging experiments, cells were incubated with the functionalized nanoprobe ($CaMoO_4:Eu^{3+}$@AuNR-MBA-Ab) for 24 hr, and rinsed with PBS 3 times before imaging experiments. For LA treatments, cells were first treated with LA for 5 min at different concentrations, and then incubated with nanoprobes for 24 hr.

Cellular fluorescence imaging was performed on an Olympus IX71 inverted microscope with an external 285 nm UV lamp. Images were acquired and processed using DPController software (Olympus Corporation) to maintain identical light exposure for three different cell conditions.

For SERS measurements, cells were seeded on a cleaned magnesium fluoride (MgF2) optical window (United Crystals Co.) to minimize background signal from substrate. Raman spectra between 600~1800 cm^{-1} were recorded under 10s laser exposure (3mW). For each sample, 25 spectra from 25 cells with 1spectrum per cell were collected. Raman mappings were generated using Renishaw WiRE 3.3 software.

6.4 RESULTS AND DISCUSSION

6.4.1 Nanoparticle Structure characterization

The typical TEM image of the composite $CaMoO_4:Eu^{3+}$@AuNR NPs is shown in Figure 6.1a. It confirms the formation of hybrid nanoparticles where AuNR is attached to the surface of $CaMoO_4:Eu^{3+}$ NP. The presence of each element in the particle was confirmed by EDX spectrum (Figure 6.1a, inset). The average size of $CaMoO_4:Eu^{3+}$ nanoparticles is found to be ~20 nm, whereas, average lengths and widths of AuNR is found to be ~40 and 10 nm, respectively. Moreover, the hybrid nanoparticles show high dispersion for long-time without precipitation. The crystalline nature of the $CaMoO_4:Eu^{3+}$

nanoparticles was confirmed by X-ray diffraction pattern (not shown here). All peaks are well match with the tetragonal structure of $CaMoO_4:Eu^{3+}$ (JCPDF#29-0351). The UV-Vis spectra of hybrid nanoparticles in the range 200–1000 nm are shown in Figure 6.1b. A strong absorption bands at 512.5 and 789 nm was observed, which are assigned to transverse and longitudinal surface plasmon resonance (SPR) bands of AuNR, respectively. It is observed that the peak positions of SPR band at 789 nm is slightly red-shifted (~0.8 nm) and full width at half maximum (*FWHM*) increases by ~27 nm, whereas there is no shift for SPR band at 512.5 nm and FWHM increased by ~14.4 nm on antibody coating on the surface of nanoparticles. Moreover, a small hump ~265 nm was observed for $CaMoO_4$:Eu@AuNR NPs, this is ascribed to a charge transfer from the oxygen ligands to the central molybdenum atom within the MoO_4^{2-} cluster (also called Mo–O charge transfer band (CTB)), but no such peak was observed for bare AuNR. It was further confirmed by excitation spectra (λ_{em} = 615 nm). Also some weak peaks in the longer wavelength region 300–500 nm are ascribed to the direct $4f^6$–$4f^6$ intraconfiguration transitions of Eu^{3+} ion (Figure 6.1d, inset) [34]. The $CaMoO_4:Eu^{3+}$@AuNR NPs emits strong red fluorescence under 270, 285, 300, 395, and 464 nm excitations (Figure 6.1d) peaks centered at 590 ($^5D_0 \rightarrow {}^7F_1$; magnetic dipole transition) and 615 nm ($^5D_0 \rightarrow {}^7F_2$; electric dipole transition). The high-energy state excited (Mo–O CTB and Eu^{3+}) electrons of Eu^{3+} are unstable and relaxed back to back to ground states of Eu^{3+} ion through photons emission in visible region. The intensity of $^5D_0 \rightarrow {}^7F_2$ transition is significantly higher than other transitions of Eu^{3+} ion [35]. Strong luminescence of $CaMoO_4:Eu^{3+}$@AuNR NPs may be particularly useful for biological fluorescence labeling.

Figure 6.1c shows the FT-IR spectra of bare $CaMoO_4:Eu^{3+}$, $CaMoO_4:Eu^{3+}$@AuNR, and antibody-conjugated $CaMoO_4:Eu^{3+}$@AuNR hybrid nanoparticles in the range from 4000–500 cm^{-1}. Peak at ~1650 and 3450 cm^{-1} correspond to bending and stretching vibrations of H–O–H molecules present on the surface of the hybrid nanoparticles. The characteristic peaks appears ~802 cm^{-1} is assigned to asymmetric stretching vibration of O–Mo–O vibration in the MoO_4^{2-} tetrahedron [36]. The peaks at 2923 and 2852 cm^{-1} indicating the C–H streaching vibrations arises from OA [37]. On antibody conjugation to $CaMoO_4:Eu^{3+}$ nanoparticles with AuNR and AuNR-Ab the peaks become broaden. The FTIR spectrum of pure HS–PEG–COOH, mPEG-HS, and antibody are show in Figure 6.2. It was found that pure HS–PEG–COOH has sever characteristic peaks between 1700–1000 cm^{-1}, whereas some feeble peaks were observed ~2500, 1244, and 1076 cm^{-1} for antibody. Moreover, the conjugation of the antibody to the $CaMoO_4$:Eu@AuNR nanoparticles results some small peaks between 1700–1000 cm^{-1} which are characteristic of peaks arises from PEG and/or antibody present on the surface of the nanoparticles. It further confirms the presence of antibody coating on the surface of the particles.

6.4.2 Functionalization and performance of SERS-fluorescence bimodal probe

As prepared $CaMoO_4:Eu^{3+}$@AuNR nanocomposite was further functionalized to generate intense Raman signals and achieve specific targeting. Figure 6.3a demonstrate the functionalization process containing three steps: (1) MBA, as a Raman reporter molecule providing strong chemical enhancement of the SERS signal and simple SERS spectrum, was conjugated onto the nanocomposite through covalent Au-S bond. (2) PEG linkers were coated to improve the stability and biocompatibility of the nanoprobe, as well as to minimize the non-specific binding of the nanoprobes to cells. (3) Finally, anti-GPR120

antibodies were conjugated onto the nanocomposite to realize specific GPR120 targeting in cells. The specificity of GPR120 antibody was determined by immunofluorescence imaging (Figure 6.4). Under 1:250 dilution ratio, the antibody exhibited good specificity in labeling GPR120 in cells. Thus, this ratio was used in nanoprobe functionalization and cell incubation.

The performance of functionalized nanoprobe ($CaMoO_4:Eu^{3+}$@AuNR-MBA-Ab) was assessed by SERS and fluorescence imaging. The constructed probes were incubated with cells for 24 hr at final concentration of 100 μg/mL. Three different cell samples are: (1) HEK293-GPR120 cells induced with DOX for 48 hr (GPR120 (+)); (2) HEK293-GPR120 cells without DOX inducing (GPR120 (-)); (3) constitutive HEK293-CD36 (CD36) cells. Representative SERS spectra of the nanoprobe-treated cells are shown in Figure 6.3b. Typical spectrum of GPR120 (+) cells shows two enhanced peaks at 1078 and 1585 cm^{-1}, which are assigned to the ring breathing and axial deformation modes of MBA, respectively [38, 39]. In contrast, spectra of GPR120 (-) and CD36 cells show nearly no Raman peaks from the reporter molecule MBA, but only regular Raman signals from cells (e.g. 1003 cm^{-1} from phenylalanine). Average peak intensity at 1078 cm^{-1} for GPR120 (+) cells is significantly higher ($P<0.001$, $N=25$) than GPR120 (-) and CD36 cells (Figure 6.3c). This difference is resulted from the specific targeting ability of the constructed nanoprobe $CaMoO_4:Eu^{3+}$@AuNR-MBA-Ab, which selectively binds to GPR120 (+) cells through specific antibody-antigen interactions, bringing significantly enhanced SERS signal. This finding can also be confirmed by fluorescent images, in which the $CaMoO_4:Eu^{3+}$@AuNR-MBA-Ab nanoprobe-incubated GPR120 (+) cells exhibited considerable red fluorescence while the fluorescence of GPR120 (-) cells was almost invisible (Figure 6.5).

6.4.3 Biocompatibility

Biocompatibility of the SERS-fluorescence bimodal nanoprobe $CaMoO_4$:Eu^{3+}@AuNR-MBA-Ab was estimated by incubating GPR120 (+) cells with the nanoprobes at different concentrations (20, 50, 80, 100, 200 μg/mL) for 24 hr, and then testing the cell viability using live/dead fluorescence imaging. As shown in Figure 6.6, there were no significant decreases in cell viability when incubating cells with nanoprobes at concentration as high as 100 μg/mL. Thus, this concentration (100 μg/mL) was chosen in further imaging experiments.

6.4.4 Cellular fluorescence and SERS imaging

Cellular imaging capability of the bimodal nanoprobe was estimated by fluorescence and SERS imaging. Fluorescent images of nanoprobe-treated multiple cells successfully demonstrated the difference in GPR120 levels between DOX-induced and non-induced HEK293-GPR120 cells (**Figure 6.5**). Besides, due to its high-throughput nature, fluorescence was also used to quickly identify individual cells with high GPR120 expression levels. At single cell level, as shown in Figure 6.7, CD36 cell showed hardly visible red fluorescence at the central area of the cell (Figure 6.7b); on the other hand, GPR120 (+) cell had strong red color all over the cell (Figure 6.7d). Because the nanoprobes were conjugated with anti-GPR120 antibodies, they tended to bind with GPR120 but not CD36 at cell surface.

Furthermore, cellular SERS imaging was performed on the nanoprobe-treated cells. SERS images were created using the Raman intensities of peak 1078 cm^{-1}, which is the most stable and reproducible characteristic peak from the reporter molecule, MBA. By collecting the peak intensity values all over the cell and transforming them into color values,

GPR120 distribution were reflected by the brightness of the SERS image at single cell or subcellular level. Figure 6.8 showed the single-cell SERS mapping of GPR120. Apparently, strong SERS signals were recorded on GPR120 (+) cell (Figure 6.8d), while SERS signals at the CD36 cell were nearly undetected (Figure 6.8b). SERS imaging is able to mapping the heterogeneous distribution of GPR120 receptors at single cell level, providing more accurate spatial information than regular fluorescence imaging.

6.4.5 Detection of GPR120 under LA treatment by SERS

GPR120 responses to LA treatments were measured by SERS. GPR120 (+) cells were treated with LA at concentrations 0, 5, 20, 30, and 60 μM for 5 min, and then incubated with nanoprobes for 24 hr. After washing off the unabsorbed nanoparticles, cells were taken for Raman measurements. Figure 6.9a showed the average SERS spectra (N=25) of the LA-treated cells. Two major intense peaks at 1078 and 1585 cm^{-1} were from the nanoprobes, which represent the activity level of GPR120 receptors. Elevated SERS signals were observed in high LA concentration treatments (Figure 6.9b, inset). Peak intensity at 1078 cm^{-1} vs. LA concentration was plotted in Figure 6.9b. It was found that there is a linear relationship ($R^2 = 0.93$) between the SERS intensity and LA concentrations. This result indicates GPR120 activity is up-regulated by LA treatment, which is consistent with previous reports using other methods [7]. Furthermore, for the first time, we found that there is a linear dose-dependence of GPR120 to LA in 0~60 μM concentration range.

6.5 CONCLUSIONS

In summary, we developed a dual functional composite nanoprobe for SERS-fluorescence bimodal imaging of fat-responsive receptor GPR120 in single living cells. The dual functional nanoprobe was composed of europium-doped calcium molybdate and

gold nanorod, and further functionalized with Raman reporter and anti-GPR120 antibody. The functionalized nanoprobe was successfully applied for both SERS and fluorescence detection of GPR120 in different cell lines. Fluorescence served as an indicator for fast recognition of the target, while SERS functions for accurate localization of molecular signature in single cells. In particular, cellular distribution of GPR120 was successfully detected by single-cell SERS mapping. Taking advantages of the quantification ability of SERS, we observed an up-regulation of GPR120 by LA treatment. Moreover, a linear relationship between GPR120 activity and LA concentration in 0~60 μM range was observed for the first time. Our future direction is to build multiplex imaging probes for simultaneous detection of major lipid receptors such as GPR120, GPR40 and CD36, trying to unveil the enigma how these receptors interact with each other in the chemoreception of fatty acids.

6.6 REFERENCES

[1] T.T. Fung, E.B. Rimm, D. Spiegelman, N. Rifai, G.H. Tofler, W.C. Willett, F.B. Hu, Association between dietary patterns and plasma biomarkers of obesity and cardiovascular disease risk, Am. J. Clin. Nutr. 73 (2001) 61-67.

[2] L. Cordain, S.B. Eaton, A. Sebastian, N. Mann, S. Lindeberg, B.A. Watkins, J.H. O'Keefe, J. Brand-Miller, Origins and evolution of the Western diet: health implications for the 21st century, Am. J. Clin. Nutr. 81 (2005) 341-354.

[3] S. Abdoul-Azize, S. Selvakumar, H. Sadou, P. Besnard, N.A. Khan, Ca^{2+} signaling in taste bud cells and spontaneous preference for fat: unresolved roles of CD36 and GPR120, Biochimie 96 (2014) 8-13.

[4] R.F. Margolskee, Molecular mechanisms of bitter and sweet taste transduction, J. Biol. Chem. 277 (2002) 1-4.

[5] E. Adler, M.A. Hoon, K.L. Mueller, J. Chandrashekar, N.J.P. Ryba, C.S. Zuker, A novel family of mammalian taste receptors, Cell 100 (2000) 693-702.

[6] C. Cartoni, K. Yasumatsu, T. Ohkuri, N. Shigemura, R. Yoshida, N. Godinot, J. le Coutre, Y. Ninomiya, S. Damak, Taste preference for fatty acids is mediated by GPR40 and GPR120, J. Neurosci. 30 (2010) 8376-8382.

[7] M.H. Ozdener, S. Subramaniam, S. Sundaresan, O. Sery, T. Hashimoto, Y. Asakawa, P. Besnard, N.A. Abumrad, N.A. Khan, CD36-and GPR120-mediated Ca^{2+} signaling in human taste bud cells mediates differential responses to fatty acids and is altered in obese mice, Gastroenterology 146 (2014) 995-1005.

[8] C. Martin, P. Passilly-Degrace, D. Gaillard, J.F. Merlin, M. Chevrot, P. Besnard, The lipid-sensor candidates CD36 and GPR120 are differentially regulated by dietary lipids in mouse taste buds: impact on spontaneous fat preference, Plos One 6 (2011) e24014.

[9] J.P. Camden, J.A. Dieringer, J. Zhao, R.P. Van Duyne, Controlled plasmonic nanostructures for surface-enhanced spectroscopy and sensing, Accounts Chem. Res. 41 (2008) 1653-1661.

[10] K. Kneipp, Y. Wang, H. Kneipp, L.T. Perelman, I. Itzkan, R. Dasari, M.S. Feld, Single molecule detection using surface-enhanced Raman scattering (SERS), Phys. Rev. Lett. 78 (1997) 1667-1670.

[11] S.M. Nie, S.R. Emery, Probing single molecules and single nanoparticles by surface-enhanced Raman scattering, Science 275 (1997) 1102-1106.

[12] K. Kneipp, H. Kneipp, V.B. Kartha, R. Manoharan, G. Deinum, I. Itzkan, R.R. Dasari, M.S. Feld, Detection and identification of a single DNA base molecule using surface-enhanced Raman scattering (SERS), Phys. Rev. E 57 (1998) R6281-R6284.

[13] H.X. Xu, E.J. Bjerneld, M. Kall, L. Borjesson, Spectroscopy of single hemoglobin molecules by surface enhanced Raman scattering, Phys. Rev. Lett. 83 (1999) 4357-4360.

[14] K. Kneipp, A.S. Haka, H. Kneipp, K. Badizadegan, N. Yoshizawa, C. Boone, K.E. Shafer-Peltier, J.T. Motz, R.R. Dasari, M.S. Feld, Surface-enhanced Raman spectroscopy in single living cells using gold nanoparticles, Appl. Spectrosc. 56 (2002) 150-154.

[15] W. Xie, L. Wang, Y.Y. Zhang, L. Su, A.G. Shen, J.Q. Tan, J.M. Hu, Nuclear targeted nanoprobe for single living cell detection by surface-enhanced Raman scattering, Bioconjugate Chem. 20 (2009) 768-773.

[16] J.P. Scaffidi, M.K. Gregas, V. Seewaldt, T. Vo-Dinh, SERS-based plasmonic nanobiosensing in single living cells, Anal. Bioanal. Chem. 393 (2009) 1135-1141.

[17] A. Samanta, K.K. Maiti, K.S. Soh, X.J. Liao, M. Vendrell, U.S. Dinish, S.W. Yun, R. Bhuvaneswari, H. Kim, S. Rautela, J.H. Chung, M. Olivo, Y.T. Chang, Ultrasensitive near-infrared Raman reporters for SERS-based In vivo cancer detection, Angew Chem. Int. Edit. 50 (2011) 6089-6092.

[18] H. Kang, S. Jeong, Y. Park, J. Yim, B.H. Jun, S. Kyeong, J.K. Yang, G. Kim, S. Hong, L.P. Lee, J.H. Kim, H.Y. Lee, D.H. Jeong, Y.S. Lee, Near-infrared SERS nanoprobes with plasmonic Au/Ag hollow-shell assemblies for in vivo multiplex detection, Adv. Funct. Mater. 23 (2013) 3719-3727.

[19] M. Richter, M. Hedegaard, T. Deckert-Gaudig, P. Lampen, V. Deckert, Laterally Resolved and direct spectroscopic evidence of nanometer-sized lipid and protein domains on a single cell, Small 7 (2011) 209-214.

[20] H.W. Tang, X.B. Yang, J. Kirkham, D.A. Smith, Probing intrinsic and extrinsic components in single osteosarcoma cells by near-infrared surface-enhanced Raman scattering, Anal. Chem. 79 (2007) 3646-3653.

[21] L. Xiao, S. Harihar, D.R. Welch, A. Zhou, Imaging of epidermal growth factor receptor on single breast cancer cells using surface-enhanced Raman spectroscopy, Anal. Chim. Acta 843 (2014) 73-82.

[22] P.-J. Huang, L.-L. Tay, J. Tanha, S. Ryan, L.-K. Chau, Single-domain antibody-conjugated nanoaggregate-embedded beads for targeted detection of pathogenic bacteria, Chem.–Eur. J. 15 (2009) 9330-9334.

[23] R.M. Jarvis, R. Goodacre, Characterisation and identification of bacteria using SERS, Chem. Soc. Rev. 37 (2008) 931-936.

[24] M.Q. Li, J. Xu, M. Romero-Gonzalez, S.A. Banwart, W.E. Huang, Single cell Raman spectroscopy for cell sorting and imaging, Curr. Opin. Biotech. 23 (2012) 56-63.

[25] M.V. Yigit, L.Y. Zhu, M.A. Ifediba, Y. Zhang, K. Carr, A. Moore, Z. Medarova, Noninvasive MRI-SERS imaging in living mice using an innately bimodal nanomaterial, ACS Nano 5 (2011) 1056-1066.

[26] V. Amendola, S. Scaramuzza, L. Litti, M. Meneghetti, G. Zuccolotto, A. Rosato, E. Nicolato, P. Marzola, G. Fracasso, C. Anselmi, M. Pinto, M. Colombatti, Magneto-plasmonic Au-Fe alloy nanoparticles designed for multimodal SERS-MRI-CT imaging, Small 10 (2014) 3823-3823.

[27] M. Xiao, J. Nyagilo, V. Arora, P. Kulkarni, D.S. Xu, X.K. Sun, D.P. Dave, Gold nanotags for combined multi-colored Raman spectroscopy and x-ray computed tomography, Nanotechnology 21 (2010) 035101.

[28] Z. Wang, S. Zong, W. Li, C. Wang, S. Xu, H. Chen, Y. Cui, SERS-fluorescence joint spectral encoding using organic–metal–QD hybrid nanoparticles with a huge encoding capacity for high-throughput biodetection: putting theory into practice, J. Am. Chem. Soc. 134 (2012) 2993-3000.

[29] Y. Wang, L. Chen, P. Liu, Biocompatible triplex Ag@SiO_2@mTiO_2 core–shell nanoparticles for simultaneous fluorescence-SERS bimodal imaging and drug delivery, Chem.–Eur. J., 18 (2012) 5935-5943.

[30] X. Niu, H. Chen, Y. Wang, W. Wang, X. Sun, L. Chen, Upconversion fluorescence-SERS dual-mode tags for cellular and in vivo imaging, ACS Appl. Mater. Inter. 6 (2014) 5152-5160.

[31] S. Lee, H. Chon, S.Y. Yoon, E.K. Lee, S.I. Chang, D.W. Lim, J. Choo, Fabrication of SERS-fluorescence dual modal nanoprobes and application to multiplex cancer cell imaging, Nanoscale 4 (2012) 124-129.

[32] A.K. Parchur, R.S. Ningthoujam, S.B. Rai, G.S. Okram, R.A. Singh, M. Tyagi, S.C. Gadkari, R. Tewari, R.K. Vatsa, Luminescence properties of Eu^{3+} doped $CaMoO_4$ nanoparticles, Dalton T. 40 (2011) 7595-7601.

[33] J. Zhao, H. Lui, D.I. McLean, H. Zeng, Automated autofluorescence background subtraction algorithm for biomedical Raman spectroscopy, Appl. Spectrosc. 61 (2007) 1225-1232.

[34] B.P. Singh, A.K. Parchur, R.S. Ningthoujam, A.A. Ansari, P. Singh, S.B. Rai, Influence of Gd^{3+} co-doping on structural property of $CaMoO_4$:Eu nanoparticles, Dalton T. 43 (2014) 4770-4778.

[35] B.P. Singh, A.K. Parchur, R.S. Ningthoujam, A.A. Ansari, P. Singh, S.B. Rai, Enhanced photoluminescence in $CaMoO_4$:Eu^{3+} by Gd^{3+} co-doping, Dalton T. 43 (2014) 4779-4789.

[36] A.K. Parchur, A.I. Prasad, A.A. Ansari, S.B. Rai, R.S. Ningthoujam, Luminescence properties of Tb^{3+}-doped $CaMoO_4$ nanoparticles: annealing effect, polar medium dispersible, polymer film and core-shell formation, Dalton T. 41 (2012) 11032-11045.

[37] J. Huang, L. Wang, X. Zhong, Y. Li, L. Yang, H. Mao, Facile non-hydrothermal synthesis of oligosaccharides coated sub-5 nm magnetic iron oxide nanoparticles with dual MRI contrast enhancement effect, J. Mater. Chem. B 2 (2014) 5344-5351.

[38] A. Michota, J. Bukowska, Surface-enhanced Raman scattering (SERS) of 4-mercaptobenzoic acid on silver and gold substrates, J. Raman Spectrosc. 34 (2003) 21-25.

[39] W. Fang, Z. Wang, S. Zong, H. Chen, D. Zhu, Y. Zhong, Y. Cui, pH-controllable drug carrier with SERS activity for targeting cancer cells, Biosens. Bioelectron. 57 (2014) 10-15.

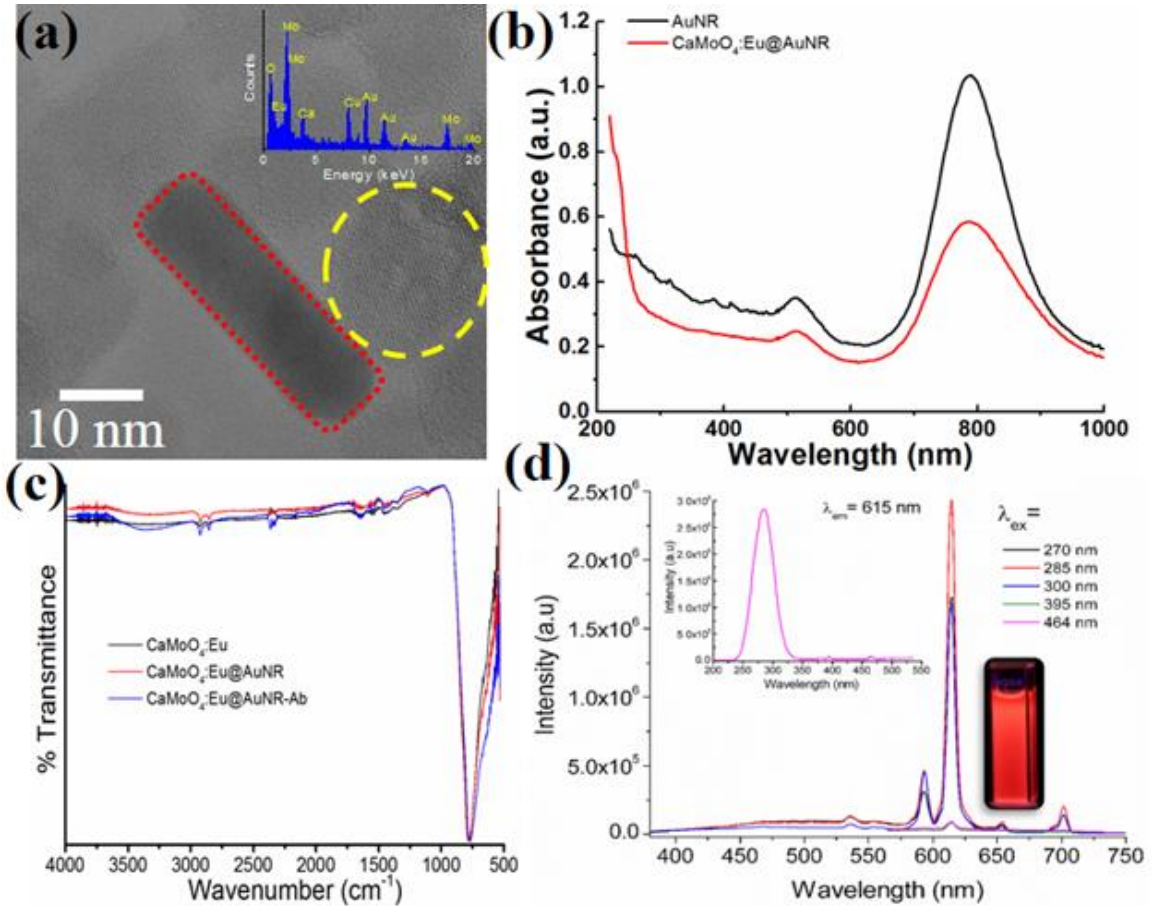


Figure 6.1 Characterization of the nanoprobe. (a) TEM image of $CaMoO_4:Eu^{3+}$@AuNR nanoparticle. Inset: EDX spectrum of the particle. (b) UV-Vis absorption spectra of AuNR and $CaMoO_4:Eu^{3+}$@AuNR. (c) FT-IR spectra of bare $CaMoO_4:Eu^{3+}$, $CaMoO_4:Eu^{3+}$@AuNR, and antibody-conjugated $CaMoO_4:Eu^{3+}$@AuNR. (d) Luminescent properties (excitation/emission) of the $CaMoO_4:Eu^{3+}$@AuNR nanoparticle.

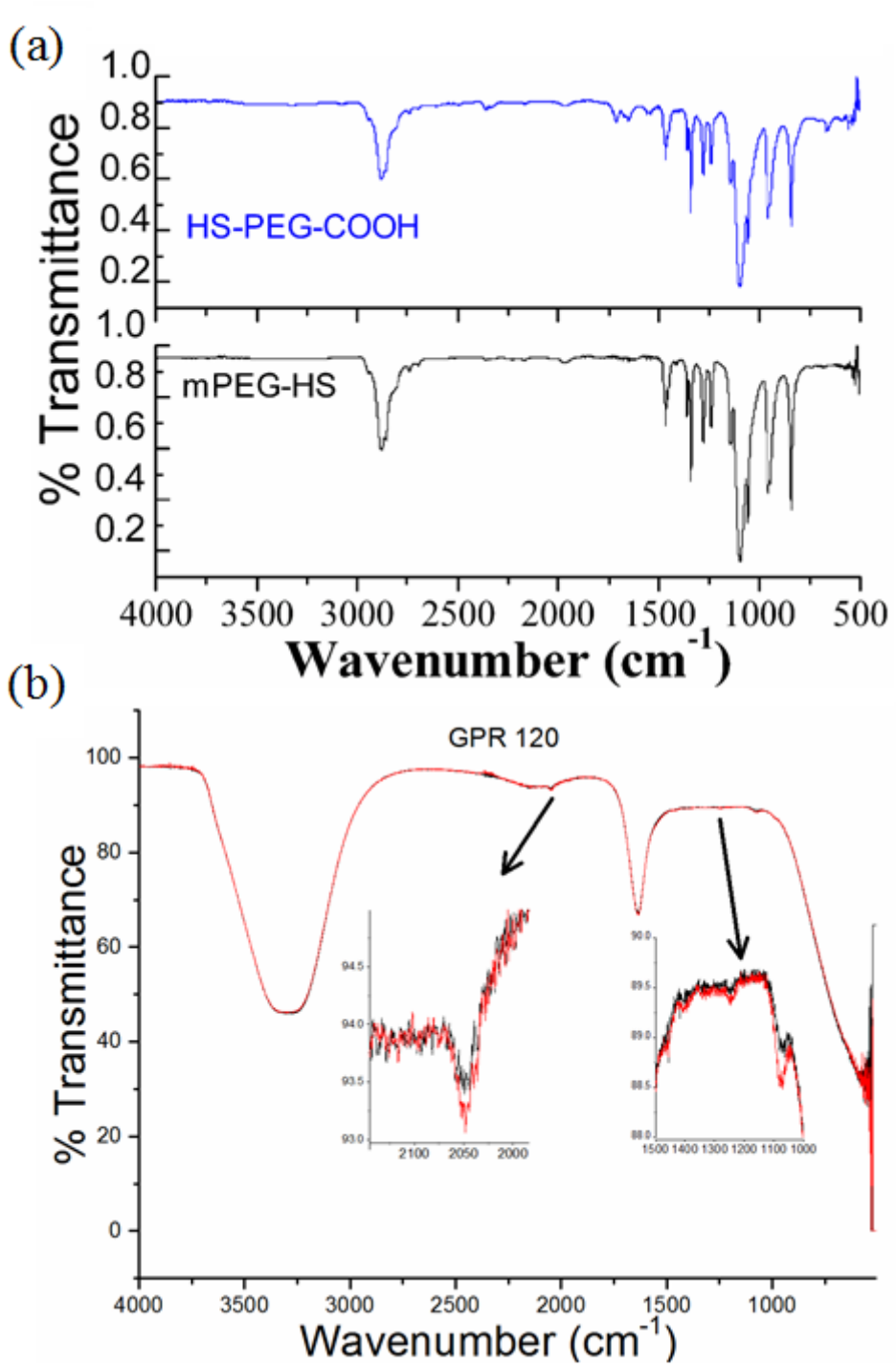


Figure 6.2 FT-IR spectra of (a) HS–PEG–COOH, mPEG-HS and (b) GPR120 antibody.

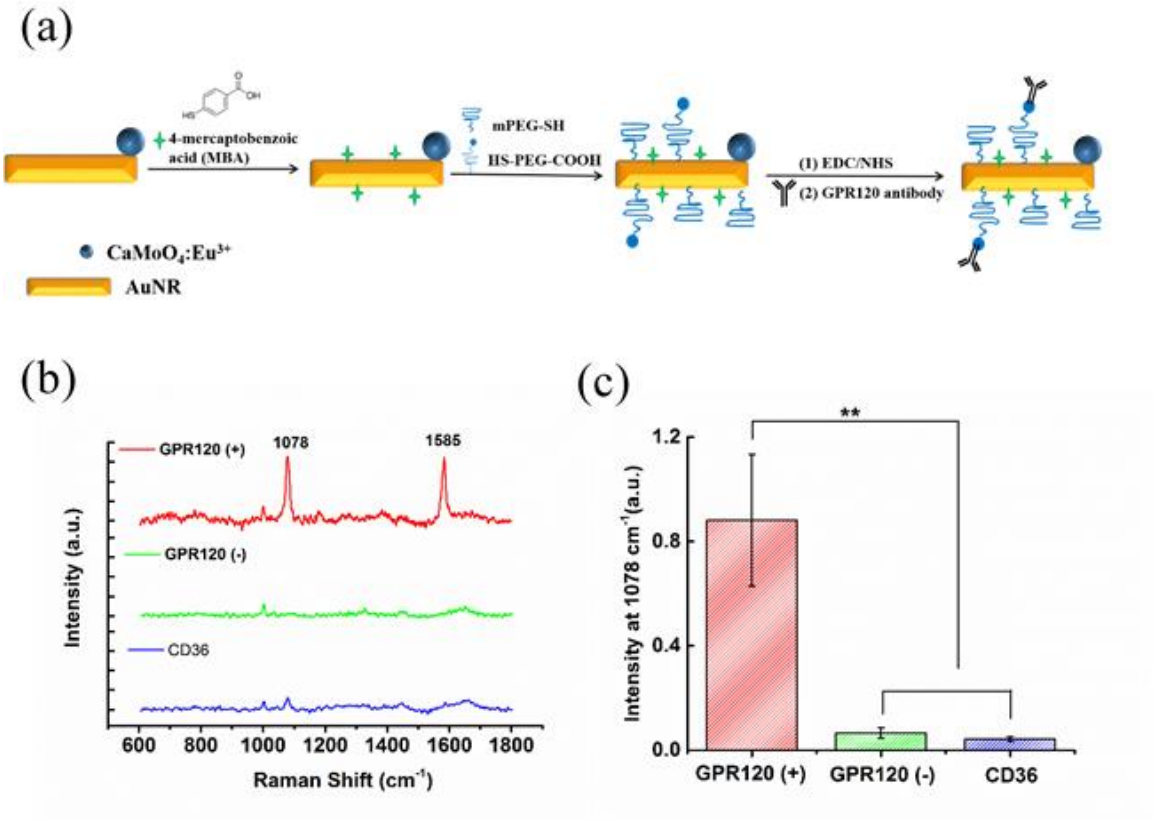


Figure 6.3 (a) Schematic for functionalization process of $CaMoO_4:Eu^{3+}$@AuNR nanocomposite. (b) Representative SERS spectra and (c) average SERS intensities at 1078 cm^{-1} (N=25) of $CaMoO_4:Eu^{3+}$@AuNR-MBA-Ab nanoprobe-incubated cell samples: (1) HEK293-GPR120 cells induced with DOX (GPR120 (+)); (2) HEK293-GPR120 cells without DOX inducing (GPR120 (-)); (3) constitutive HEK293-CD36 (CD36) cells. **P<0.001.

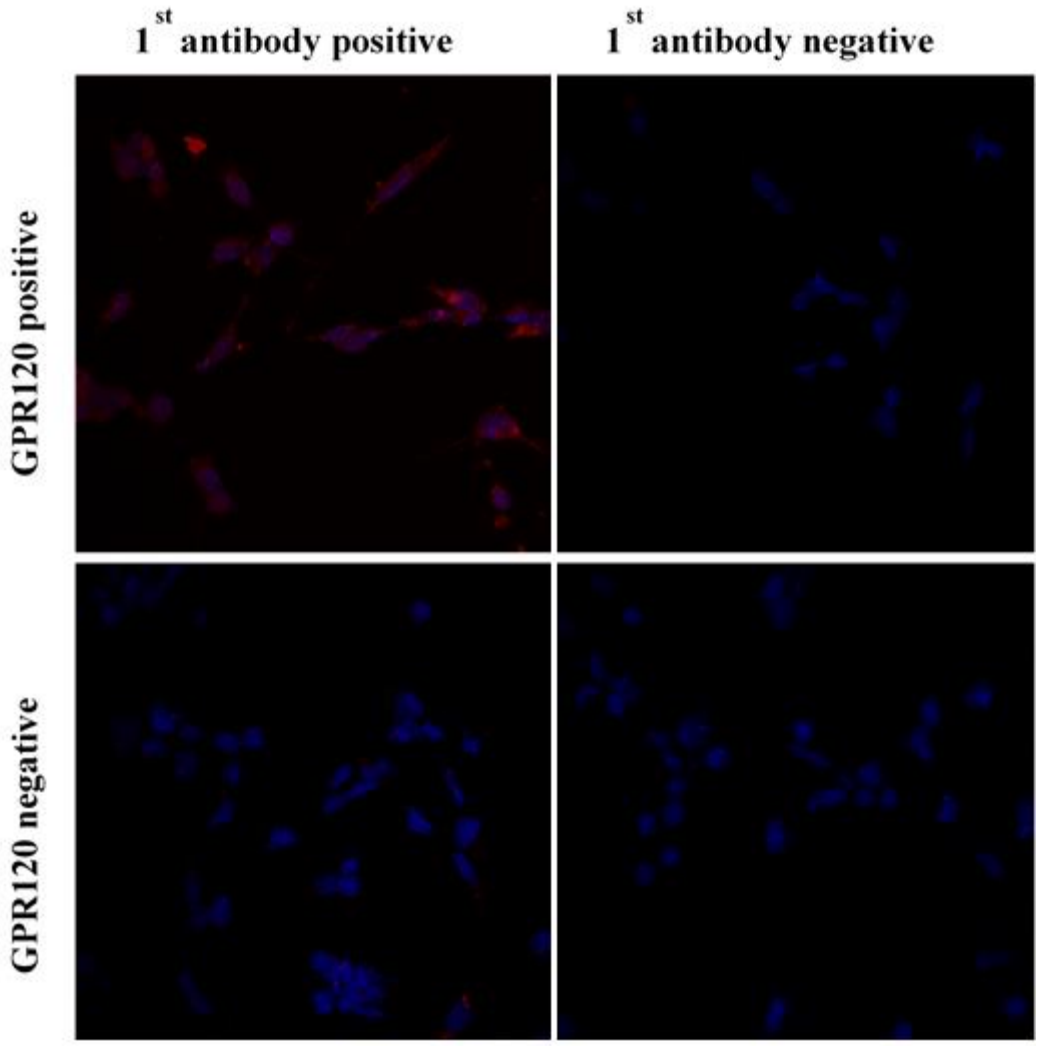


Figure 6.4 Immunofluorescence imaging to test the specificity of GPR120 antibody. Antibody ratio: 1st 1:250, 2nd 1:500. Color: red—GPR120, blue—DAPI.

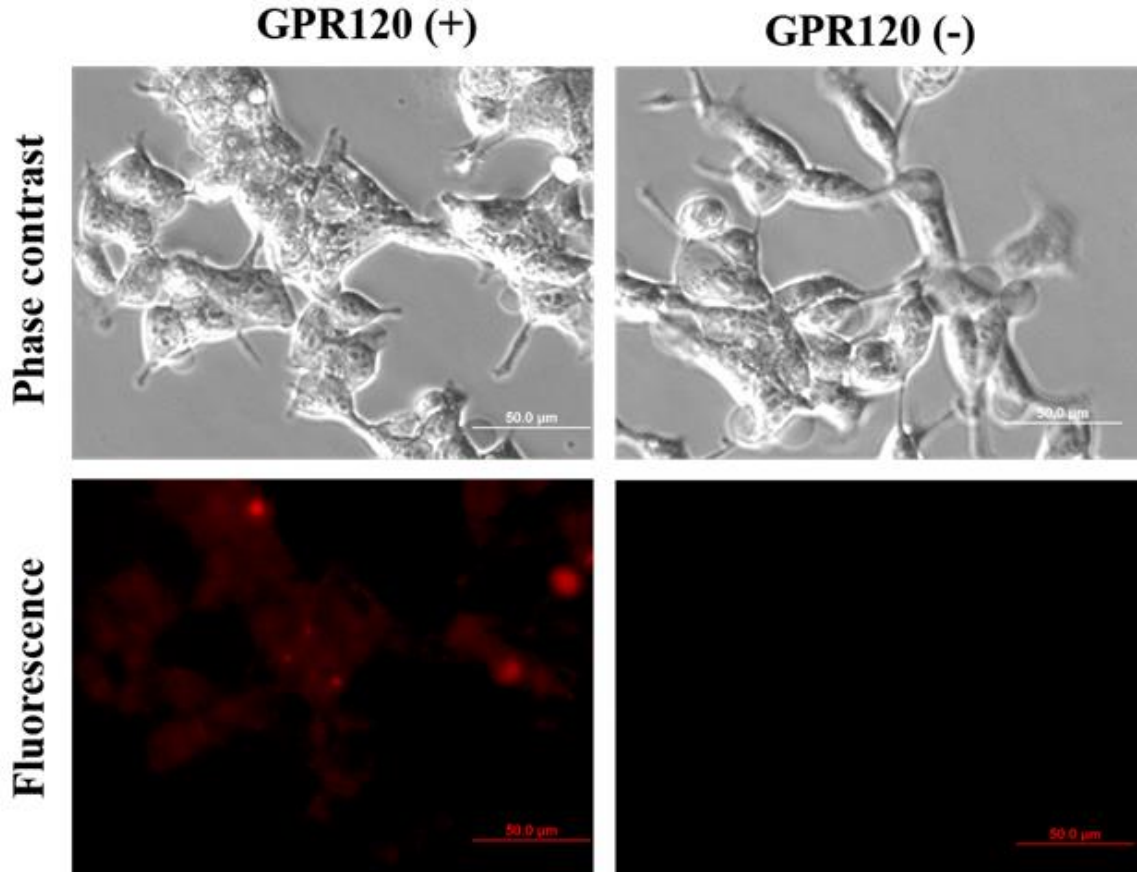


Figure 6.5 Fluorescence imaging of GPR120 (+) and GPR120 (-) cells incubated with $CaMoO_4:Eu^{3+}$@AuNR-MBA-Ab nanoprobe for 24 hr.

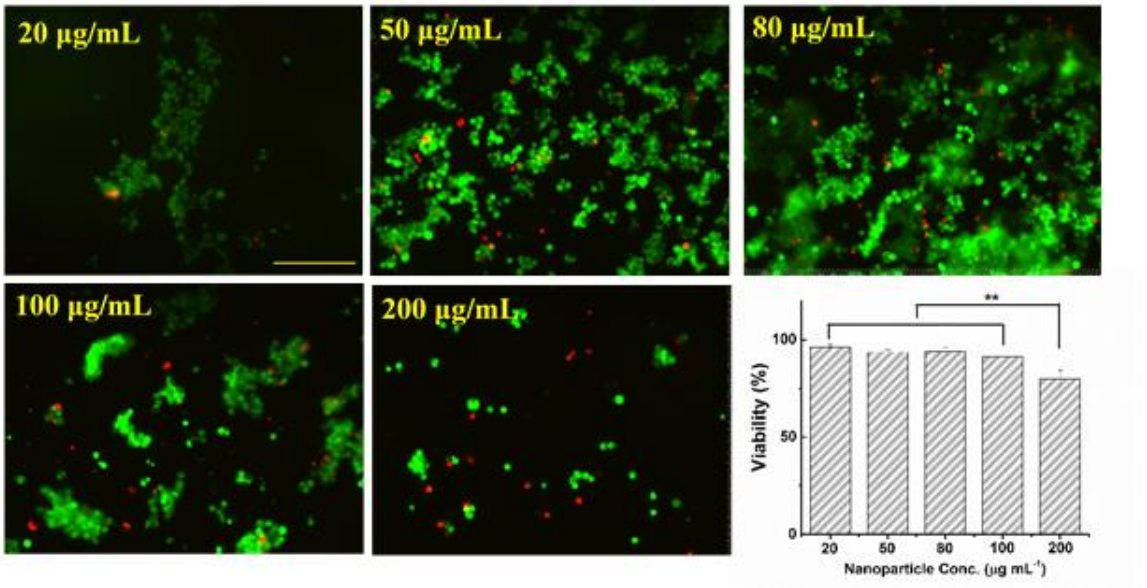


Figure 6.6 Viability of GPR120 (+) cells with 24-hr incubation of $CaMoO_4:Eu^{3+}$@AuNR-MBA-Ab nanoprobe at concentrations of 20, 50, 80, 100, and 200 µg/mL. Green fluorescence presented live cells, whereas red fluorescence showed dead or membrane-damaged cells. Over 300 cells were counted for each treatment condition. Scale bar: 200 µm. **P<0.001.

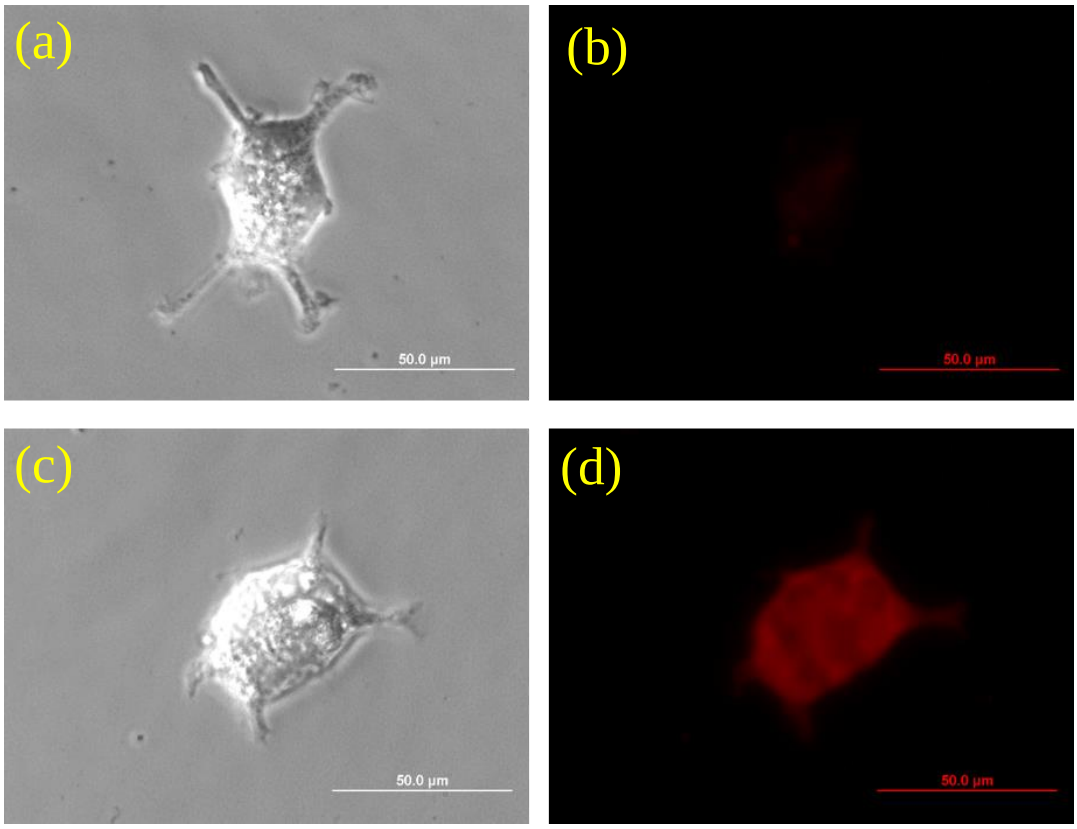


Figure 6.7 Phase contrast (a, c) and Fluorescence (b, d) images of single CD36 (a, b) and GPR120 (+) (c, d) cells incubated with $CaMoO_4:Eu^{3+}$@AuNR-MBA-Ab nanoprobes for 24 hr.

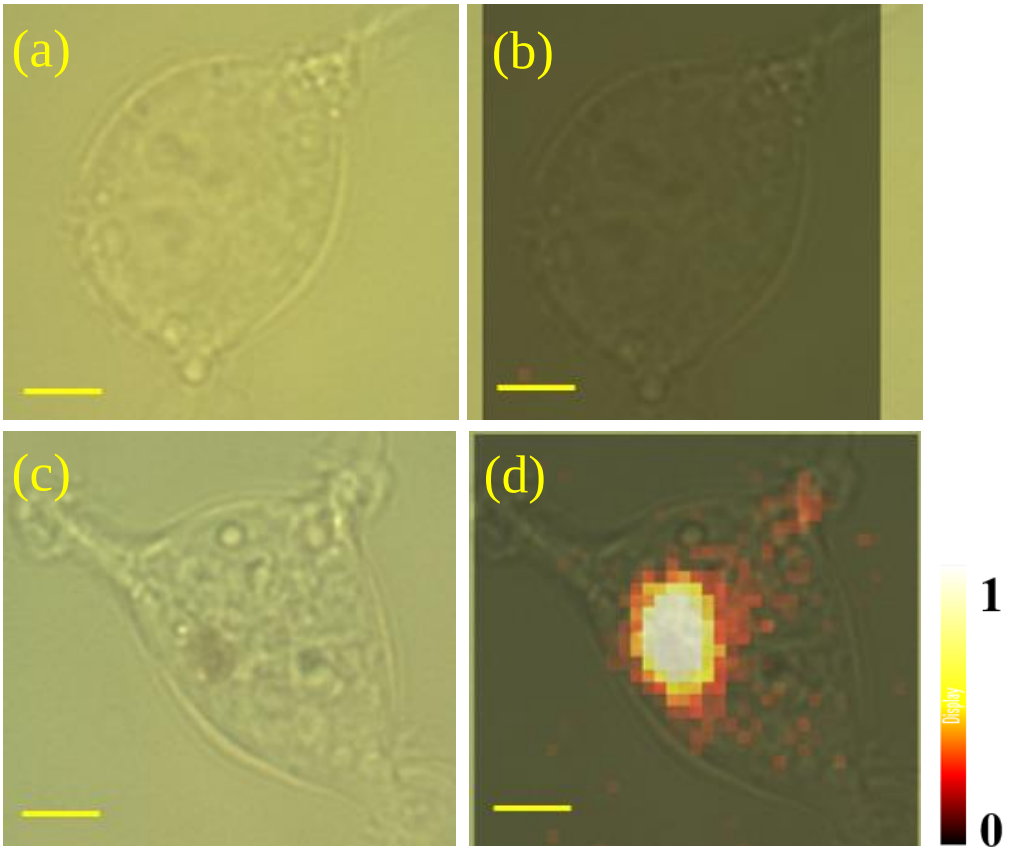


Figure 6.8 Bright field images (a, c) and Raman mappings (b, d) of single CD36 (a, b) and GPR120 (+) (c, d) cells incubated with $CaMoO_4:Eu^{3+}$@AuNR-MBA-Ab nanoprobes for 24 hr. Raman mappings were generated by the selection of peak 1078 cm^{-1}. The intensities were normalized between the lowest (0) and highest (1) color values. Scale bar: 5 μm.

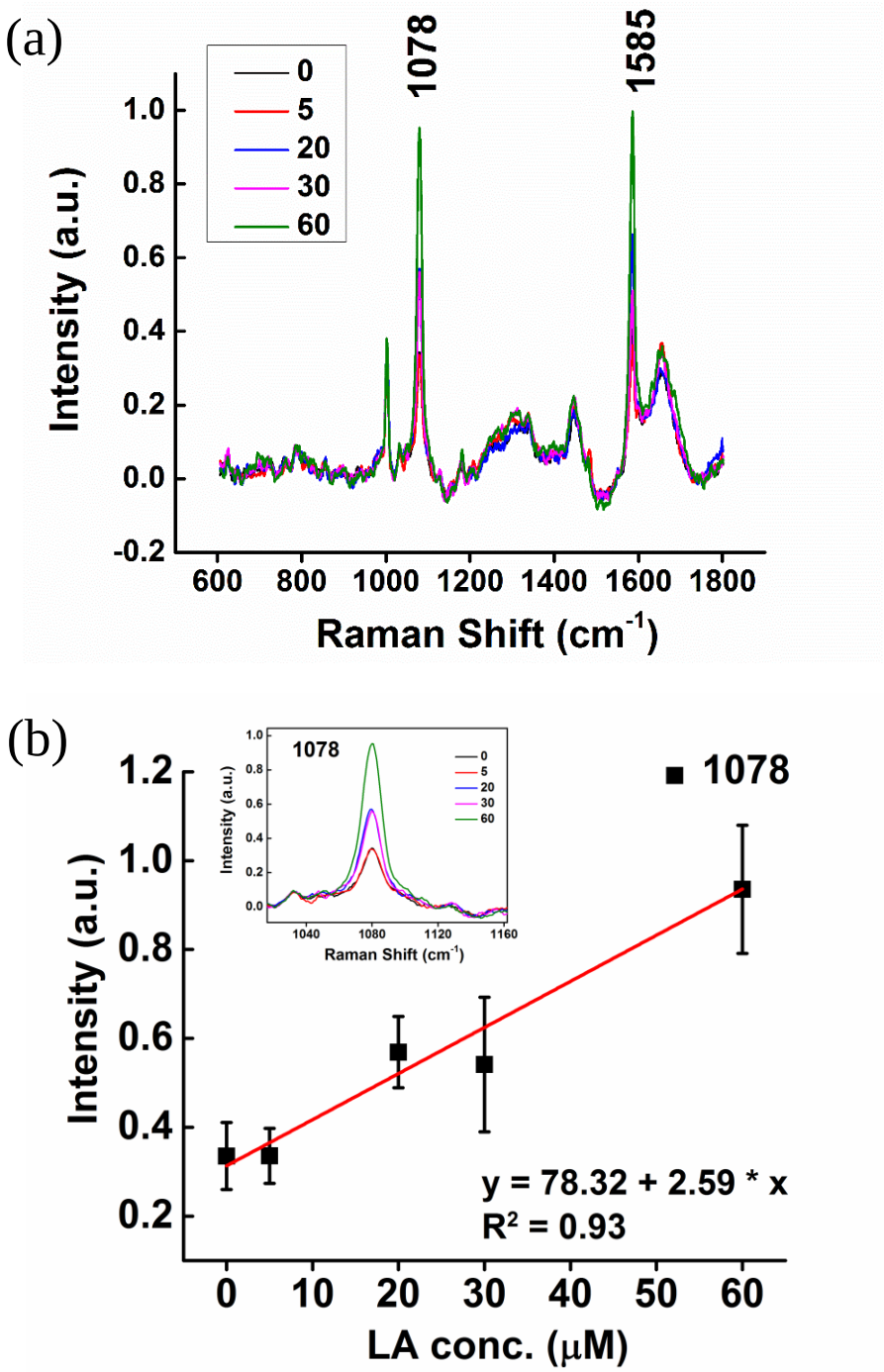


Figure 6.9 GPR120-LA dependence measured by SERS. (a) Average Raman spectra of $CaMoO_4:Eu^{3+}$@AuNR-MBA-Ab nanoprobe-incubated cells under 5 min LA treatment at concentrations 0, 5, 20, 30, and 60 μg/mL. (b) Linear relationship (R^2=0.93) between SERS intensity (1078 cm^{-1}) and LA concentration. Inset: expanded Raman spectra around 1078 cm^{-1}.

CHAPTER 7

SUMMARY AND FUTURE DIRECTION

7.1 SUMMARY

The overall objective of this dissertation is to study human disease at single cell level using advanced instrumentation including atomic force microscopy (AFM), Raman spectroscopy and fluorescence microscopy. Research presented in five technical chapters (chapter 2-6) can be summarized as following:

- Apply atomic force microscopy (AFM) and Raman spectroscopy to measure cellular biomechanical and biochemical properties for classification of cells in different conditions.
- Design and synthesize nanoparticle-based probes for highly sensitive and specific imaging and detection of cell surface receptors using surface-enhanced Raman scattering (SERS), AFM-based nanoscale recognition and fluorescence microscopy.

In chapter 2, we measured the biomechanical and biochemical properties of healthy and cancerous (SAEC & A549) human lung epithelial cells, and compared their responses to short-term (4 hr) anticancer drug doxorubicin (DOX) treatments, using AFM and Raman spectroscopy. Some key research findings are: (1) cancerous A549 cell is less stiff and less adhesive than healthy SAEC cell. (2) After DOX treatment, A549 gets stiffer and more adhesive while SAEC respond oppositely, resulting a reduced difference in biomechanics between two cell lines. (3) DOX treatment causes decrease in DNA but increase in protein and lipid contents in both cell lines. We also discussed the potential correlation between the biomechanics measured by AFM and the biochemical composition measured by Raman spectroscopy, and suggested a series of experiments to study the correlation.

In chapter 3, a gold nanorod (AuNR)-based SERS nanoprobe was developed for single-cell analysis of epidermal growth factor receptor (EGFR). The SERS probe was able to specifically target EGFR in single breast cancer cell and generate characteristic Raman peak that can be used determine the localization of EGFR on cell membrane surface. Quantification of EGFR expression level was performed using SERS and confirmed by immunoblotting. In addition, cellular distribution of EGFR was visualized by single-cell SERS mapping, which provides more detailed spatial resolution at single cell level comparing with traditional immunofluorescence imaging. EGFR-mediated nanoparticle endocytosis was also investigated by depth SERS mapping, demonstrating the potential of SERS, as a noninvasive technique, to study dynamic cellular process.

Chapter 4 described an AFM-based recognition imaging technique—simultaneous Topography and RECognition (TREC) imaging—for nanoscale imaging of EGFR. Experiments on mica demonstrated high specificity, reproducibility and efficiency of TREC imaging technique for EGFR recognition. Single molecule recognition of EGFR was achieved in fixed and living breast cancer cells. TREC imaging exhibited potential to monitor cellular activities like receptor-ligand binding at single molecule level.

Chapter 5 introduced a previously reported MRI contrast agent Gd-Au nanocomposite. We further functionalized the composite Gd-Au nanoprobe to integrate SERS function and tested its SERS performance. Our results showed that composite Gd-Au nanoprobe successfully served as a SERS probe for single-cell mapping of EGFR as well as quantification of EGFR levels in different cancer cells, showing the potential of this nanoprobe for MRI-SERS multifunctional detection and bioimaging.

In chapter 6, we developed a SERS-fluorescence dual functional nanoprobe for *in vitro* imaging of fat-responsive GPR120 receptor. We tested the performance of this nanoprobe for specific imaging of GPR120 using SERS and fluorescence imaging. Furthermore, by using SERS, we observed a dose-dependent GPR120 response to linoleic acid treatment. Our results showed a bright perspective to study fat receptors and their interaction with fatty acids using SERS.

7.2 FUTURE DIRECTION

7.2.1 Cellular analysis of human diseases by AFM and Raman spectroscopy

In this dissertation, I included a study that uses our tandem AFM/Raman system to measure the biomechanical properties and biochemical composition of human lung cancer cells (chapter 2), demonstrating the strength of our combined AFM/Raman system as an noninvasive tool for cellular diagnosis of human diseases like cancer. In fact, due to the noninvasive nature of this technique, and its ability to provide quantitative information for cells, our AFM/Raman system can be applied for a range of different cell analysis. For example, we have measured the changes in biomechanics and biochemical composition during differentiation process of stem-like cells [1]. We also have investigated the toxicity effects of diesel exhaust particles (DEPs) to human lung cells by measuring their biomechanical and biochemical responses [2]. Another ongoing project is that we are trying to use our AFM/Raman instrumentation to study human lung cells in response to inflammatory stimuli. We would also investigate human cellular response to air pollutant like PM2.5.

Although AFM and Raman spectroscopy are techniques with great potential in cell analysis, they only physical and basic chemical properties, and need to combine with other

techniques for comprehensive analysis. In other words, since AFM and Raman spectroscopy are not standard approaches for many biological assays, they need to be validated by other tested methods. For example, in addition to the biomechanical and biochemical properties measured by AFM and Raman spectroscopy, we could use multiplex ELISA to measure cytokine and chemokine production to verify the inflammatory responses of cells induced by DEP treatments. We could use quantitative PCR to measure gene expression long with the biophysical and biochemical changes during cell differentiation.

In summary, our AFM/Raman system has great potential in mammalian cell analysis. It could provide supplementary information to conventional biological techniques for better investigation of complicated biological problems. Thus using AFM and Raman spectroscopy for studies human diseases at cellular level is still an important future direction in our lab.

7.2.2 nanoparticle-based imaging probes for noninvasive bioimaging

Molecular imaging of human disease cells by nanoparticle-based imaging probes is the major focus of this dissertation. Metallic nanoparticles (e.g. Au or Ag) showed remarkable light scattering efficiency due to their strong surface plasmon resonance. Especially for Au nanoparticles, the high photostability, water solubility and low cytotoxicity make them favorable for biological imaging. In this dissertation, several studies have been done using Au nanoparticle-based contrast agent for *in vitro* bioimaging. A lot more experiments could be performed in this direction in the future.

One project ongoing is to use Au nanoparticle-base imaging probe for multiplex SERS detection of fat receptors GPR120 and CD36 at single cell level, because their roles

in the chemoreception of fatty acids are thought to be critical for people to understand fat preference and develop obesity treatments. In chapter 6 of this dissertation, we have presented a study using SERS-fluorescence bimodal imaging technique to study GPR120 in single cells. However, we are more interested in the interactions between the two receptors GP120 and CD36, even their interactions with fatty acids. From this perspective, one experiment we can do is to build multiplex SERS probes, and use them to mapping cellular distribution of both GPR120 and CD36 in same single cell. Moreover, we can monitor their distribution change when fatty acid is introduced using single cell SERS mapping. Even though SERS technique shows great promise for multiplex detection and imaging, it still suffers the diffraction limit of optical imaging techniques. In order to achieve nanoscale imaging resolution, we could apply tip-enhanced Raman scattering (TERS), which uses an AFM probe instead of a laser to map the cell surface. Due to the nanoscale imaging capability of AFM, TERS is promising to provide us the detailed spatial information of GPR120 and CD36 distribution at subcellular level or even single molecule level.

Another direction is multimodal *in vivo* boimaging. As discussed in previous chapters, multimodal imaging can integrate advantages of different imaging modalities, improving imaging performance in resolution and sensitivity. In this dissertation, I have included two studies describing bimodal imaging probes for *in vitro* bioimaging (chapters 5 and 6). The sensitivity, specificity and biocompatibility of these probes have been tested by *in vitro* experiments. It is very promising to apply these probes for more clinically important *in vivo* imaging. One potential challenge is the long-term stability of these probes. Will these probes maintain their stable structure in complex biological environments like

animal organs? What iss the retention time of these nanoprobes in animal body? There questions need to be further investigated in future studies.

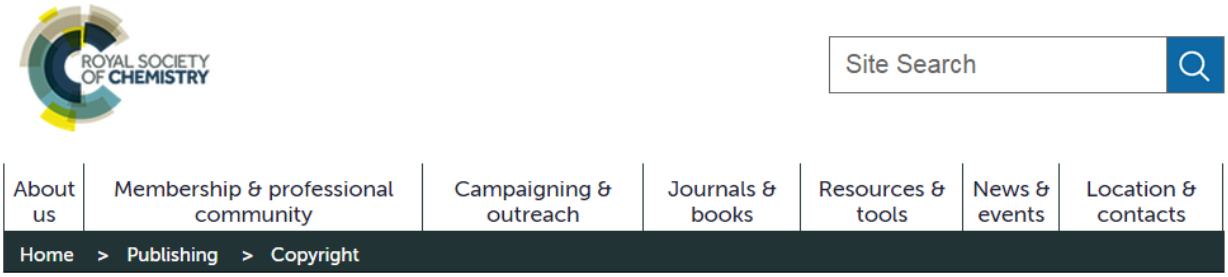
Besides the imaging application, there are many other biological application of metallic nanoparticles that worth investigation in the future. For example, we could apply Au nanoparticles for photothermal therapy (PTT) or photodynamic therapy (PDT) of human cancers. My colleague Qifei Li from Dr. Anhong Zhou's lab has done some initial work on PTT and PDT of human cancer cells using Au nanoparticle-based nanoprobes. In addition, we could also develop porous nanostructures as carriers for drug delivery and controlled drug release. In a word, our future direction is to use advanced instrumentation and nanotechnologies to help biologists solve more sophisticated biology problems.

7.3 References

[1] Q. Li, E. Suasnavas, L. Xiao, S. Heywood, X. Qi, A. Zhou, S.C. Isom, Label-free and non-invasive monitoring of porcine trophoblast derived cells: differentiation in serum and serum-free media, J. Biophotonics, (2014) doi: 10.1002/jbio.201400062.

[2] M.J. Tang, Q.F. Li, L.F. Xiao, Y.P. Li, J.L. Jensen, T.G. Liou, A.H. Zhou, Toxicity effects of short term diesel exhaust particles exposure to human small airway epithelial cells (SAECs) and human lung carcinoma epithelial cells (A549), Toxicol. Lett. 215 (2012) 181-192.

APPENDIX



Author use of own material in theses and dissertations

Authors of articles in our journals or chapters in our books do not need to formally request permission to reproduce their article or book chapter in their thesis or dissertation. For all cases of reproduction the correct acknowledgement should be given in the caption of the reproduced material. The acknowledgement depends on the publication in which the material was published. The form of the acknowledgement to be included in the caption can be found on the page entitled *Acknowledgements to be used by RSC authors*.

Please ensure that your co-authors are aware that you are including the paper in your thesis.

http://www.rsc.org/Publishing/copyright/permission-requests.asp

Permission Letter

Mingjie Tang
Chongqing Institute of Green and Intelligent Technology, Chinese Academy of Sciences
No.266 Fangzheng Avenue, Shuitu Hi-tech Industrial Park, Shuitu Town,
Beibei District, Chongqing, China 400714

March 31, 2015

Lifu Xiao
Department of Biological Engineering
Utah State University
Logan, UT 84322-4105

This letter grants my permission to Lifu Xiao to use the following publication in part or in full for inclusion in his Ph.D. dissertation.

Xiao, L., Tang, M., Li, Q., and Zhou, A. (2013). Non-invasive detection of biomechanical and biochemical responses of human lung cells to short time chemotherapy exposure using AFM and confocal Raman spectroscopy. Analytical Methods, 5(4), 874-879.

Sincerely,



Mingjie Tang

Permission Letter

Qifei Li
Department of Biological Engineering
Utah State University
Logan, UT 84322-4105

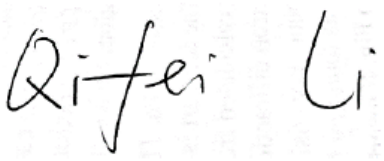
March 31, 2015

Lifu Xiao
Department of Biological Engineering
Utah State University
Logan, UT 84322-4105

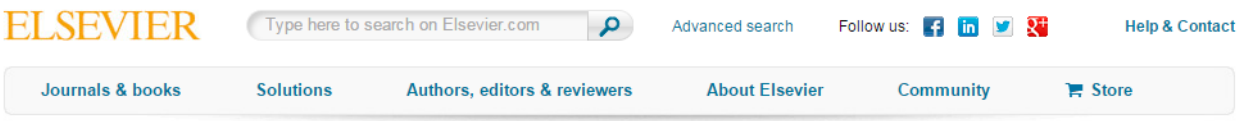
This letter grants my permission to Lifu Xiao to use the following publication in part or in full for inclusion in his Ph.D. dissertation.

Xiao, L., Tang, M., Li, Q., and Zhou, A. (2013). Non-invasive detection of biomechanical and biochemical responses of human lung cells to short time chemotherapy exposure using AFM and confocal Raman spectroscopy. Analytical Methods, 5(4), 874-879.

Sincerely,



Qifei Li



Lightbox_Scholarly purposes

Personal (scholarly) purposes

Authors can use their articles, in full or in part, for a wide range of scholarly, non-commercial purposes as outlined below:

- Share copies of the article and distribute them via email to colleagues for their research use (also known as 'scholarly sharing').
- Share the article for personal use or for the author's own classroom teaching.
- Use the article at a conference, meeting or for teaching purposes.
- Allow the author's employers to use the article for other internal purposes (such as training).
- Include the article in a printed compilation of the author's works, such as collected writings and lecture notes.
- Inclusion the article in a thesis or dissertation
- Use the article in full or in part to prepare other derivative works, including expanding the article to book-length form, with each work to include full acknowledgement of the article' original publication.

These rights apply for all Elsevier authors who publish their article as either a subscription article or an open access article. In all cases we require that all Elsevier authors always include a full acknowledgement and, if appropriate, a link to the final published version hosted on Science Direct.

http://www.elsevier.com/about/policies/author-agreement/lightbox_scholarly-purposes



Department of Cancer Biology

Danny R. Welch, Ph.D.
Professor & Chair, Department of Cancer Biology
Associate Director - Basic Sciences, KU Cancer Center
Kansas Bioscience Authority Eminent Scholar
Director, Graduate Program in Cancer Biology
Director, NFCR Center for Metastasis Research
Deputy Editor, *Cancer Research*

Lifu Xiao
Department of Biological Engineering
Utah State University
Logan, UT 84322-4105

April 14, 2015

This letter grants my permission to Lifu Xiao to use the following publication in part or in full for inclusion in his Ph.D. dissertation.

Xiao, L., Harihar, S., Welch, D. R., and Zhou, A. (2014). Imaging of epidermal growth factor receptor on single breast cancer cells using surface-enhanced Raman spectroscopy. Analytica chimica acta, 843, 73-82.

Sincerely,

Danny R Welch

Permission Letter

Sitaram Harihar
Institute of Molecular and Cell Biology (IMCB)
61 Biopolis Drive, Proteos
Singapore 138673

March 31, 2015

Lifu Xiao
Department of Biological Engineering
Utah State University
Logan, UT 84322-4105

This letter grants my permission to Lifu Xiao to use the following publication in part or in full for inclusion in his Ph.D. dissertation.

Xiao, L., Harihar, S., Welch, D. R., and Zhou, A. (2014). Imaging of epidermal growth factor receptor on single breast cancer cells using surface-enhanced Raman spectroscopy. Analytica chimica acta, 843, 73-82.

Sincerely,

H. Sitaram

Sitaram Harihar

CURRICULUM VITAE

Lifu Xiao

1693 N 400 W

APT N203

Logan, UT 84341

E-mail: lifu.xiao@aggiemail.usu.edu or lfxiao0517@gmail.com

Work Phone: (435)213-8716 Cell Phone: (435)757-1349

Education

09/2011-05/2015 (expected)	Ph.D. in Biological Engineering, Utah State University, Logan UT. Advisor: Anhong, Zhou, Ph.D.
09/2007-07/2011	B.Sc. in Chemistry, Fudan University, Shanhai, China.

Experimental Skills

Mammalian Cell Culture, Bench Chemistry, Nanomaterial Preparation

Raman spectroscopy, Atomic Force Microscopy, Fluorescence Microscopy

Awards and Recognitions

- Keysight Technologies AFM image competition "2015 Calendar Image" (2015)
- Robins Award, finalist, Utah State University (2015)
- Graduate Researcher of the Year, College of Engineering (2015)
- Outstanding Graduate Researcher, Department of Biological Engineering (2015)
- USU Graduate Students Travel Awards (2014)
- Top 10 most accessed articles, Analytical Methods (Feb 2013)
- 2nd place Poster competition, Annual Institute of Biological Engineering Western Regional Conference (2011)

Research Experience

Graduate Research Assistant (2011-present)

- A combined TERS and functional cellular imaging approach to explore receptor function. (NSF grant) (2013-present)
    - Design and synthesize composite nanoparticle for multimodal bioimaging.
    - Conjugate the nanoparticle-based imaging probe with antibodies to specifically target fatty acid-responsive cell-surface receptors.

  - In vitro imaging of receptors and monitor how receptors rearrange and co-localize on surfaces of cells.
  - Real-time imaging of receptors in response to presence of fatty acids.

- Localization and Quantification of Single EGF Receptor on Single Breast Cancer Cell Surface. (DoD CDMRP grant) (2011-2013)
  - Design a gold nanorod (GNR)-based nanoprobe for surface-enhanced Raman scattering (SERS) detection of EGFR in single breast cancer cells.
  - Develop an AFM-based simultaneous topography and recognition (TREC) imaging technique for EGFR detection at single molecule level.
  - Design a MRI-SERS bimodal nanoprobe for EGFR detection

- Detection and identification of mammalian cells by biomechanical and biochemical properties using atomic force microscopy and Raman spectroscopy (2011-2012)
  - Cell morphology was imaged by combined AFM-Fluorescence microscopic system
  - Biomechanics were measured by AFM force measurements
  - Biochemical composition was measured by Raman spectroscopy

Undergraduate Research Assistant (2009-2011)

- Fudan's Undergraduate Research Opportunities Program ("Xiyuan" Program)
  - Iron-catalyzed alkyne cyclotrimerization reaction to form benzene derivatives

- Senior Design Project
  - Nucleotide-mediated dispersion of magnetic nanoparticles for MRI-based quantification of enzyme

Journal Publications

1. M. Tang, Q. Li, **L. Xiao**, Y. Li, J. L. Jensen, T. G. Liou, A. Zhou, Toxicity effects of short term diesel exhaust particles exposure to human small airway epithelial cells (SAECs) and human lung carcinoma epithelial cells (A549), **Toxicology letters** 215.3 (2012): 181-192.
2. **L. Xiao**, M. Tang, Q. Li, A. Zhou, Non-invasive detection of biomechanical and biochemical responses of human lung cells to short time chemotherapy exposure using AFM and confocal Raman spectroscopy, **Analytical Methods** 5.4 (2013): 874-879 (**top ten accessed article** in Feb 2013 of the journal).
3. G. Liang, **L. Xiao**, H. Chen, Q. Liu, S. Zhang, F. Li, J. Kong, Label-free, nucleotide-mediated dispersion of magnetic nanoparticles for "non-sandwich type" MRI-based quantification of enzyme, **Biosensors and Bioelectronics** 41 (2013): 78-83.
4. **L. Xiao**, S. Harihar, D. R. Welch, A. Zhou, Imaging of epidermal growth factor receptor on single breast cancer cells using surface-enhanced Raman spectroscopy, **Analytica Chimica Acta** 843 (2014): 73-82.

5. Q. Li, E. Suasnavas, **L. Xiao**, S. Heywood, X. Qi, A. Zhou, S. C. Isom, Label-free and non-invasive monitoring of porcine trophoblast derived cells: differentiation in serum and serum-free media, **Journal of Biophotonics** (2014).
6. **L. Xiao**, X. Tian, S. Harihar, Q. Li, L. Li, D. R. Welch, A. Zhou, Gd_2O_3-doped silica @ Au Nanoparticles as Probes for *In Vitro* Cancer Cell Imaging Biomarkers Using Surface-Enhanced Raman Spectroscopy (**Submitted**).
7. **L. Xiao**, Q. Chen, Y. Wu, X. Qi, A. Zhou, Simultaneous topographic and single molecule recognition imaging of epidermal growth factor receptor (EGFR) on single human breast cancer cells (**Submitted**).
8. Q. Li, E. Suasnavas, S. Heywood, **L. Xiao**, A. Zhou, S. Isom, Biochemical, biophysical and genetic changes of porcine trophoblast derived cells during differentiation as evaluated using Raman microspectroscopy, Atomic force microscopy and quantitative polymerase chain reaction (**Submitted**).
9. **L. Xiao**, A. K. Parchur, H. Xu, T. A. Gilbertson, A. Zhou, SERS-fluorescence bimodal imaging of fatty acid responsive receptor GPR120 (**To be submitted**).

Conference Presentations

1. **L. Xiao**, Y. Wu, Q. Chen, Q. Li, M. Tang, A. Zhou, Simultaneous acquisition of topography and recognition (TREC) images using anti-EGFR antibody modified atomic force microscopy probe, Annual Institute of Biological Engineering Western Regional Conference, Logan, Utah, Oct 28, 2011 (**2nd place award** in poster competition).
2. **L. Xiao**, A. Zhou, Probe biomechanical response and cellular biochemical composition changes of human lung epithelial cells to short time chemotherapy drug exposure using AFM and Raman Micro-Spectroscopy, Intermountain Graduate Research Symposium, Apr 5, 2012.
3. R. Li, Q. Li, **L. Xiao**, S. Williams, E. Suasnavas, C. Isom, D. Larson, L. Rickords, A. Zhou, Assessment of Cell Behaviors on TiO2 Nanotube Arrays by Using Atomic Force Microscopy, Raman Spectroscopy, Fluorescence Microscopy. In Meeting Abstracts (No. 18, pp. 2060-2060). The Electrochemical Society, June 2012.
4. **L. Xiao**, A. Zhou, Surface enhanced Raman spectroscopy detection of epidermal growth factor receptor regulated by BReast Cancer Metastasis Suppressor 1 on single breast cancer cells, Annual Institute of Biological Engineering Western Regional Conference, Logan, Utah, Oct 26, 2012.
5. **L. Xiao**, S. Harihar, Y. Wu, D. R. Welch, A. Zhou, Highly sensitive detection of cancer biomarker EGFR by PicoTREC-SERS, NanoTech Conference & Expo 2013, Washington, D.C., May 12-16, 2013.
6. **L. Xiao**, Q. Li, A. Zhou, Multimodal nano-bioprobes for imaging EGFR on single human cancer cells, SPIE Photonics West BiOS 2014, San Francisco, California, Feb 1-6, 2014 (**Podium Presentation**).
7. Q. Li, **L. Xiao**, A. Zhou, Assessment of the anti-cancer drug chemoresistance by Raman microspectroscopy and atomic force microscopy (AFM), SPIE Photonics West BiOS 2014, San Francisco, California, Feb 1-6, 2014.
8. **L. Xiao**, H. Xu, A. K. Parchur, Q. Li, T. A. Gilbertson, A. Zhou, SERS-fluorescence bimodal nanoprobes for imaging of HEK293 cells expressing

GPR120, The 69th Northwest Regional Meeting of the American Chemical Society, Missoula, Montana, Jun 22-25, 2014.

9. Q. Li, S. Heywood, **L. Xiao**, M. Tang, A. Zhou, S. C. Isom, Atomic force microscopy (AFM), Raman microspectroscopy (RM) and gene chip monitoring of porcine trophoblast derived cells differentiation, SPIE Photonics West BIOS 2015, San Francisco, California, Feb 7-12, 2015.
10. **L. Xiao**, A. K. Parchur, H. Xu, Q. Li, T. A. Gilbertson, A. Zhou, Lanthanide (Ln^{3+})-doped calcium molybdate nanoparticle ($CaMoO_4:Ln^{3+}$, Ln=Eu, Tb) based SERS-fluorescence bimodal imaging probes for detection and imaging of fatty acid responsive GPR120 and CD36 receptors, SPIE Photonics West BIOS 2015, San Francisco, California, Feb 7-12, 2015 (**Podium Presentation**).
11. **L. Xiao**, H. Xu, D. R. Hansen, T. A. Gilbertson, A. Zhou, In vitro SERS-fluorescence bimodal imaging of fatty acid responsive GPR120 receptor using a Gadolinium-Gold composite nanoprobe, 2015 Institute of Biological Engineering Annual Meeting, St. Louis, MO, March 5-7, 2015.

List of References

Anhong Zhou, Ph.D.
Associate Professor
Department of Biological Engineering
Utah State University
4105 Old Main Hill
Logan, UT 84322-4105
Anhong.zhou@usu.edu
Phone: 435-797-1248

Tim Gilbertson, Ph.D.
Professor
Department of Biology
Utah State University
UMC 5305
Logan, UT 84322-5305
Tim.gilbertson@usu.edu
Phone: 435 797-7314

Ronald C. Sims, Ph.D.
Professor
Department of Biological Engineering
Utah State University
4105 Old Main Hill
Logan, UT 84322-4105
Ron.sims@usu.edu
Phone: 435-770-4922